Università degli Studi di Salerno

Dipartimento di Ingegneria Elettronica ed Ingegneria Informatica

Dottorato di Ricerca in Ingegneria dell'Informazione
XI Ciclo – Nuova Serie

TESI DI DOTTORATO

Sliding Mode control of DC/DC switching converters for photovoltaic applications

CANDIDATO: **EMILIO MAMARELIS**

TUTOR: **PROF. GIOVANNI SPAGNUOLO**
CO-TUTOR: **ING. GIOVANNI PETRONE**

COORDINATORE: **PROF. ANGELO MARCELLI**

Anno Accademico 2011 – 2012

A Jaja, Natan e Nicole

Contents

This work has been supported by Bitron S.p.A. - Grugliasco (TO), both in terms of scholarship for the PhD candidate and with a number of circuit prototypes for validating the theoretical and simulation results. The PhD candidate especially wishes to acknowledge Dr. Martin Williams and Eng. Enrico Bianconi for their precious support.

Introduction

The maximum power point tracking (MPPT) is one of the most important features of a system that process the energy produced by a photovoltaic generator must hold. It is necessary, in fact, to design a controller that is able to set the value of voltage or current of the generator and always ensure the working within its maximum power point. This point can considerably change its position during the day, essentially due to exogenous variations, then sunshine and temperature. The MPPT techniques presented in literature and adopted in commercially devices operate a voltage control of the photovoltaic generator and require careful design of the control parameters. It is in fact complex obtain high performance both in stationary that strongly variable conditions of sunshine without a careful choice of some parameters that affect in both conditions the performance of the algorithm for the MPPT.

In this thesis has been addressed the analysis of an innovative current-based MPPT technique: the sensing of the current in the capacitor placed in parallel with the photovoltaic source is one of the innovative aspects of the proposal. The controller is based on a nonlinear control technique called "sliding mode" of which has been developed an innovative model that allow to obtain a set of conditions and enable the designing of the controller with extreme simplicity. The model also allow to demonstrate how the performance of this MPPT control tecnique are independent not only from the characteristics and operating conditions of the photovoltaic generator, but also by the parameters of the switching converter that implements the control. This property allows a significantly simplification in the designing of the controller and

improve the performance in presence of rapid changes of the irradiance.

An approach to the dynamic analysis of a class of DC/DC converters controlled by a sliding mode based maximum power point tracking for photovoltaic applications has been also presented. By referring to the boost and SEPIC topologies, which are among the most interesting ones in photovoltaic applications, a simple analytical model is obtained. It accounts for the sliding mode technique that allows to perform the maximum power point tracking of the photovoltaic generator connected at the converters input terminals. Referring to the previous approach, a correction term allowing to have an increased accuracy of the model at high frequencies has been also derived.

The control technique proposed has been implemented by means of low cost digital controller in order to exploit the potential offered by the hardware device and optimize the performance of the controller. An extensive experimental analysis has allowed to validate the results of the research.

The laboratory measurements were conducted on prototypes of DC/DC converters, boost and SEPIC, carried out by Bitron SpA. There are a considerable experimental tests both in the time and in the frequency domain , both using source generator in laboratory than photovoltaic panels. The results and theoretical simulations have found a large validation through laboratory measurements.

The dissertation is organized as follows. In Chapter 1 an introduction to photovoltaic systems is presented. In Chapter 2, a new current-based P&O MPPT with sliding mode control strategy is proposed and applied to the boost converter. The small signal model and the experimental validation for a high order converter are derived in Chapter 3. In Chapter 4 an accurate SM linear model is derived and validated by means of experimental results. Chapter 5 is devoted to the implementation of the sliding mode controller, a novel hybrid analog-digital configuration is explained. Conclusions and final considerations end this work.

Chapter 1

Maximum power point tracking in photovoltaic applications

In recent years PhotoVoltaic (PV) systems have assumed an increasing role in modern electric power production technologies, providing secure and pollution free energy. A PV string is a dependent power source that shows a non linear voltage vs. current (v-i) characteristic, depending on some external parameters, such as irradiance and temperature (Fig.1.1).

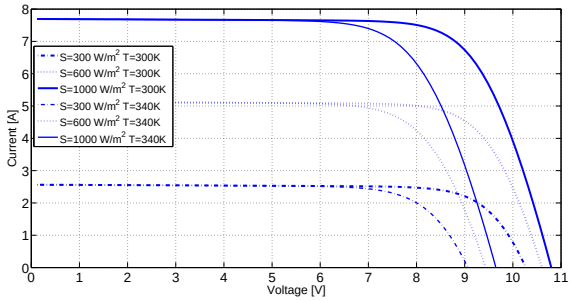

Figure 1.1: Non linear photovoltaic I-V characteristics

The curves clearly exhibit a Maximum Power Point (MPP)

whose location depends on the values assumed by the exogenous parameters mentioned before as well as on manufacturing tolerances and aging. In order to reduce the effects of the relatively high fabrication costs and the low energy conversion efficiency, the employment of control systems that help in using PV arrays more efficiently and in extracting the maximum available power from them under different environmental conditions are mandatory. Specific solutions for the power conversion are available, but they also require ad hoc control techniques for the Maximum Power Point Tracking (MPPT).

1.1 Main MPPT techniques

The MPPT algorithms that are most widely discussed in literature and used in commercial products are the Perturb and Observe (P&O) and the Incremental Conductance (INC) [HMHO95] techniques. P&O is based on a perturbative approach: the PV operating point is in fact perturbed periodically based on the comparison between the PV power before and after the perturbation. If the PV power has increased, this means that the operating point has been moved towards the MPP and the subsequent perturbation will have the same sign of the previous one. If the PV power decreases, this means that the operating point has been moved away from the MPP, thus the sign of the subsequent voltage perturbation is reversed. An evident drawback of this approach is that also in sunny days or with slowly variation of the irradiance the operating point oscillates around the MPP, thus wasting some amount of available energy. Anyway, as discussed in [HR00], because of noise, measurement and quantization errors, also the INC algorithm lets the operating voltage oscillate around the MPP. In [HR00] it is shown that the P&O method ensures an MPPT efficiency which is close to that one given by the INC method. Other different MPPT techniques have been proposed in literature; they use different control strategies in terms of complexity, efficiency and implementation costs. For example, in [WKK+94] an MPPT

approach using fuzzy logic control algorithm is introduced. Although this approach is capable of improving the tracking performance compared with conventional methods, unfortunately several parameters are selected on a trial and error basis, essentially depending on the designer experience and intuition. A real time MPPT controller for PV grid connected systems based on neural networks is described in[HKIO95]. In [ISTS00] an MPPT technique which uses monitoring cells to get proper starting point of the operation is shown. Unfortunately, most of these techniques have a limited field of practical applicability because they require expensive hardware resources. A full description and a comparison of a number of MPPT control approaches is given in [EC07]. For its low complexity and cost of implementation MPPT with P&O approach is very common in many PV systems [FLM08]. The P&O technique often operates the direct perturbation of the duty ratio of the power converter (Fig.1.2a). Better performances are obtained by applying perturbations to the reference voltage of an error amplifier which generates the signal controlling the duty-cycle (Fig.1.2c): an in-depth analysis of this aspect is performed in[FPSV09] and a quantification of the performances of the two solutions is given in [FPSV09].
In order to reduce the amplitude of oscillations around the MPP several improvements of the P&O algorithm have been proposed in literature. Unfortunately, no guidelines or general rules are provided to determine the optimal values of the two P&O parameters, that are the amplitude and the frequency of the perturbations. A theoretical analysis allowing the optimal design of the values of such a two parameters according to the converter's dynamics is carried out in [FPSV05]. It is applicable to any power conversion system connected to a PV source that shows only one peak in the v-i characteristic (Fig.1.4a), thus it fails in case of PV arrays subjected to mismatching phenomena.

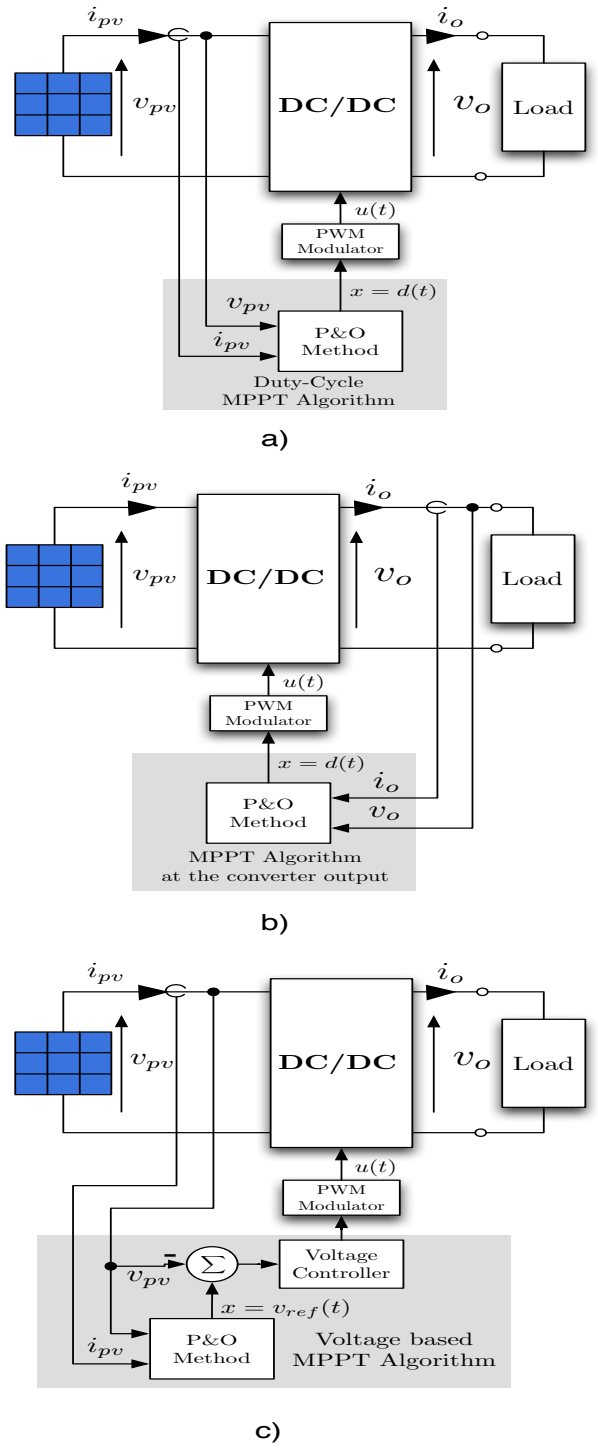

Figure 1.2: P&O converters

1.2 MPPT and Distributed-MPPT

The basic PV system structure is made of strings of PV modules which were connected in parallel and fed a central DC/AC inverter that was responsible of the Field MPPT (Fig.1.3).

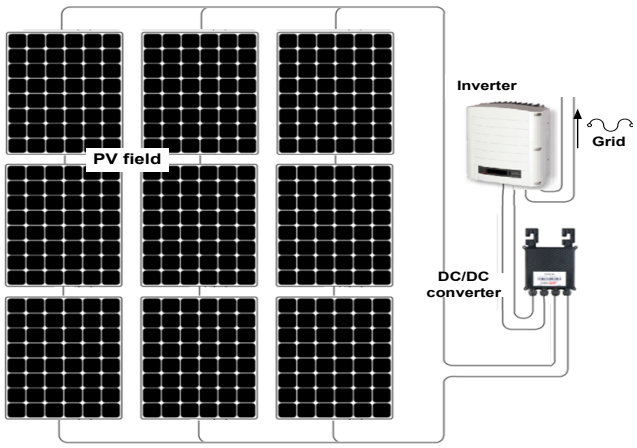

Figure 1.3: PV field inverter.

Due to mismatching effects among the cells in a PV string, e.g. due to aging, shadowing and occasional phenomena, significant power drops can occur. The same effect can be due to different orientation of the PV panels, because of ground unevenness and mistakes in the installation. In order to minimize this energy production reduction, commercial PV modules are equipped with bypass diodes. These give the advantage of removing the current bottlenecks due to mismatching, but lead to multi-modal v-i curves. Details about the possible modifications in the curve shape can be found in [G.P07]. With this kind of curves (Fig.1.4b), the probability that the classical MPPT algorithms fail is very high with obvious implications in terms of efficiency. In order to avoid the PV multimodal characteristic the so-called Distributed MPPT (DMPPT) approach has been recently proposed in literature.

Nowadays, some products implementing this idea have been put on the market by some producers [FLP+08]. It is possible in fact to overcome the drawbacks associated to mismatching phenomena by the adoption of a module dedicated DC/DC converter carrying out the MPPT for each module and eventually a central inverter for grid-connected applications or battery recharging (Power Optimizer) as in Fig.1.5. Moreover, the adoption of the so called Module Integrated Inverter is possible: this architecture makes the PV module a "plug and play" system that can directly be connected to the grid without any additional device and usable by persons without any knowledge of electrical installations (Fig.1.6). Both DC/DC and DC/AC solutions for D-MPPT must have a conversion efficiency as high as the one ensured by the centralized solutions.

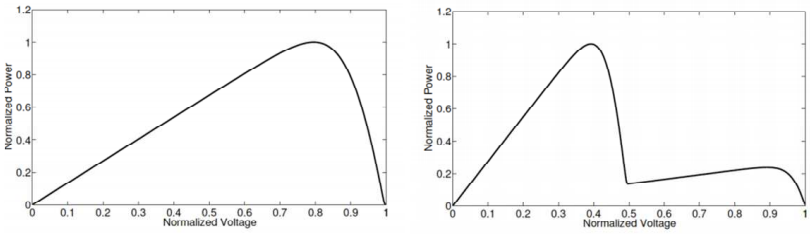

Figure 1.4: a) PV Monomodal characteristic;b) PV Multimodal characteristic;

Otherwise, the advantages obtained by a distributed control are compensated by a lower conversion efficiency, so that the D-MPPT approach becomes useless. In D-MPPT the classical MPPT techniques can be used, because the PV sections controlled by dedicated controllers are less probably affected by mismatching phenomena, so that their v-i curves exhibit a single MPP.

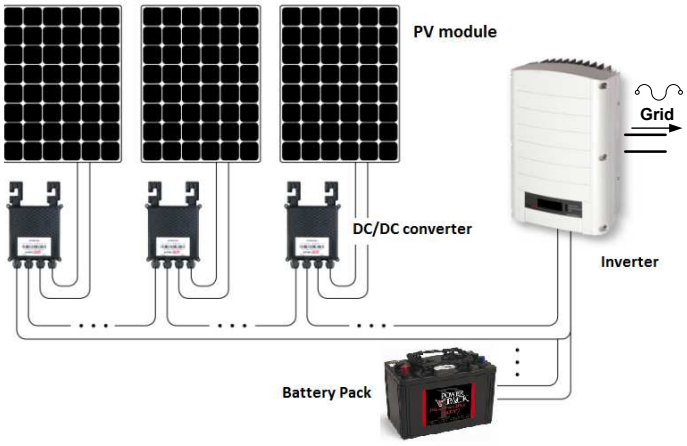

Figure 1.5: Power Optimizer.

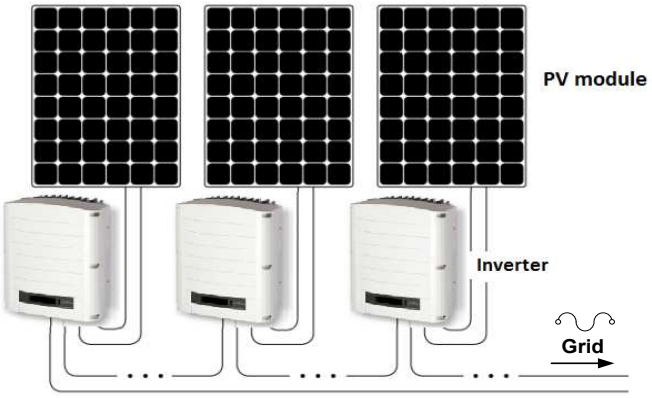

Figure 1.6: Module Inverter.

1.3 Design of the MPPT in PV systems

The maximization of the conversion efficiency is the starting point of the design process of any power stage. The peculiarity of the PV applications is in the fact that the operating point is not constant but it is continuously changing. So all the design process involves not only decisions concerning the topology of the dc/dc converter, the type of power components, the value of the output voltage, the value of the switching frequency, the efficiency of the charge/discharge processes of the batteries, their lifetime, and the shape of the profile of the power required by the load, but also the time varying characteristics of the PV sources. It is worth noting that it is not possible to identify a single reference operating condition to be taken into account in the design process. In particular the profile of the efficiency of the dc/dc converter must be optimized on the basis of the power profile of the PV source which in turn depends on the weather conditions characterizing the installation site.

Thus, a high degree of robustness must be ensured in spite of large input voltage, output current, and even parametric variations. The classical control design procedure relies on the state space averaging method, which derives an equivalent model by averaging all the system variables in a switching period. By assuming that the switching frequency is much greater than the natural frequency of system variables, low-frequency dynamics is preserved while high-frequency behavior is neglected. By means of the averaged model, a suitable small signal model is then derived by perturbing and linearizing around a precise operating point. Finally, the small-signal model is used to derive all the necessary converter transfer functions to design a linear control system by using classical control techniques. The design procedure is well known, but it is not completely correct for PV systems, because of the strong dependence of the small-signal model parameters on the system operating point. Thus, suitable procedures must be applied [AFP+10].

Although the conversion efficiency is a key point in the design of the PV processing system, the control algorithms should ensure a reliable MPPT and also the system stability in any operating condition as well as good static and dynamic performances in terms of rejection of input voltage disturbances and load changes. In the sequel, the differences in MPPT approaches based on the PV voltage and current sensing are discussed and the main mechanism that significantly affects the MPPT efficiency in both grid connected and stand alone applications is described.

1.3.1 Voltage based and current based MPPT approaches

The largest part of the MPPT algorithms presented in the literature is voltage-based, because of the logarithmic dependency of the PV voltage on the irradiation level. In fact, the linear dependency of the PV current on the irradiance level would be very useful for a fast MPPT, but the occurrence of irradiance drops might lead to the failure of the control algorithm. In Fig.1.7 are shown the waveforms obtained by adopting a direct current mode control without a voltage loop control and in presence of a negative step irradiance variation.

Two different amplitudes of the perturbation have been considered. Basically, in the first case after the perturbation the system experiences a transient from which it is able to reach new steady-state condition. In the second case instead, the system crashes since, after the irradiance perturbation, the reference current provided by the MPPT controller is higher than the short circuit current associated to the new irradiance condition . It is due to the intrinsic nature of the PV field to work like a current generator in the region at the left of the MPP. For this reason multiloop control techniques, such as current-mode control, have greatly improved power converter dynamic behavior, but the control design remains difficult especially for high-order topologies, such as those based on Cuk and SEPIC schemes. Moreover it is important for the effectiveness of this type of control techniques applied to PV

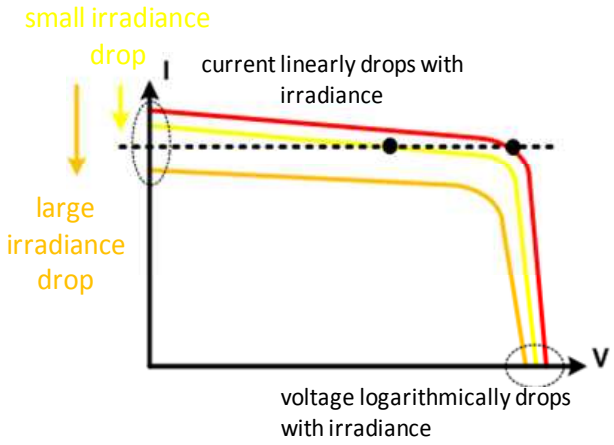

Figure 1.7: Irradiance effect on PV I-V characteristics.

context, that the current control loop is able to follow also fast irradiance variations and at the same time ensuring the rejection of the low frequency voltage oscillations affecting the PV array. In [NBGM10] the sliding mode current control is used for the MPPT of a cascade full bridge multilevel inverter grid connected PV system. In [RG11] an inner current loop together with an MPPT oriented voltage loop are used to control a grid connected inverter and to face fast irradiance variations. In [LLPG10] and [LLPG11] an hysteretic capacitor voltage control is used for the MPPT function in an energy harvesting system, so that the main aim is to reduce the power consumption of the control circuitry. Instead, few examples of current-based MPPT approaches can be found. For instance, in [Dur06] a model-based approach, depending on the assigned PV module characteristic, is presented. In [JBSLORGL10] the PV array current is not sensed, but it is reconstructed through a sliding-mode observer of the dc/dc converter's input inductor current and fed into the controller to generate the maximum power point reference voltage.

Although a reliable and fast MPPT algorithm can be designed by using the approaches mentioned above, its efficiency is strongly

affected by disturbances generated at the DC/DC converter output, thus at the DC bus, and due to the inverter operation or to other generators and/or loads connected at the same DC bus terminals.

1.3.2 Rejection of disturbances affecting the MPPT efficiency

The MPPT efficiency maximization requires a robust and efficient control in terms of disturb rejection. A classical grid connected PV system includes a dc/dc stage and a dc/ac converter, connected through a dc-link whose voltage is generally stabilized by a bulk capacitor (Cb in Fig.1.8). In single phase applications, but also in three phases ones, the inverter operation generates an oscillation of the voltage of the bulk capacitor at a frequency equal to the double of the line frequency and with an amplitude that is inversely dependent on the capacitance[KPB05]. The whole PV power processing system in fact generates dc and pulsating power, at twice of the line voltage frequency, into the grid, so inevitably the oscillation back-propagates and affects the PV voltage, thus degrading the MPPT performances and the global efficiency [PST$^+$08]. Traditionally, these drawbacks are overcome by choosing a high value of the DC-link capacitance: employ an electrolytic capacitor increase cost and result in a possible reduction of the system reliability[PST$^+$08], while adopt of non-electrolytic capacitors would lead to an expensive implementation, because a high capacitance value operating at a high voltage is needed.
Different topologies are proposed in literature aimed at reducing or eventually removing the DC link capacitor, but at the price of a lower efficiency or of an additional switching circuit, with an increased complexity in terms of layout and control techniques and, of course, with additional costs [XCK$^+$04], [LW08]. A different approach avoids the drawbacks of the passive filtering by using the voltage oscillations affecting Cb to create a proper control strategy to be applied to the DC/DC converter allowing a smaller, and also cheaper and more reliable, value of capacitance. A first

approach proposed in [FPSV09] guarantees satisfactory filtering performances by means of a carefully designed additional analog feedback loop controlling the DC/DC converter. Other approaches ensure high performances adopting low cost solutions using digital control[FPSV09]. In [KKN09] was proposed a feed-forward approach ensuring the cancelation of the low frequency voltage oscillations at the PV array terminals. Such solution is based on a digital controller and does not require an accurate knowledge of the PV system parameters; nevertheless, it involves a phase locked loop for the grid frequency synchronization. It is based on an idea that was introduced in [BBR+02], where the feed-forward compensation was used to regulate the DC/DC converter input current value.

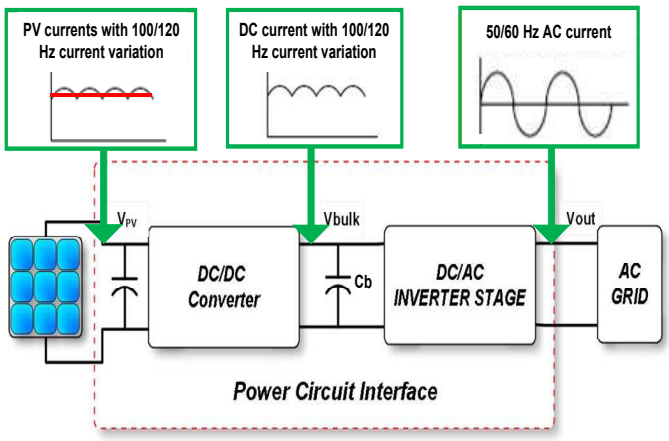

Figure 1.8: PV grid connected power processing system.

1.4 Non linear MPPT control

Non linear control techniques can be very useful for both MPPT and disturbance rejection operations in PV power processing systems because of its capability to improve the dynamic perfor-

mance. Typical non-linear control approach applied to the switching converters are, for example, One-Cycle control, Peak and Valley Current controls, Constant On time and Constant off time controls. All these techniques are theoretically well formalized and widely used in practical implementations. The sliding mode (SM) approach offers an alternative way to implement a control action that exploits the inherent variable structure nature of switching converter. It represents an effective control method which provides extreme robustness and fast response not only in applications involving switching converters but also for more complex power electronic systems. Unfortunately, many discussions regarding the usefulness and advantages of SM controllers have been proven theoretically but not yet consolidated in practical applications. This because there is a lack of understanding in SM design principle by power-supply engineers and for the absence in literature of a systematic procedure for the system design. Moreover, unlike PWM controllers, the SM controllers are not available in integrated-circuit (IC) for power-electronic applications. For these reasons the use of the SM control in DC/DC converters is almost limited.
An objective of this thesis is to analyze the different aspects concerning SM controllers in DC/DC converters, giving a procedure to design SM controlled converters and showing practically the benefits concerning this type of control especially for PV applications.
Although many research publications are available in the literature on the SMC, those ones focused in photovoltaic applications are few and mainly devoted on the control of the DC/AC stage for regulating the current injected into the grid [WWL08], [WW08] or devoted to perform the Maximum Power Point Tracking (MPPT)[KKY06] as alternative to other MPPT techniques like the Perturb and Observe (P&O) and the Incremental Conductance (INC). In this thesis the SMC is used with the specific objective to regulate the PV source in order to reject all disturbances which might appear at the converter output and assures an optimal regulation of the electrical variables at the PV terminals.

1.4.1 Sliding Mode control

Switching converters are systems whose physical structure is intentionally changed during the transient in accordance with a preset structure control law. From this point of view, they represent a particular class of variable structure system (VSS), since their structure is periodically changed by the action of controlled switches and diodes. The time instants, at which the control action of changing the structure occurs, are not determined by a fixed program, but in accordance with the current state of the system. This property distinguishes VSS from programmed controllers.
In general we may state that VSS consist of a number of well defined elements, linear or nonlinear. Under control action the elements may be configured into a number of possible well defined independent substructures. The theory of VSS provides a systematic method of defining such systems using discontinuous variables, known as switching variables, and selecting a rational control law to pick out the substructure used at any instant in order to achieve the control objective. In order to study such systems, it is advantageous to select a system description where time information is suppressed or implicit. The phase plane description satisfies this condition and provides valuable insight into the various aspects pertaining to VSS[UGS09].

1.4.2 The Phase Plane for sliding mode control analysis and design

The phase plane analysis technique is a graphical method widely used in the study of non-linear systems of the second order and brings out the features of sliding mode control remarkably well. The axes of the phase plane are the system states. The instantaneous state of the system is represented on the phase plane by a Representative Point (RP) whose coordinates on the phase plane are the present states of the system. The basic idea is to graphically solve the equation of state of the system rather than deter-

mine an analytical solution. The study of the system involves the motion of the RP on the phase plane under different input and initial conditions. The evolution on the phase plane of the system states with respect to time, referred to the phase trajectories or the state trajectories, represent the dynamic properties of the system. For a given system, the phase trajectories are a family of curves satisfying the dynamic properties of the system. In the case of VSS, the phase plane description consists of a set of a family of phase trajectories, one for each of the substructures used. The analysis problem of VSS is to study the overall system behavior under a given structure-control law. The design problem in VSS is to develop a rationale to synthesize a structure-control law in order to achieve the performance objectives of the overall system. More details on this aspect can be found in [UGS09].

For example consider the following two substructures given by

$$SubI \rightarrow \begin{cases} \dot{x}_1 = x_2 \\ \dot{x}_2 = -2\zeta x_2 - x_1 \end{cases} \tag{1.1}$$

With:

$$-1 < \zeta < 0 \tag{1.2}$$

The eigenvalues of substructure I are complex with positive real parts. The phase trajectories of this substructure are shown in Fig.1.9(a) The trajectories are diverging logarithmic spirals and the substructure I is unstable. Substructure II is given by

$$SubII \rightarrow \begin{cases} \dot{x}_1 = x_2 \\ \dot{x}_2 = -2\zeta x_2 + x_1 \end{cases} \tag{1.3}$$

With:

$$q_1 = -\zeta + \sqrt{1+\zeta^2}; q_2 = -\zeta - \sqrt{1+\zeta^2} \tag{1.4}$$

The eigenvalues of substructure II are real with opposite sign.. The phase trajectories are given in Fig1.9(b). They diverge indicating instability The structure-control law is:

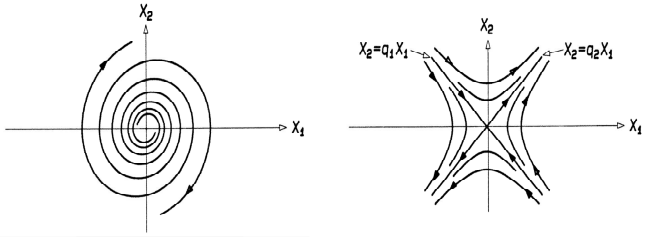

(a) Substrucure I (b) Substrucure II

Figure 1.9: Phase plane analysis

$$\begin{cases} SubI\ holds for \rightarrow x_1 \cdot (x_2 + cx_1) > \delta \\ SubII\ holds for \rightarrow x_1 \cdot (x_2 + cx_1) < \delta \end{cases} \tag{1.5}$$

With:

$$c > 0; |c| < |q_1| \tag{1.6}$$

The switching boundaries are the $x2$ axis and the straight line $x2 + cx1 = 0$. The line $x2 + cx1 = 0$ is the switching line. The idealized switching boundaries, the substructures active in the various regions of the phase plane, and the trajectories in each of the regions of the phase planes are all shown in Fig.1.10. The structure changes whenever the Representative Point (RP) enters a region defined by the switching boundaries. In the proximity of the switching line the phase trajectories converge to the switching line. The immediate consequence of this important property of the phase trajectories of the substructures is that, once the RP hits the switching line the structure-control law ensures that the RP does not move away from the switching line. Fig.1.10(b) shows a typical trajectory starting from an arbitrary initial condition $A(x_{11}, x_{21})$. The resultant trajectory is seen to be confined along the switching boundary $x2 + cx1 = \delta$. Fig.1.10(c) shows the same trajectory when the non idealities of the switching boundaries approach zero ($\delta = 0$). In the case of ideal switching it may be seen that once the RP moves onto the switching line $x2 + cx1 = 0$, the system motion is then along the switching line. The switching line

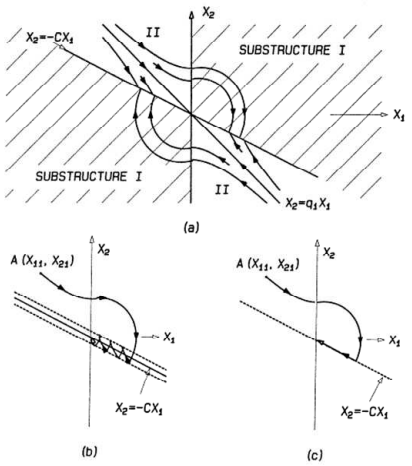

Figure 1.10: Idealized switching boundaries

$x2 + cx1 = 0$ is defined by the structure-control law and doesn't belong to the trajectories of any of the substructures of the VSS. This motion of the system RP along the new trajectory, on which the structure of the system changes, and that is not part of any of the substructure trajectories, is called the sliding mode. This property is one of the strongest features of VSS. When sliding modes exist, and are exploited, the resultant system performance is independent of the properties of the substructures employed and depends only on the preset structure-control law.
The design of such strategies is performed in two steps [SM01]. The first step concerning the selection of the sliding surface that providing the desired asymptotic behavior when the converter dynamics is forced to evolve over it. In the second step, the feedback circuit which addresses the converter dynamics to the sliding surface is designed. The main advantages of sliding-mode control over conventional PWM control are stability, even for large supply and load variations, robustness, good dynamic response, and simple implementation [UGS09] [SR87] [WL10]. However, sliding-mode control presents some drawbacks: the switching frequency depends on the working point, due to the control hysteretic nature, steady-state errors can appear in the output response [DT09] and

a significant overshoot in the state variables might arise during the converter transient regime.

1.4.3 Digital implementation of a sliding mode controller

Digital control of switch mode power supplies (SMPS's) is more and more used because of the increased computational capabilities and of the reduced cost of the devices available on the market. In general, the noise immunity and the high flexibility of the digital controls are additional benefits that increase the interest towards such a solutions. On the other side, the new generation of SMPS must assure high dynamic performances that can be achieved only by employing non-linear control techniques ensuring a controller bandwidth which is comparable with the switching frequency. Unfortunately, the performances such control techniques are able to guarantee are strongly affected by delays and errors the digital implementation might introduce. As a consequence, on the basis of the specific digital platform used to implement the controller (FPGA, DSP, ASIC, micro-controller), such aspects must be properly managed in order to avoid the degradation of the control performances. Typical instability phenomena related to the quantization effect are well described in [PS03], wherein guidelines for removing such instability in PWM-based controllers have been also proposed.
There are a lot of commercial integrated circuits for dc-to-dc switching conversion control developed in the last years. A great number of these circuits perform PWM control in either voltage or current mode with both reference voltage and switching frequency externally adjustable,and can be chosen according to power supply specifications, i.e., input and output voltage levels, converter topology, control strategy, output power, etc.
There are some integrated controllers that use hysteresis comparators to generate the on/off power transistor control signal. In some cases, the power switch is also integrated in the same controller circuit. Nevertheless, the hysteresis width is fixed in all cases and,

besides, external signal processing is required to close the control loop. Therefore, if sliding-mode control is implemented through these available hysteresis controllers, some drawbacks will arise, mainly due to the fixed hysteresis width and the need of designing external networks for voltage regulation.
To obtain a wide use of the sliding mode control it is preferable to implement a controller in a low cost digital device. In [LGLSA11] an improved digital pulse-width-modulator (DPWM), which takes advantage of FPGA's attractive features in order to implement the SM controller for a boost converter, has been proposed. The paper discusses a way for alleviating the quantization effects due to the DPWM and the SM control equation is translated in its equivalent digital representation. In [GLSA$^+$10] the same FPGA-based SM controller has been developed by using a fully digital implementation in which external ADC's are used for having a 10-bit, 40 MSPS sampling rate. Such a solution takes advantage of a fast analog to digital conversion which simplifies the implementation of the SM control law, but the cost of the FPGA device is high if compared with the cost of the power stage of any DC/DC converter for low power applications. In [LLSL$^+$11] the application of the fixed frequency, or indirect, SM control to a SEPIC dc/dc converter has been proposed. The system has been tested by using both a DSP and an FPGA board. In the latter case, only the output voltage is measured and a Kalman observer is proposed to estimate the other state variables. As expected, the reduction in the number of sensor is paid with a more complex control strategy which requires additional computational resources that are available only in more expensive devices.
The approaches referenced above have the feature of flexibility, but they are suitable when the cost is not the main priority.
The control technique proposed in [VICCMS11] does not require the high frequency sampling of the signals. It is based on a prediction of the time instant in which the switch commutations must be performed. This instant is analytically estimated by using only one or two samples of the control signals in each switching period. In this case the limitation is related to the time delay and to calcu-

lation time needed for estimating the commutation instant: this time might be too long if a low cost micro-controller should be used. In [VIMSG+04] the SM control joins a fuzzy logic mechanism, with a PI controller that guarantees the output voltage regulation and an excellent transient response during start-up. The SM control requires usual analogue devices and the fuzzy logic voltage regulator has been implemented by using a cheap 8-bit micro-controller.
Papers [YUO99] and [Ś11] give an overview of the application of Variable Structure Systems (VSS's) with SM methods in discrete-time. The authors discuss how to design the SM control by means of the sampled data model and they also give an outline of the so-called *chattering* problem. This is an undesired oscillation phenomenon having finite frequency and amplitude and appearing when the SM control is practically implemented. It reduces the control accuracy and increases heat losses in power circuits.
Generally there are two reasons that lead to chattering: the *unmodeled* dynamics, that are the small time constants which were usually neglected in the ideal model, and the adoption of digital controllers with a finite sampling rate, which causes the so-called *discretization chatter*. In[DT09], several chattering suppression methods for DSP based SM control implementation have been discussed. Special attention has been devoted to the *equivalent-control-dependent* and *state-dependent* gain adjustment methods, which have been proposed in recent theoretical studies. The well known observer-based method was also used for purposes of comparison. Additionally, the effect of an increased sampling rate on the amplitude of discretization chattering was examined. These methods may exhibit unsatisfactory results when performed separately, so that various combinations of them are tested in order to find the best solution for chattering elimination. This approach may increase the complexity of the control structure, but preserves the advantages of SM methodology. In this work a novel hybrid analog-digital implementation will be developed for the SM control. Its main advantage is in the possibility to use low cost micro-controller thus easily integrated on the DC/DC converter board.

This circuit will be used for validating the theoretical analysis proposed in the next chapters. Details about the implementation will be proposed in.

Chapter 2

A fast current-based MPPT technique employing sliding mode control

A typical control strategy operating on the inductor current of a DC/DC converter in order to regulate the PV current value is showed in Fig. 2.1.

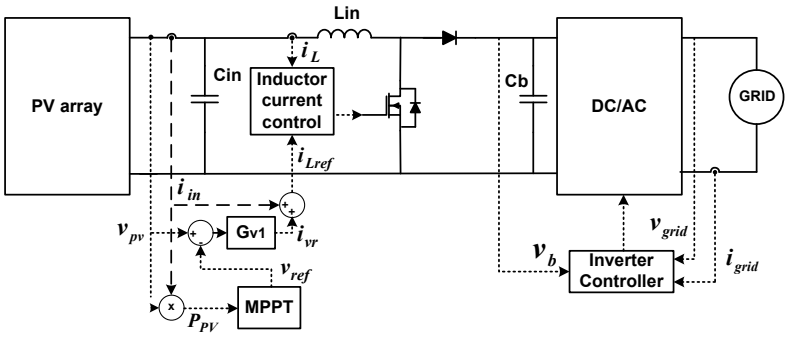

Figure 2.1: System scheme.

The role of the input capacitor C_{in} is that of absorbing the switching ripple affecting the inductor current, so that the PV current control is obtained by acting on the average inductor current. In the circuit node connecting the PV array, the boost converter input inductor L and capacitor C_{in} (see Fig. 2.1), the Kirchhoff current law holds:

$$i_{in} = i_{C_{in}} + i_L \tag{2.1}$$

The current controller gives the reference current i_{Lref}:

$$i_{Lref} = i_{in} + i_{vr} \tag{2.2}$$

where i_{in} is the actual PV current and i_{vr} is the output of the compensator $G_{v1}(s)$ (see fig.2.1). The feedforward action on i_{in} considered in (2.2) helps in detecting the irradiation variations promptly. In steady-state conditions, it is $i_{in} = i_{Lref}$ and $i_{vr} = 0$.

According to the classical DC/DC converters current control theory, the signal $u(t)$ driving the MOSFET is a function of the error signal $e_i(t) = i_{Lref}(t) - i_L(t)$, so that the inductor current i_L is regulated according to the current reference signal i_{Lref}. By using (2.1) and (2.2), the following simplification is thus possible:

$$i_{Lref} = i_{C_{in}} + i_L + i_{vr} \tag{2.3}$$

$$e_i = i_{C_{in}} + i_L + i_{vr} - i_L \tag{2.4}$$

$$e_i = i_{C_{in}} + i_{vr} \tag{2.5}$$

where the control objective $i_{Lref} = i_L$ (see Fig. 2.1) leads to $e_i = 0$, so that it is equivalent to:

$$i_{C_{in}} = -i_{vr} \tag{2.6}$$

and the steady-state condition results in $i_{C_{in}} = 0$.

The simplified control objective (2.6) reveals that the control structure of Fig. 2.1 can be simplified as in Fig. 2.2, with the inner control loop which is now aimed at regulating the input capacitance current $i_{C_{in}}$. This simplification is important because the practical implementation of the scheme shown in Fig. 2.1 would

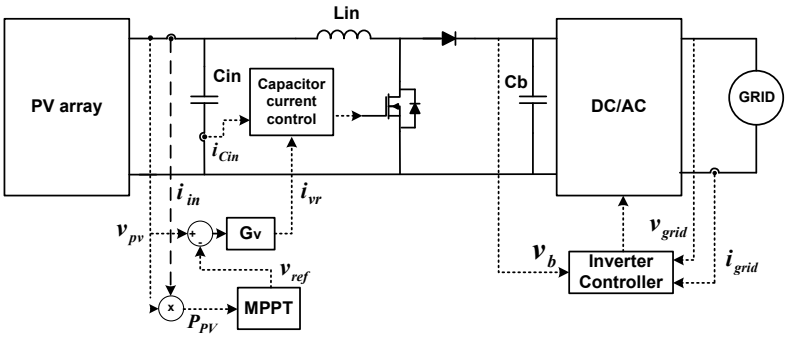

Figure 2.2: System scheme based on input capacitor current control.

require two high-bandwidth current sensors for i_{in} and i_L, both affecting the value of the MOSFET control signal $u(t)$. Instead, in the scheme of Fig. 2.2, $u(t)$ only depends on the instantaneous value of $i_{C_{in}}$. Consequently, only one high-bandwidth current sensor is required because the other one is a low-bandwidth one dedicated to i_{in}, In fact the MPPT controller block of Fig. 1 is characterized by a slow dynamics [FPSV05]. Additionally, the capacitor current sensing is made easier than the inductor current one due to the fact that the former has a zero DC component. Another advantage of the system shown in Fig. 2.2 is in its easier analysis with respect to that one depicted in Fig. 2.1.

2.1 Sliding-mode-based MPPT

The switching function S is given in (2.7):

$$S = -i_{C_{in}} - i_{vr} \tag{2.7}$$

It is defined in order to fulfill the control objective (2.6). The current loop reference i_{vr} in the scheme of Fig. 2.2 is given by

$G_v(s)$. The definition of the sliding surface S as in (2.7) suggests that, in sliding-mode operation, the capacitor current $i_{C_{in}}$ changes in order to reject the perturbations on the bulk capacitor voltage v_b and to track the perturbations in the irradiance level. Thus, the fact that S does not depend on those variables ensures the MPPT operation and the rejection of the low frequency disturbances, at a frequency that is twice the grid one, in single phase AC applications.

Two conditions must be fulfilled in order to ensure the sliding-mode operation [TLT08]:

$$S = 0 \tag{2.8}$$

$$\frac{dS}{dt} = 0 \tag{2.9}$$

From the first condition (2.8), and by accounting for the characteristic equation of the input capacitor:

$$i_{C_{in}} = C_{in} \cdot \frac{dv_{PV}}{dt} \tag{2.10}$$

the following condition is obtained:

$$\frac{dv_{PV}}{dt} = -\frac{i_{vr}}{C_{in}} \tag{2.11}$$

In sliding mode operation, eq.(2.11) gives the relation between the PV voltage and the reference current, so that, as it will be shown in the following, it allows to design the voltage compensator.

From the second sliding-mode condition (2.9), and by considering that $i_{C_{in}} = i_{in} - i_L$, we get:

$$\frac{dS}{dt} = \frac{di_L}{dt} - \frac{di_{in}}{dt} - \frac{di_{vr}}{dt} = 0 \tag{2.12}$$

By neglecting the series and parallel resistances of the PV array, namely $R_s = 0$ and $R_{sh} = \infty$, the PV current can be approximated by the expression:

$$i_{in} = i_{PV} - I_R \cdot e^{a \cdot v_{PV}} \tag{2.13}$$

where v_{PV} is the PV voltage, I_R and a are parameters depending on the adopted PV modules, i_{PV} is the short-circuit current for a given irradiance level, which is approximately proportional to the irradiance $i_{PV} = k_G{\cdot}G$ [U.E03]. In fact, the short circuit current at the desired value of temperature and irradiation can be calculated as a function of the values of the same quantities in the Standard Test Conditions (STC) and by using the value of α_I, which is given in any PV module data sheet and expressing the sensitivity of the short circuit current with respect to the temperature [U.E03]:

$$i_{PV} = i_{PV,STC} \cdot \frac{G}{G_{STC}} \cdot (1 + \alpha_I \cdot \big(T_{PV} - T_{PV,STC}\big)) \qquad (2.14)$$

The analysis of the equation (2.12) can be done by using the small-signal model shown in Fig. 2.3, wherein the switching converter is represented by a current source and the PV generator is given as a Norton model including the photoinduced current source and the differential resistance R_{diff} which is calculated in the generator's operating point.

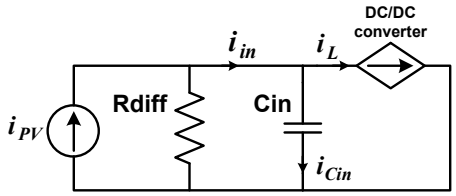

Figure 2.3: Small-signal model of the open-loop system. It is $I_L = i_{in} - i_{Cin} = i_{in} - G_v \cdot (V_{pv} - v_{ref})$.

By looking at Fig. 2.3 and (2.13), it results:

$$\left.\begin{aligned} \frac{di_{in}}{dt} &= -\frac{1}{R_{diff}} \cdot \frac{dv_{PV}}{dt} + \frac{di_{PV}}{dt} \\ \frac{1}{R_{diff}} &= a \cdot I_R \cdot e^{a \cdot v_{PV}} \end{aligned}\right\} \qquad (2.15)$$

As a result, the sliding-mode condition given in (2.12) can be thus rewritten as:

$$\frac{di_L}{dt} + \frac{1}{R_{diff}} \cdot \frac{dv_{PV}}{dt} - \frac{di_{PV}}{dt} - \frac{di_{vr}}{dt} = 0 \tag{2.16}$$

In addition, the classical boost converter model gives the following relationship:

$$\frac{di_L}{dt} = \frac{v_{PV}}{L} - \frac{v_b \cdot (1-u)}{L} \tag{2.17}$$

where v_b is the dc/dc converter's output voltage and the value $u = 1$ is used in the MOSFET ON state and the value $u = 0$ in the OFF state.

Since $S = 0$ is required, by taking into account (2.1) and (2.6), if $S < 0$, or $i_{C_{in}} > -i_{vr}$, then the inductor current i_L must be increased in order to decrease $i_{C_{in}}$, so that from (2.17) $u = 1$ is required. On the other side, if $S > 0$, or $i_{C_{in}} < -i_{vr}$, then the inductor current i_L must be decreased in order to increase $i_{C_{in}}$, so that from (2.17) $u = 0$ is required. Finally, it is [UGS09]:

$$u = 1 \quad if \quad S < 0 \tag{2.18}$$
$$u = 0 \quad if \quad S > 0 \tag{2.19}$$

In order to obtain the constraints that must be fulfilled in order to ensure the sliding-mode operation, the equivalent control technique [SR87] can be used. The constraints on the inputs and states are defined by ensuring that the average control signal u_{eq} fulfills the inequality $0 < u_{eq} < 1$. From equations (2.11)-(2.17) the following equivalent control equation is obtained:

$$\frac{v_{PV}}{L} - \frac{v_b \cdot (1-u_{eq})}{L} + \frac{1}{R_{diff}} \cdot \frac{dv_{PV}}{dt} - \frac{di_{PV}}{dt} - \frac{di_{vr}}{dt} = 0 \tag{2.20}$$

From (2.7) and (2.12) it is deduced that the sliding-mode equilibrium point is defined by $\{i_{in} = i_L,\ i_{vr} = 0\}$. In (2.20), at the

equilibrium point it is $\frac{dv_{PV}}{dt} = 0$, while the constraints to be fulfilled in terms of maximum slope values of i_{vr} and irradiance, $\frac{di_{vr}}{dt}$ and $\frac{dG}{dt} = \frac{1}{k_G} \cdot \frac{di_{PV}}{dt}$, ensuring the sliding-mode operation are calculated by using the superposition principle. The latter is used by assuming that the two variations, affecting the irradiance level and the reference signal, do not occur at the same time. Consequently, the boundaries that are determined by means of the analysis that follows are the maximum allowable variations admitted on the irradiance and the reference signal.

Thus, by putting $\frac{di_{vr}}{dt} = 0$ in (2.20), the effect of the i_{PV} variations ensuring that $0 < u_{eq} < 1$ leads to the inequality:

$$0 < \frac{v_{PV} - L\frac{di_{PV}}{dt}}{v_b} < 1 \tag{2.21}$$

so that the two following inequalities ensure that the sliding mode control of the converter is preserved:

$$v_{PV} - L\frac{di_{PV}}{dt} > 0 \tag{2.22}$$

$$v_{PV} - L\frac{di_{PV}}{dt} < v_b \tag{2.23}$$

Finally, the constraint to be fulfilled on the i_{PV} slope in order to guarantee the proper sliding mode operation is obtained:

$$\frac{v_{PV} - v_b}{L} < \frac{di_{PV}}{dt} < \frac{v_{PV}}{L} \tag{2.24}$$

It is worth noting that the lower bound for the i_{PV} slope in (2.24) is negative because of the adoption of a boost converter. This means that the larger the converter's voltage boosting factor, the faster negative short circuit current variation can be tracked without loosing the sliding mode behavior. This might be the case of a step-up dc/dc converter used in PV module dedicated microinverter applications, in which the low PV module voltage must be boosted up significantly, so that the quantity $\frac{v_{PV}-v_b}{L}$ is deeply negative.

Due to the proportionality between i_{PV} and the irradiance S, condition (2.24) can be translated into a constraint for the maximum irradiance variation the MPPT technique is able to track:

$$\frac{v_{PV} - v_b}{L \cdot k_G} < \frac{dG}{dt} < \frac{v_{PV}}{L \cdot k_G} \tag{2.25}$$

Inequality (2.25) reveals that the maximum irradiance variation that can be tracked without loosing the sliding-mode control is bounded by the inductor current derivatives in the OFF and ON MOSFET states. This means that the inductance value L should be properly designed in order to follow the expected irradiance profile and variations, according to the specific applications. For instance, stationary PV power plants will be subjected to slow irradiance variations, while in PV applications dedicated to sustainable mobility fast irradiance variations need to be tracked.

By fixing $\frac{di_{PV}}{dt} = 0$ in (2.20), the effect of variations on i_{vr} can be accounted for, so that the following constraint on $\frac{di_{vr}}{dt}$ is obtained:

$$\frac{v_{PV} - v_b}{L} < \frac{di_{vr}}{dt} < \frac{v_{PV}}{L} \tag{2.26}$$

which again shows that the maximum i_{vr} slope value that can be tracked without missing the sliding-mode control depends on the inductor current derivatives in the OFF and ON MOSFET states. In this case, the voltage controller can be designed to fulfill this dynamic constraint.

It is worth noting that, due to the symmetry of the expression (2.20), constraints (2.25) and (2.26) show the same boundaries.

When both (2.24) and (2.26) conditions are fulfilled, the converter is in sliding-mode control and therefore the dynamics of the system is given by (2.11).

The transfer function $G_{v/i}(s)$ between the input capacitor voltage, that is the PV voltage, $v_{C_{in}}$ and the current reference i_{vr} provided by the voltage controller is:

$$G_{v/i}(s) = -\frac{1}{C_{in} \cdot s} \tag{2.27}$$

This expression allows to point out one of the main features of the proposed control technique. Indeed, it is worth noting that the transfer function (2.27) is not dependent on any PV generator's parameter, so that the control approach can have the same performances regardless of the PV array type/size connected at the dc/dc converter's input terminals. This feature is not achieved through classical control approaches [FPSV05].

2.1.1 PI controller design

The controller block G_v of Fig. 2 is a traditional PI compensator. By taking into account the PI transfer function $G_v(s)$ given in (2.28) and the voltage error $E_v(s)$ definition (2.29) that compensates the negative sign appearing in (2.27), the closed loop transfer function $T(s)$ of the system can be expressed as in (2.30):

$$G_v(s) = k_p + \frac{k_i}{s} \tag{2.28}$$

$$E_v(s) = -(V_{ref}(s) - V_{C_{in}}(s)) \tag{2.29}$$

$$T(s) = \frac{V_{PV}(s)}{V_{ref}(s)} = \frac{k_p s + k_i}{C_{in} s^2 + k_p s + k_i} \tag{2.30}$$

The transfer function $T(s)$ in (2.30) is designed by accounting for a classical relation between the settling time t_S of the closed loop voltage and the minimum switching period T_{sw}.

The $T(s)$ structure gives the following relations:

$$k_p = 2C_{in}\zeta\omega_n \tag{2.31}$$

$$k_i = C_{in}{\omega_n}^2 \tag{2.32}$$

so that, by using the equivalent time constant definition, it is $\tau = \frac{1}{\zeta\omega_n}$.

It must be pointed out that the designed PI controller allows to meet all the desired performances. Nevertheless, at the price of a steady state error, a simpler pure proportional controller might be used, the error being compensated by the MPPT operation.

2.1.2 MPPT refinements: input and output signals filtering

The MPPT controller adopted in this example is a traditional Perturb and Observe (P&O) one. This means that the P&O output generates a step change in the v_{ref} signal of the voltage controller, thus violating the constraint on $\frac{di_{vr}}{dt}$. In order to avoid this drawback, the P&O output is filtered thus generating a dynamic behavior of v_{ref} that is comparable with that one of the closed loop system. In this way, the first order filter $G_{fv}(s)$ given in (2.33) is used,

$$G_{fv}(s) = \frac{V_{ref}(s)}{\mathsf{P\&O(s)}} = \frac{1}{\tau_f s + 1} \tag{2.33}$$

where $\mathsf{P\&O(s)}$ is the P&O control signal.

The P&O filter dynamics (2.33) exhibits a time constant τ_f that is related to the slope of the unitary-step time response. By considering that the P&O MPPT controller applies a perturbation of amplitude Δv_{ref}, the maximum slope of the voltage reference is:

$$\frac{\Delta v_{ref}}{\tau_f} = \left.\frac{dv_{ref}}{dt}\right|_{max} \tag{2.34}$$

By keeping into account the transfer function (2.28) of the PI voltage controller adopted in this numerical example and by considering the sliding-mode equilibrium point ($v_{C_{in}} = v_{ref}$, $\frac{dv_{C_{in}}}{dt} = 0$), the derivative of i_{vr} is given as follows:

$$\frac{di_{vr}}{dt} = -k_p \cdot \frac{dv_{ref}}{dt} \tag{2.35}$$

There is a need to filter signals v_{PV} and i_{in} at the MPPT input too. In fact, the possibility of reducing the amplitude of the perturbations given by the P&O algorithm determines the corresponding reduction of the v_{PV} and i_{in} perturbations, with

a beneficial effect on the MPPT efficiency. The PV current and voltage measurements used to calculate the PV power needed by the P&O controller can be filtered by using the same $G_{fv}(s)$ to remove the switching frequency components without degrading the dynamic response of the system, thus avoiding the P&O controller to be confused by the switching ripple. The Δv_{ref} perturbation generated by the P&O controller can be adopted equal to the voltage ripple, which is mitigated due to the PV voltage filtering. The PV voltage ripple Δv_{PV} is calculated as [EM01]:

$$\Delta v_{PV} = \frac{H \cdot T_{sw,max}}{8C_{in}} \tag{2.36}$$

where H is the inductor current ripple.

2.2 Simulation results

Some simulation results have been obtained in PSIM environment. In Fig. 2.4 the complete PSIM schematic has been shown.

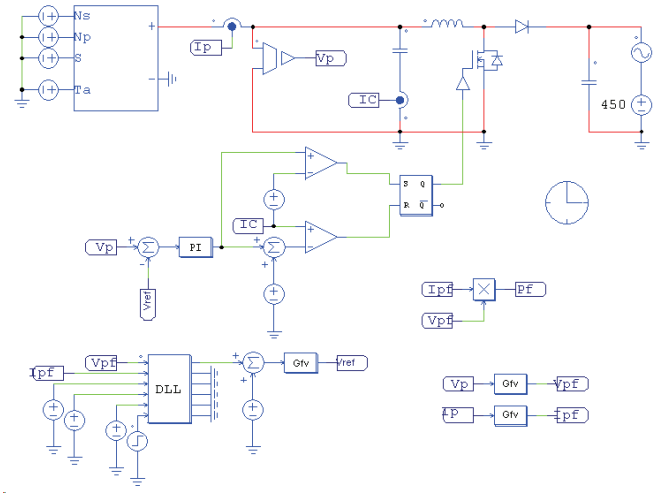

Figure 2.4: Complete PSIM schematic.

The input capacitance value has been assumed equal to $C_{in} = 50\ \mu\mathsf{F}$, the input inductance $L = 410\ \mu\mathsf{H}$, with a desired inductor current ripple $H = 4\ \mathsf{A}$. The minimum PV voltage value has been fixed at $v_{PV,min} = 100\ V$, and a bulk capacitor $C_b = 22\ \mu\mathsf{F}$ with an average voltage $v_{b0} = 450\ \mathsf{V}$ has been considered.

With the system operating in sliding-mode, the steady-state duty cycle $D(t)$ and switching frequency $f_{sw}(t)$ will oscillate around their nominal values D_0 and f_{sw0}, respectively, in order to cancel out the bulk capacitor voltage oscillations $\Delta v_b(t)$ according to the following formulas:

$$D(t) = 1 - \frac{v_{PV}}{v_{b0} + \Delta v_b(t)} \quad , \quad D_0 = 1 - \frac{v_{PV}}{v_{b0}} \tag{2.37}$$

$$f_{sw}(t) = \frac{v_{PV} \cdot D(t)}{H \cdot L} \quad , \quad f_{sw0} = \frac{v_{PV} \cdot D_0}{H \cdot L} \tag{2.38}$$

According to (2.38), the minimum switching frequency is equal to 40 kHz. With such values, from (2.36) it results that $\Delta v_{ref} = \Delta v_{PV} = 0.2\ \mathsf{V}$.

In order to put into evidence one of the main features of the proposed approach, i.e. the ability of rejecting the low frequency voltage variations backpropagating from the bulk voltage towards the PV voltage, $\Delta v_b(t)$ has been assumed to oscillate in the range [-160, 160] V, so that $\Delta v_b = 160\ V$.

The considerations done above about the PI controller design lead to a maximum switching period $T_{sw,max} = 25\ \mu\mathsf{s}$ so that, by choosing $t_S/T_{sw,max} = 8$, where ts is the closed loop settling-time, we get $t_S = 200\ \mu\mathsf{s}$, which is the first design consideration for the PI controller. The second design consideration is related to the damping of the system, which can be adjusted by choosing $\zeta = 0.7$. Named τ is the equivalent time constant of the closed loop system, by approximating t_S as 4τ, so that the settling error step response is smaller than 2%, it results that the PI controller that ensures the defined t_S and ζ is the following one:

$$G_v(s) = 2 \cdot \frac{s + 20408.16}{s} \tag{2.39}$$

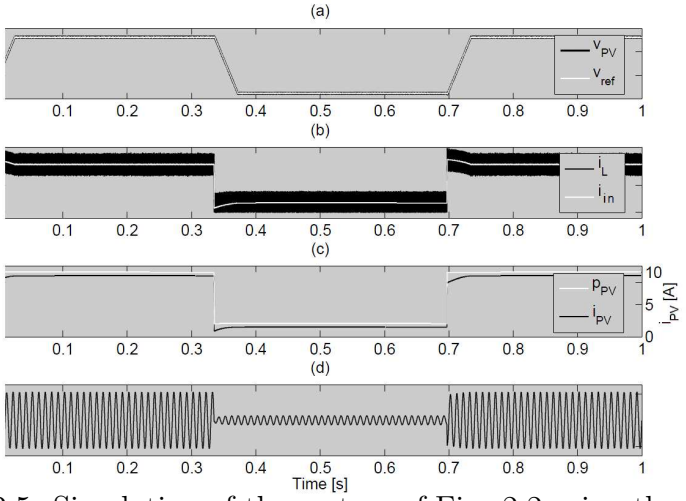

Figure 2.5: Simulation of the system of Fig. 2.2 using the sliding-mode and G_v controllers.

which also provides an infinite gain margin and a phase margin equal to 65.2 °.

The PI design from the t_S specification also allows to define the MPPT controller period T_a equal to the v_{PV} stabilization time, that is $1.5 \cdot t_S$ approximatively. Such a value of T_a ensures that the PV power has reached its steady state when the MPPT controller measures it, thus avoiding the MPPT deception [FPSV05]. In this example $T_a = 300$ μs.

As for the signal filtering, the time constant in (2.33) is set to $\tau_f = \tau = 50$ μs.

Fig. 2.5 shows the results of the simulation of the system of (Fig. 2.2) by using the sliding-mode and G_v controllers. First of all, simulation results put into evidence that the large low frequency oscillations affecting the bulk voltage have been rejected at the PV terminals. Moreover, the sudden irradiance variations, having an instantaneous effect on the PV short circuit current, have been correctly tracked, with the system permanently tracking the maximum power point even at the very high rate of irradiance variation which has been considered. The two features listed above

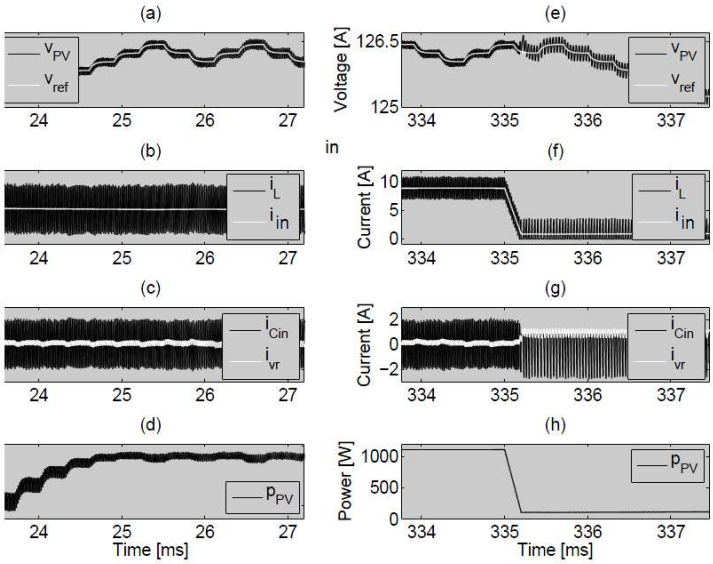

Figure 2.6: Zoom of of Fig. 2.5.

make the control strategy shown in Fig. 2.2 suitable for all the PV applications in which the adoption of electrolytic capacitors at the dc bus must be avoided and/or wherever an excellent MPPT performance is required. Current literature (e.g. [PST+08]) puts into evidence that electrolytic capacitors are the bottleneck of any PV power processing system because they significantly affect its lifetime. The extraordinary fast MPPT capability opens to the PV generators controlled by means of the proposed technique the doors of a large range of applications for which the sudden irradiation changes are very common, e.g. in sustainable mobility and for the PV integration on cars, trucks, buses, ships and so on.

Fig. 2.6 shows the magnification in two different time intervals of the waveforms shown in Fig. 2.5. The first time window is [23.5, 27.2] ms: plots show the system behavior while approaching the steady state operation. Fig. 2.6(a) puts into evidence the proper design of the P&O parameters leading to a three points behavior of the PV voltage. The same figure shows the waveform of the closed loop voltage reference v_{ref} and the accurate tracking

performed by both the $G_v(s)$ and the sliding-mode controller. Fig. 2.6(b) shows that the PV current waveform is free of the 100Hz oscillations due to the inverter operation, thus demonstrating that the control technique has been able to stop the back propagation of the large oscillations of amplitude Δv_b affecting the converter's output voltage. Fig. 2.6(c) shows the input capacitor current and the current reference control signal waveforms. Finally, Fig. 2.6(d) shows that the MPPT technique has been able to drive the system towards the maximum PV power corresponding to the short circuit current of 10 A settled for this simulation example.

Similarly, Figs. 2.6(e)-(h) show a magnification of the system behavior in the time interval [333.6, 337.9] ms, when a high irradiance transient generating a fast reduction (80 %) of the short circuit current has been considered. At the beginning, with $i_{PV} = 10$ A, the converter works in continuous conduction mode and the proper operation of the control algorithm, that is the tracking of v_{ref} and of the PV maximum power point, is evident. Afterwards, at t = 335 ms, the PV short circuit current has been forced to drop suddenly at $i_{PV} = 2$ A, thus simulating a steep reduction in the irradiance level. As a consequence, the converter enters in discontinuous conduction mode at $t > 335$ ms (Fig. 2.6(f)): in this case the switching frequency of the system is reduced, but the voltage controller $G_v(s)$ still drives the PV voltage to follow the MPPT controller reference. Fig. 2.6(e) shows the satisfactory PV voltage behavior in continuous and discontinuous conduction modes, and Fig. 2.6(h) puts into evidence the fast MPPT response under a constant and time varying irradiance levels.

As a final consideration, the upper and lower limits of the slopes $\frac{di_{PV}}{dt}$ and $\frac{di_{vr}}{dt}$ as appear in (2.24) and (2.26) have been calculated for the numerical example considered in this section. In the considered case it must be:

$$-805 \ \mathsf{A/ms} < \frac{di_{PV}}{dt} + \frac{di_{vr}}{dt} < 293 \ \mathsf{A/ms} \tag{2.40}$$

This inequality shows that the most restrictive condition appears when the irradiance level, and thus the short circuit current, is subjected to a positive variation.

By adopting a perturbation amplitude imposed by the P&O MPPT equal to $\Delta v_{ref} = 0.2$ V, which leads to a maximum slope of 4 V/ms, in terms of the boundaries of $\frac{di_{vr}}{dt}$ it results that:

$$\left.\begin{array}{ll} \mathsf{min}\left(\frac{di_{vr}}{dt}\right) = -8\ \mathsf{A/ms} & ,\Delta v_{ref} > 0 \\ \mathsf{max}\left(\frac{di_{vr}}{dt}\right) = 8\ \mathsf{A/ms} & ,\Delta v_{ref} < 0 \end{array}\right\} \tag{2.41}$$

which is two orders of magnitude lower than the limits (2.40) that ensure that the sliding-mode control is still correctly operating. This means that this system is able to track PV short circuit current perturbations with slopes between [-800, 290] A/ms, thus corresponding to very fast irradiance perturbations that are approximately in the range [-80, 29] $\mathsf{W/(m^2 \mu s)}$. Such a remark confirms the inherent bent of the proposed technique for applications characterized by uncommon irradiance slopes.

2.3 Experimental Results

The synchronous boost dc/dc converter shown in Fig.2.7(b) has been developed to test the proposed control method experimentally. As shown in fig.2.7(a), the converter's output terminals have been connected to the series connection of a lead acid battery pack and a four quadrant power amplifier which is used to emulate the 100Hz disturbance which usually appears at the dc/dc converter's output terminals in single stage AC applications. At its input terminals, the boost converter is fed by a low voltage PV module. The PV module and converter parameters' values are listed in Table 2.1. The proposed technique is based on the sliding-mode control of the input capacitor current, whose extreme values hit the thresholds fixed through the comparators thus determining the MOSFET's commutations (see Fig.2.4). Such a need has required a proper design of the capacitor current sensing in order to have an accurate reconstruction of the current ripple at the switching frequency.

The availability of the ground reference, which is one of the advantages of the proposed method which needs to sense the ca-

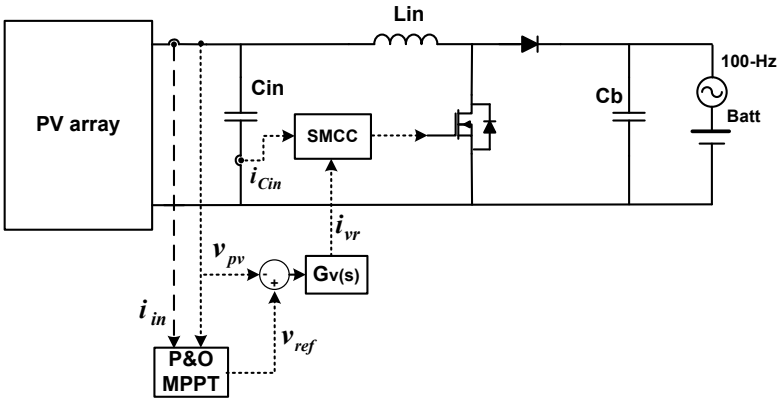

(a) Electrical scheme

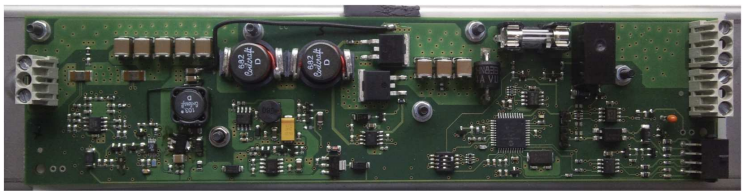

(b) Synchronous boost converter

Figure 2.7: Laboratory prototype: a) Block diagram of the system under test (SMCC stands for Sliding Mode Current Controller). b) PCB board with boost prototype, sensor and control circuits plus auxiliary power unit.

pacitor current instead of the inductor one, has simplified the design of the sensing circuitry made of a cascade connection of a power resistor, a passive low-pass filter, and a wide-band voltage amplifier with a total sensor gain of 1 V/A.

Fig. 2.8 shows the experimental comparison between the capac-

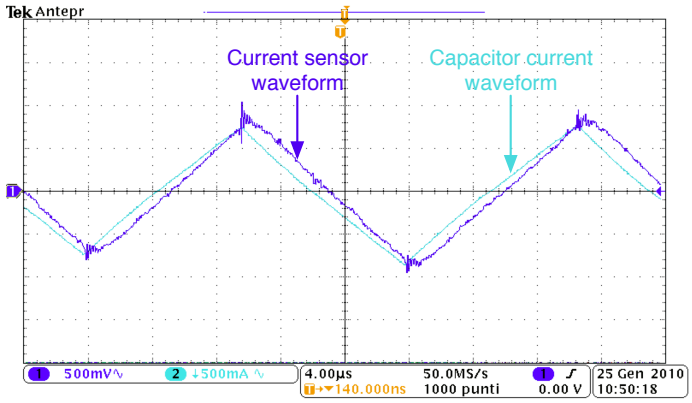

Figure 2.8: Input capacitor current sensing: CH1 is the voltage at the output of the current sensor. Ch2 is the capacitor current measured using the oscilloscope current probe.

itor current measured by a 100 MHz oscilloscope current probe and the corresponding voltage waveform obtained at the output of the current sensor developed on the prototype.

The performances of the control technique presented in this thesis have been studied by means of some experimental tests whose results are described below. The ability in rejecting the 100Hz disturbance at the converter's input terminals has been studied by fixing PV voltage equal to 6 V and the C_b voltage equal to 13.5 V. Fig.2.9 shows the converter's input and output voltage when a reference current value $i_{Lref} = 3A$ is used for the sliding mode controller. A significant oscillation amplitude equal to 6 V peak to peak has been applied in order to demonstrate that the proposed solution does not require a high output capacitance value, so that an almost constant PV voltage is achieved with a large voltage per-

turbation at the dc/dc converter output terminals. The relative bulk voltage oscillation that has been imposed is:

$$\left.\frac{\Delta v_b}{V_{bo}}\right|_{\%} = \frac{6}{13.5} \simeq 45\% \tag{2.42}$$

It is worth noting that the noise rejection performances ensured by the proposed technique have been obtained without using a feedback voltage control, which is only used to adapt the PV voltage to the reference one. On the contrary, as shown in [FPSV09] and in [GPSV10], in order to have the same performances, the classical PWM approach would require a much more involved design of the feedback compensation network.

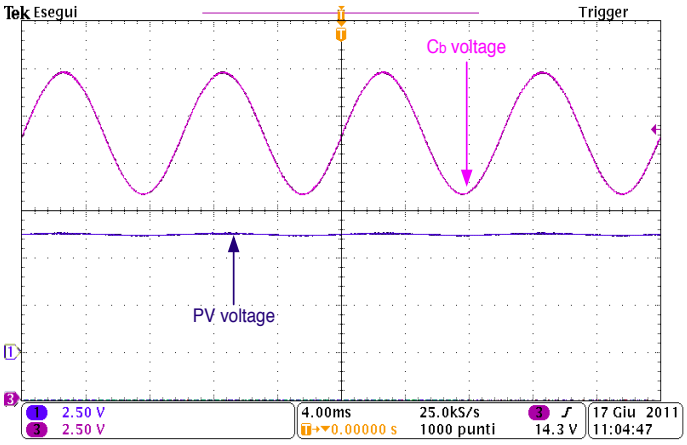

Figure 2.9: 100 Hz compensation by means of the Sliding Mode Control

Just to remark this aspect, in Fig. 2.10 the proposed solution, based on a PI voltage feedback interfaced with the SM control, has been compared with an implementation adopting a classical PID voltage feedback with PWM modulator. Both systems have been designed with a crossover frequency equal to 2 kHz. The

figure shows the system behavior in presence of a 50% irradiance variation; it is evident that the proposed solution leads to a better dynamic response even if a simpler voltage compensation network has been used.

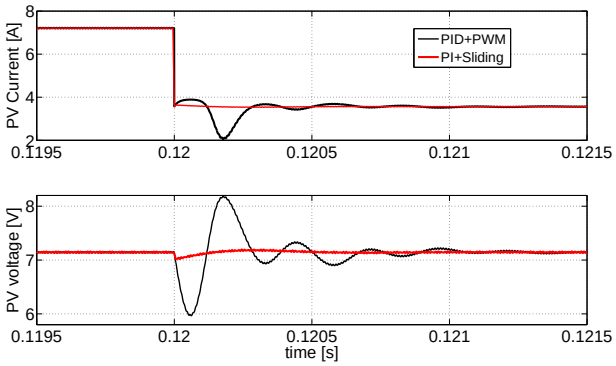

Figure 2.10: PV behavior in presence of a fast irradiance variation

The noise rejection capability of the technique proposed herein is furthermore confirmed by the result shown in Fig.2.9: the insensitivity of the converter's input voltage with respect to sinusoidal disturbances at different frequencies affecting the boost converter output is evident. This characteristic makes the proposed solution effective not only in single phase AC applications, but in any case in which the PV voltage might be affected by noises back propagating from the dc/dc converter output.

As explained in the previous sections, a voltage loop has been used to change the current reference of the sliding mode controller according to the actual value of the irradiance, thus ensuring the "hitting condition" in any operating point. The voltage loop gain has been designed by using the data listed in Table 2.1 for the PV module and by assuming that the boost converter input voltage is in the range [5V,10V] with a nominal value of 8.6V corresponding to the MPP of the PV module. The input voltage sensor divides by 10 the PV voltage in order to assure the right behavior of

compensation network. The designed PI transfer function is the following one:

$$G_v(s) = k_p \cdot \frac{s + k_i}{s} = 0.2 \cdot \frac{s + 10000}{s} \tag{2.43}$$

Fig. 2.11 shows the Bode diagram of the voltage loop gain, which has been obtained by assuming a crossover frequency of 2kHz.

PV array	**Values @ STC**
Short-circuit current I_{STC}	7.7 [A]
Open-circuit voltage V_{OC}	10.8 [V]
MPP current I_{mpp}	7.2 [A]
MPP voltage V_{mpp}	8.6 [V]
Temp. coefficient of I_{SC} (α_I)	0.07 [%/^{o}C]
Temp. coefficient of V_{OC} (α_V)	-0.35 [%/^{o}C]
Boost paramaters	**Nominal values**
input capacitance C_{in}	110 [uF]
output capacitance C_{out}	2 x 22[uF]
inductance L	13.8 [uH]
Operating conditions	**Nominal values**
nominal switching frequency fs	100 [kHz]
average output voltage V_o	13.5 [V]
100-Hz voltage amplitude $vo_{pp,100Hz}$	6 [V]

Table 2.1: Parameters and nominal operating conditions for the laboratory prototype

Usually this diagram is proposed at different irradiation levels, because it is well known that the differential resistance of the PV array, whose value depends on its operating conditions, has a significant impact on the Bode plot. On the contrary, the proposed control approach allows to make the system dynamics not depending on the PV array differential resistance so that, in accordance with (2.27), its performances do not change with the

operating conditions and do not depend on the PV array type, size and characteristics. This consideration is supported by the results shown in Fig. 2.11. The Bode plots obtained by means of PSIM simulations at very different irradiance conditions have been compared with those ones obtained by means of the analytical model: Fig. 2.11 allows to confirm that the voltage loop is almost the same irrespectively from the variation of the PV operating conditions. Fig.2.12 shows the step response of the PV voltage and inductor current in presence of a step in the reference voltage. The system goes to regime in a time interval whose duration is almost 3-5 times the time constant, as predicted by the Bode diagram.

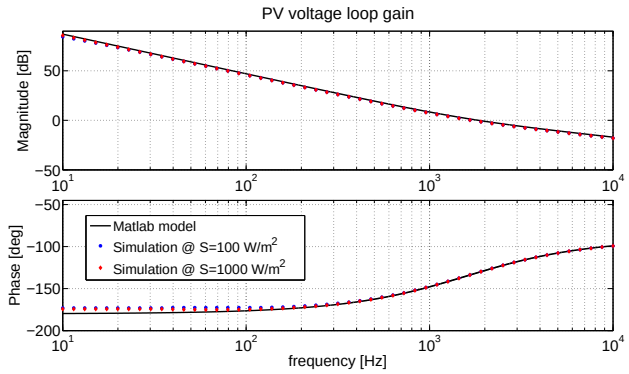

Figure 2.11: Bode diagram of the voltage loop gain. Continuous line: analytical model. Red dots: result of the PSIM simulation at a high irradiance level. Blue points: result of the PSIM simulation at a low irradiance level.

In order to verify the voltage loop stability and the MPPT tracking capability of the sliding mode controlled boost converter, the system has been also tested in presence of a fast irradiance variation. This condition has been emulated by using two identical PV modules connected in parallel at the input of the converter and disconnecting one of them abruptly, thus reproducing a 50%

sudden irradiance variation.

It is worth noting that this test has been performed by also applying the 6V peak-to-peak 100Hz sinusoidal voltage disturbance at the output of the converter, in order to test the MPPT capabilities of the proposed technique in the worst conditions. The P&O MPPT algorithm have been tuned according to the recipes given in [FPSV05], thus resulting in a sampling time $T_a = 60ms$ and a voltage reference step amplitude $\Delta V_{ref} = 0.4V$.

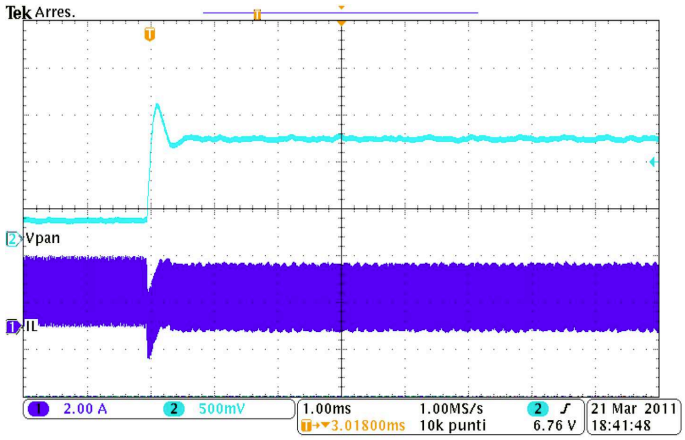

Figure 2.12: Step response with respect to the reference voltage variation. CH2: PV voltage, CH1: inductor current

The blue waveform in Fig. 2.13, representing the PV current, confirms that the sliding-mode control works once again effectively and that the system quickly reaches the new steady state conditions. As revealed by the PV voltage behavior, that is the light blue waveform, before and just after the perturbation the operating point moves around the MPP, in both cases by keeping the three levels stair-wise behavior. This measure confirms the stability and robustness of the control technique proposed.

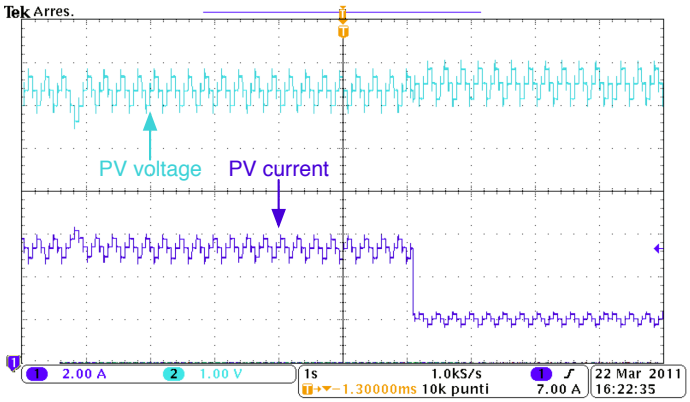

Figure 2.13: MPPT in presence of a fast irradiance variation

Chapter 3

Design of a Sliding Mode Controlled SEPIC for PV MPPT Applications

The design and implementation of the control algorithm proposed in the previous chapter refer to a boost dc/dc converter, but many PV applications require different topologies. Indeed, step up/down topologies are much more suitable in distributed MPPT (DMPPT) architectures, to the aim of compensating the mismatching effects [FLP+08] [ARS+12], and in stand-alone applications, in order to match different batteries with a wide range of PV modules. In [LEMB09] a non-inverting dc/dc converter which can operate in buck, boost or pass-through modes has been shown. Although this solution maximizes the conversion efficiency by reducing the components' stresses and the energy storage requirements, it has a drawback in terms of transition from the boost mode to the buck mode and vice versa. In [RCCP+11] this control aspect has been improved, but at the price of the need of a coupled inductor that affects the control design and robustness.

In the following the control approach proposed is extended to a wide class of step up/down dc/dc converter topologies, in particular to those ones having an input C-L second order filter, this being a prerequisite for the application of the proposed SM-based MPPT

technique. The simple approach is now completed by the formal analysis and the resulting design equations will be proposed. The design methodology presented in the following sections is applied to a Single Ended Primary Inductor Converter (SEPIC), but its extension to other fourth order converters, e.g. the Cúk one, is almost immediate. It is worth noting that in literature some examples of control design for fourth order dc/dc converters are presented, but they only refer to a linear regulation, while few papers are devoted to the the design of the SM control for such topologies [MST95], although not referred to PV applications.

In addition the analysis of the SM control reachability and existence conditions is carried out by using a graphical approach that has been never applied before to fourth order switching converters. It reveals very useful for identifying the key relations among the parameters of both the PV array and the converter as well as the sliding surface. The analysis is validated through simulations and experimental results.

3.1 Sliding Mode based MPPT control

The referring SM control architecture is shown in Fig.3.1. As usual, the PV source is modeled by using a Norton equivalent circuit, where the parameter R_{diff} is the differential resistance of the source in its operating point and the current i_{pv} depends on the irradiance level and on the PV output voltage.

The SM control is aimed at imposing a constraint to the state variables through the definition of a sliding surface [UGS09]:

$$S = \sum_{i=1}^{N} k_i \cdot x_i$$

which must be chosen so that:

- the trajectories that characterize the substructures in the vicinity of the chosen sliding surface are directed towards the surface itself.

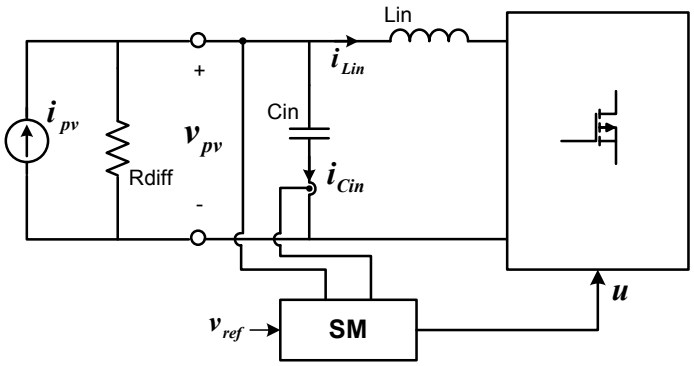

Figure 3.1: Connection scheme of the PV linear model with SM controller

- all trajectories must reach the sliding surface regardless of the initial state of the system. In this case, in fact, the state of the system can be maintained arbitrarily close to the sliding surface, regardless of the values assumed by the system's parameters, by means of an adequate control of the switch of the converter.

The SM control based MPPT proposed in [BCG+13] used the following sliding surface:

$$S = k_1 \cdot x_1 + k_2 \cdot x_2 \tag{3.1}$$

where x_1, x_2 are related to the parameters shown in Fig.3.1 as follows:

$$\begin{cases} x_1 & = -i_{Cin} = i_{Lin} + \frac{v_{pv}}{R_{diff}} - i_{pv} \\ x_2 & = v_{pv} - v_{ref} \end{cases} \tag{3.2}$$

where v_{ref} is the reference voltage of the SM controller as in Fig.3.1. Although the order of the converter is higher, only two sliding coefficients have been considered different from zero, thus:

$$\mathbf{K^T} = [k_1, k_2, 0, 0] \tag{3.3}$$

where the SM gains k_1, k_2 also accounts for the gains of the voltage and current sensors. Formally, the sliding surface (3.1) is expressed as:

$$S = \mathbf{K^T} \cdot \mathbf{x} \tag{3.4}$$

3.1.1 Reachability and existence conditions

The SM control design procedure consists of two steps. In the *hitting* phase, the controller drives the trajectory of the state variables towards the sliding surface, regardless of the initial position. The *reachability* condition must be ensured. For the PV system under study, the SM surface (3.1) divides the phase plane into two half-planes characterized by $S = k_1 \cdot x_1 + k_2 \cdot x_2 > 0$ and $S = k_1 \cdot x_1 + k_2 \cdot x_2 < 0$. By assuming that the switching converter shown in Fig.3.1 works in continuous conduction mode or it is a synchronous one, two substructures must be considered: the SM control drives the converter by means of the signal $u \in \{0, 1\}$, thus activating the first or the second substructure. Each substructure is evidently stable and its operating point converges towards a unique equilibrium point. In [UGS09] it is demonstrated that the condition of reachability holds if, in each half-plane, the control signal u activates the substructure having its equilibrium point located in the opposite half-plane [MSGO$^+$12].

The SM control *existence condition* implies that all the trajectories in the vicinity of the sliding surface are attracted by it; the necessary and sufficient conditions are [MRST93]:

$$\lim_{S \to -\frac{H}{2}^+} \frac{\partial S}{\partial t} < 0 \quad \text{and} \quad \lim_{S \to \frac{H}{2}^-} \frac{\partial S}{\partial t} > 0 \tag{3.5}$$

The constraints (3.5) ensuring that the SM regime exists are greatly depending on the systems under study and on the design conditions.

By using the matrix formalism, the SM existence conditions are [MRST93]:

$$\frac{\partial S}{\partial t} = \frac{\partial(\mathbf{K^T} \cdot \mathbf{x})}{\partial t} = \mathbf{K^T} \cdot \dot{\mathbf{x}} = \\ = \mathbf{K^T} \cdot (\mathbf{A}\ \mathbf{x} + \mathbf{B}) + \mathbf{K^T} \cdot (\mathbf{C}\ \mathbf{x} + \mathbf{D})\, u \tag{3.6}$$

where the bilinear notation [SR87] has been used for describing the generic converter dynamic:

$$\dot{\mathbf{x}} = \mathbf{A}\ \mathbf{x} + \mathbf{B} + (\mathbf{C}\ \mathbf{x} + \mathbf{D}) \cdot u \tag{3.7}$$

where **A, B, C, D** are calculated by means of the procedure shown in [SR87], thus considering the two piecewise linear differential equations of the substructures characterizing the switching converter.

3.1.2 SM dynamical analysis: the equivalent control

An ideal SM control operation would require an infinite switching frequency, so that the trajectories of the state variables are oriented precisely to the sliding surface. With a finite switching frequency the trajectory oscillates across the sliding surface by moving towards the steady state point that is, because of the definition of the state variables given in (3.2), the origin of the cartesian plane (x_1, x_2).

The trajectory is a composition of two dynamic components [UGS09]: the high frequency one, related to the switching operation, is assumed to have been filtered out. The low frequency component gives the ideal trajectory moving along the sliding surface: thus it is $S = 0$ and also the time derivative of the sliding surface must be equal to zero, so that:

$$\textit{invariant condition:} \quad S = 0 \tag{3.8}$$

$$\textit{equivalent control condition:} \quad \frac{\partial S}{\partial t} = 0 \tag{3.9}$$

From (3.6) it results that:

$$\mathbf{K^T}\left(\mathbf{A}\mathbf{x} + \mathbf{B}\right) + \mathbf{K^T} \cdot \left(\mathbf{C}\ \mathbf{x} + \mathbf{D}\right) \cdot u_{eq} = 0$$

and u_{eq} is the low frequency component of u:

$$u_{eq} = -\mathbf{K^T} \cdot \left(\mathbf{A}\ \mathbf{x} + \mathbf{B}\right) \cdot \left(\mathbf{K^T} \cdot \left(\mathbf{C}\ \mathbf{x} + \mathbf{D}\right)\right)^{-1} \tag{3.10}$$

with $\mathbf{K^T} \cdot \left(\mathbf{C}\ \mathbf{x} + \mathbf{D}\right) \neq 0$ that is the so called *trasversal condition* [SR87] [MST95].

The equivalent control u_{eq} can be substituted in (3.7) by reducing the order of the system, so that a non-linear equivalent system results. By imposing $\dot{\mathbf{x}} = 0$ and by fixing the sources vectors $\mathbf{B}$ and $\mathbf{D}$ in (3.7), the model can be linearized around an equilibrium point, so that the stability analysis and the dynamic behavior can be studied locally by means of traditional tools [MST95]. This approach is used in Section V for putting into evidence some peculiarities of the proposed SM control applied to the SEPIC converter.

3.2 SM control of a PV SEPIC converter: the reachability conditions

A comparison of different step up/down topologies reveals that the SEPIC has limitations in terms of efficiency and cost, but it offers a non inverting polarity and the low input current ripple allows a high MPPT efficiency, so that it is suitable for PV applications [CSC09]. The SM control based CMPPT technique described in [BCG$^+$13] is applied to the synchronous SEPIC topology shown in Fig.3.2, with the parameters values listed in Tab.3.2.

The converter's output terminals are assumed to be connected to a constant voltage source, as it is the case of battery chargers or connection to a dc bus whose voltage level is controlled by another converter [FPSV12].

The system modeling requires the calculation of the differential equations that describe the trajectories of the substructures obtained by considering the two possible operation modes ($u = 1$ and $u = 0$), accounting for the ON and OFF states of the controlled switches, as in Fig.3.3.

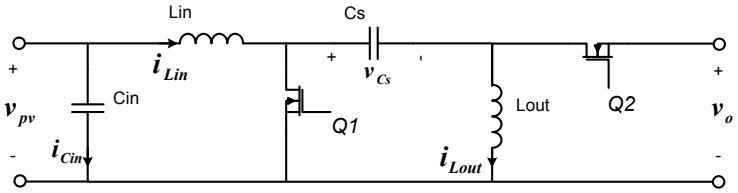

Figure 3.2: Sepic converter

parameter	value	parameter	value
L_{in}	$15\mu H$	L_{out}	$15\mu H$
C_{in}	$22\mu F$	C_s	$44\mu F$
V_o	12V	V_{ref}	6V
I_{pv}	3A	R_{diff}	5Ω

Table 3.1: Parameters' values

The analysis is carried out by assuming that:

$$\begin{cases} x_1 = i_{Lin} - i_{pv} + \frac{v_{pv}}{R_{diff}} = -i_{Cin} \\ x_2 = v_{pv} - v_{ref} \\ x_3 = i_{Lout} \\ x_4 = v_{Cs} \end{cases} \tag{3.11}$$

Regardless of the fourth order of the system, according to (3.1) the trajectories of the variables x_1 and x_2 allow to evaluate the SM

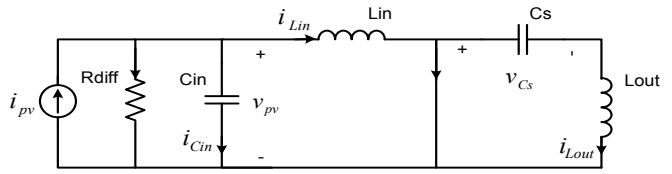

(a) Substrucure I

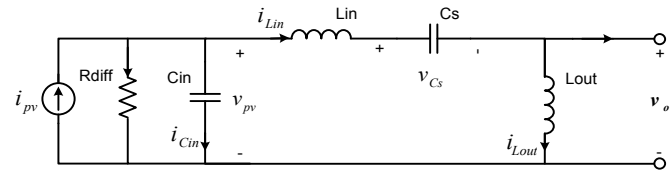

(b) Substrucure II

Figure 3.3: Linear substructures derived by the PV SEPIC converter operations

reachability condition.

3.2.1 First substructure

The differential equations for the first substructure (see Fig.3.3(a)) are:

$$\begin{cases} \dot{x}_1 = -\frac{1}{R_{diff}C_{in}}x_1 + \frac{x_2}{L_{in}} + \frac{v_{ref}}{L_{in}} - \dot{i}_{pv} \\ \dot{x}_2 = -\frac{x_1}{C_{in}} - \dot{v}_{ref} \\ \dot{x}_3 = -\frac{x_4}{L_{out}} \\ \dot{x}_4 = \frac{x_3}{C_S} \end{cases} \tag{3.12}$$

By assuming that the PV system works in steady state conditions in terms of i_{pv} and v_{ref}, from (3.12) it results that:

$$\ddot{x}_2 + \dot{x}_2\frac{1}{R_{diff}C_{in}} + x_2\frac{1}{C_{in}L_{in}} = -\frac{V_{ref}}{C_{in}L_{in}} \tag{3.13}$$

The discriminant of the algebraic homogeneous equation is:

$$\Delta = \left(\frac{1}{R_{diff}C_{in}}\right)^2 - \frac{4}{L_{in}C_{in}} \tag{3.14}$$

Typical values of the input inductance and capacitance used in PV applications give $\sqrt{\frac{C_{in}}{L_{in}}} < 1$, because a large capacitance value helps in reducing the PV voltage ripple and a low inductance value allows reducing its ESR thus the conduction losses. On the other side, if the PV generator works in its maximum power point, $R_{diff} = \frac{V_{MPP}}{I_{MPP}}$ [FPSV12]. By referring to many of the PV modules actually on the market, it is greater than one and, for PV string applications, it becomes even larger than ten. As a consequence, the discriminant assumes negative values thus producing complex eigenvalues:

$$\Delta < 0 \quad \rightarrow \quad \frac{1}{2R_{diff}} < \sqrt{\frac{C_{in}}{L_{in}}} \tag{3.15}$$

Thus, the state variables show damped oscillating waveforms, the values of the two integration constants being calculated by fixing the initial conditions for $x_1(t)$ and $x_2(t)$, giving rise to a specific trajectory in the phase plane. According to (3.2), all the trajectories of the state variables converge towards the following steady state values:

$$\begin{cases} x_1(\infty) = 0 \\ x_2(\infty) = -V_{ref} \end{cases} \tag{3.16}$$

Fig.3.4(a) shows a typical trajectory of the state variables for the first substructure.

3.2.2 Second substructure

The differential equations for the second substructure (see Fig.3.3(b)) are:

$$\begin{cases} \dot{x}_1 = -\frac{1}{R_{diff}C_{in}}x_1 + \frac{x_2}{L_{in}} - \frac{x_4}{L_{in}} - \dot{i}_{pv} + \frac{v_{ref}}{L_{in}} - \frac{v_o}{L_{in}} \\ \dot{x}_2 = -\frac{x_1}{C_{in}} - \dot{v}_{ref} \\ \dot{x}_3 = \frac{v_o}{L_{out}} \\ \dot{x}_4 = \frac{x_1}{C_S} - \frac{x_2}{C_S R_{diff}} - \frac{v_{ref}}{C_S R_{diff}} + \frac{i_{pv}}{C_S} \end{cases} \tag{3.17}$$

The coupling capacitor (see Fig.3.3(b)) introduces an additional dynamic content in the second substructure, this resulting in the following third-order differential equation:

$$\dddot{x}_2 + b \cdot \ddot{x}_2 + c \cdot \dot{x}_2 + d \cdot x_2 = \frac{I_{pv}}{C_{in}L_{in}C_s} - \frac{V_{ref}}{R_{diff}C_{in}L_{in}C_s} \tag{3.18}$$

where:

$$\frac{1}{R_{diff}C_{in}} = b \qquad \frac{C_{in}+C_s}{C_{in}C_sL_{in}} = c$$

$$\frac{1}{R_{diff}C_{in}L_{in}C_s} = d$$

As in the case of (3.13), the values of v_{ref} and i_{pv} have been considered constant. The homogeneous algebraic equation associated to this differential equation is:

$$\lambda^3 + b\lambda^2 + c\lambda + d = 0 \tag{3.19}$$

whose solutions are obtained by using the variable change $\lambda = \beta - \frac{b}{3}$ [Web]:

$$\beta^3 + \beta p + q = 0 \tag{3.20}$$

where $p = -\frac{b^2}{3} + c$ and $q = \frac{2b^3}{27} - \frac{bc}{3} + d$.

Solutions of (3.20), and thus of (3.19), are functions of the following two real numbers u, v [Web]:

$$u = \sqrt[3]{-\frac{q}{2} + \sqrt{\Delta}}, \quad v = \sqrt[3]{-\frac{q}{2} - \sqrt{\Delta}} \tag{3.21}$$

where the discriminant is:

$$\Delta = \frac{q^2}{4} + \frac{p^3}{27} \tag{3.22}$$

The strictly positive value of the determinant ensures that the solutions of (3.19) are one real eigenvalue and two complex conjugate ones.

Inequality (3.22) suggests that a sufficient condition for having $\Delta > 0$ is $p \geqslant 0$, the value q^2 always being positive.

Thus, by referring to the PV system parameters, $p \geqslant 0$ means:

$$\frac{1}{\sqrt{3}R_{diff}} \leq \sqrt{\frac{C_{in}(C_{in} + C_s)}{C_s L_{in}}} \tag{3.23}$$

For the same reasons used for justifying the design condition (3.15), condition (3.23) ensures that the state variables have a damped behavior, so that they evolve in the phase plane as convergent spirals having the following regime values:

$$\begin{cases} x_1(\infty) & = 0 \\ x_2(\infty) & = R_{diff} I_{pv} - V_{ref} \end{cases} \tag{3.24}$$

The values of the three integration constants depend on the initial conditions, so that the additional equation for x_4 is needed:

$$x_4(t) = x_2(t) + Vref - L_{in}\dot{x}_1 - \frac{L_{in}}{R_{diff}C_{in}} x_1(t) - V_o \tag{3.25}$$

Each trajectory can be plotted by starting from the initial values imposed to $x_1(t)$, $x_2(t)$ and $x_4(t)$. An example of such trajectory is shown in Fig.3.4(b).

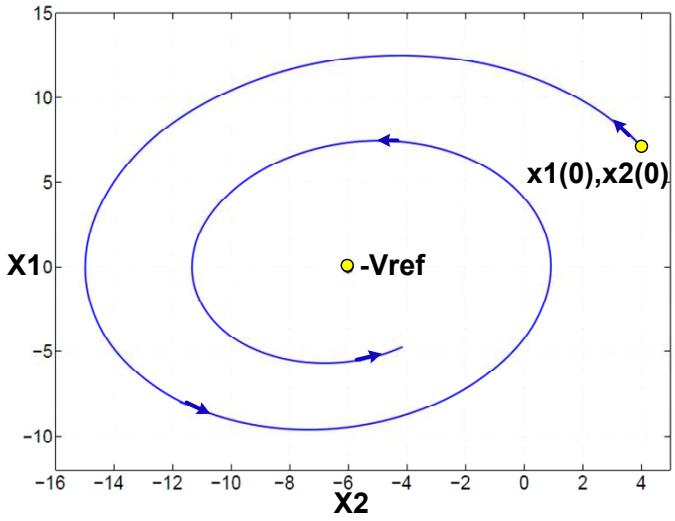

(a) Substrucure I

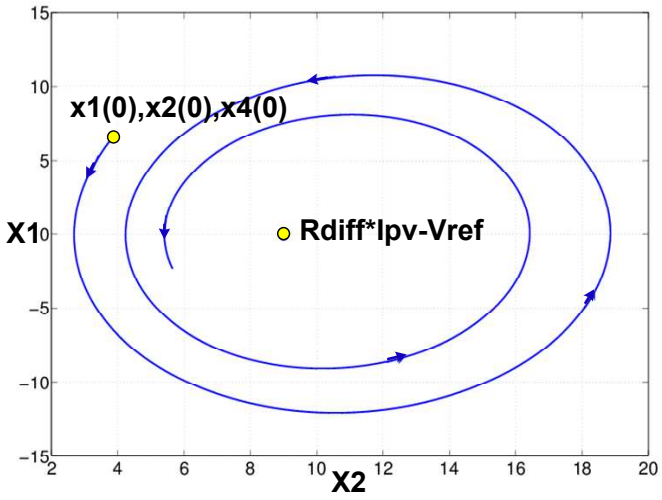

(b) Substrucure II

Figure 3.4: Phase plane analysis of the two substructures of the PV SEPIC converter

It is worth noting that the role of power source of the PV generator translates into positive values of both v_{pv} and i_{pv}. Moreover, V_{ref} is the regime value of v_{pv}, thus it is positive. Finally, in order to have a positive power generated by the PV unit, the following condition holds:

$$R_{diff} I_{pv} > V_{ref} \tag{3.26}$$

By looking at the equilibrium points of the two substructures, (3.16) and (3.24), this means that the steady state values of the two substructures shown in Fig.3.4 are located in the negative and positive half-planes, respectively.

The condition (3.8) allows to draw the sliding surface (3.1) in the phase plane (x_2, x_1):

$$S(\mathbf{x}) \leftarrow k_1 x_1 + k_2 x_2 = 0$$

whose slope is equal to:

$$m_S = -\frac{k_2}{k_1} \tag{3.27}$$

In the following, the case $m_S > 0$ with $k_1 > 0$ and $k_2 < 0$, shown in Fig.3.5 is considered, but similar conclusions can be obtained for the other cases.

The gray area in Fig.3.5 identifies the half-plane where $k_1 \cdot x_1 + k_2 \cdot x_2 > 0$. In this half-plane, the MOSFET must be forced to be off (u=0) in order to apply the conditions recalled in section 3.1.1, so that the second substructure holds. This substructure tends to the steady state condition (3.24), placed in the white half-plane, with the behavior shown in Fig.3.4(b). Similarly, in the white half-plane the MOSFET must be forced to be on (u=1) and the first substructure holds. This substructure tends to the steady state condition (3.16) placed in the grey half-plane with the behavior shown in Fig.3.4(a).

These choices assure that the *reachability condition* holds for the PV SEPIC converter under study. Fig.3.5 also shows the

hysteresis bandwidth H allowing to obtain a finite switching frequency, so that the SM control is implemented through the following conditions:

$$\begin{cases} \textbf{if} \;\; k_1 \cdot x_1 + k_2 \cdot x_2 < \frac{H}{2} \rightarrow \;\; u = 1; \\ \textbf{if} \;\; k_1 \cdot x_1 + k_2 \cdot x_2 > -\frac{H}{2} \rightarrow \;\; u = 0; \end{cases} \tag{3.28}$$

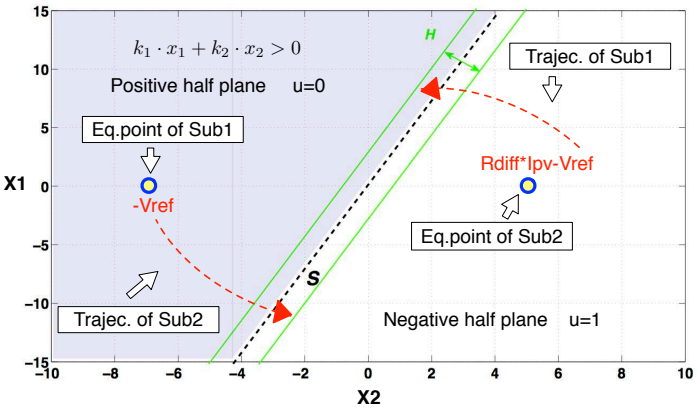

Figure 3.5: Reachability conditions

3.3 SM control of a PV SEPIC converter: the existence condition and the Region of Existence (RoE)

The SM *existence condition* is given by applying (3.5). The matrices appearing in (3.6) are calculated by applying the classical procedure shown in [SM01]. Thus, the equations of the two lines $\gamma_1(\mathbf{x})$ and $\gamma_1(\mathbf{x})$ are obtained and the following inequalities result:

$$\begin{cases} \gamma_1(\mathbf{x}) \leftarrow & (\frac{1}{R_{diff}C_{in}} + \frac{k_2}{k_1}\frac{1}{C_{in}})\ x_1 - \frac{1}{L_{in}}x_2 - \frac{V_{ref}}{L_{in}} > 0 \\ \gamma_2(\mathbf{x}) \leftarrow & (\frac{1}{R_{diff}C_{in}} + \frac{k_2}{k_1}\frac{1}{C_{in}})\ x_1 + \\ & -\frac{1}{L_{in}}x_2 - \frac{V_{ref}}{L_{in}} + \frac{x_4}{L_{in}} + \frac{V_o}{L_{in}} < 0 \end{cases} \tag{3.29}$$

Conditions (3.29) define the RoE in the tridimensional space x_1, x_2, x_4. In order to simplify the graphical representation and by keeping into account that x_4 is not used to define the sliding surface (3.1), the variable x_4 is considered as a parameter defined as V_{cs} (3.11). It is well known that, in steady state conditions, for the SEPIC topology it is $V_{cs} = V_{pv}$. If the SM controller operates properly, it also ensures that $V_{cs} = V_{ref}$. As a consequence of this parametrization, in the phase plane (x_2, x_1) the equations γ_1 e γ_2 (3.29) are represented by two straight lines that bound the RoE. The slopes of both the lines are:

$$m_\gamma = \frac{C_{in}}{L_{in}(\frac{1}{R_{diff}} + \frac{k_2}{k_1})} \tag{3.30}$$

By using (3.27) with the assumption $m_S > 0$ and by keeping into account inequalities (3.29), it results that, in order to have that the equilibrium point $(x_1 = 0, x_2 = 0)$ is included into the RoE, the slopes m_S and m_γ must have an opposite sign. Thus, the slopes of the lines γ_1 and γ_2 must be negative [SM01].

Finally the *existence conditions* give an additional constraint for selecting the SM coefficients:

$$-\frac{k_2}{k_1} > \frac{1}{R_{diff}} \tag{3.31}$$

3.3.1 The 2-dimensional RoE

By looking at Fig.3.6, it is evident that the two straight lines γ_1 e γ_2 (3.29) intersect the two axes of the cartesian plane in the following four points:

$$
\begin{aligned}
P_1 &= [-V_{ref}, 0] \\
P_2 &= [0, m_\gamma \cdot V_{ref}] \\
P_3 &= [-V_{ref} + V_{cs} + V_o, 0] \\
P_4 &= [0, m_\gamma \cdot (V_{ref} - V_{cs} - V_o)]
\end{aligned} \tag{3.32}
$$

Because of the assumptions $V_{ref} > 0$, $m_\gamma < 0$ and $V_{cs} = V_{ref}$ in steady state conditions, it results that the points P_1, P_2, P_3 and P_4 are located as shown in Fig.3.6. Finally, in the phase plane

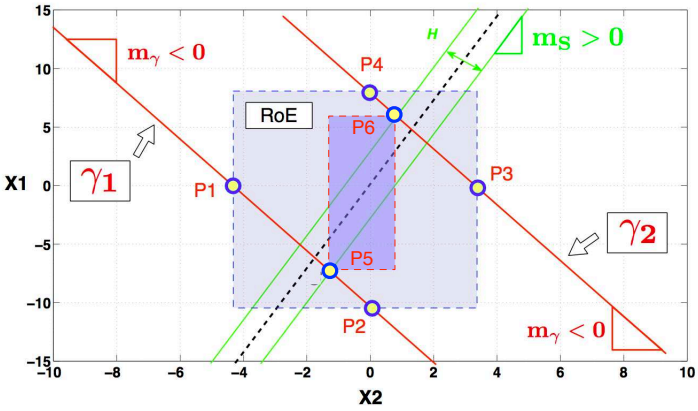

Figure 3.6: Rectangular approximations of the RoE

these points define a rectangle approximating the RoE. Such a region is the one shown in grey color in Fig.3.6, whose size depends on the SM coefficients and on the system parameters (see (3.30) and (3.32)). Thanks to the choice of the sliding surface (3.1), which can be graphically represented in the plane (x_1, x_2), and to the parametrization of the other state variables, e.g. x_4 in the case under study, the graphical analysis presented in the current literature, e.g. [SM01], can be used for analyzing the high order PV SEPIC system.

In the next Section a more accurate reconstruction of the RoE is performed, this being useful for achieving further equations for

the SM control design.

3.3.2 Accurate 2-dimensional RoE analysis

The reliable and accurate reconstruction of the RoE at different operating conditions and for different values of the parameters is a key tool for the optimal system design also in terms of MPPT performances. By intersecting the straight lines obtained by the

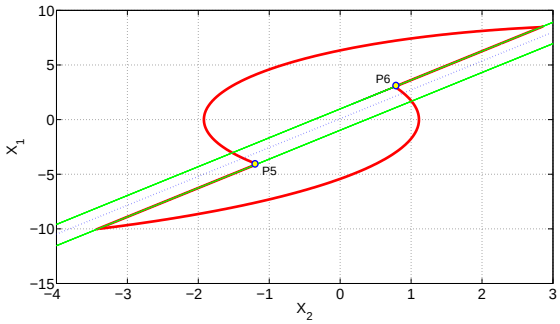

Figure 3.7: Exact RoE at a fixed x_4 value

existence conditions (3.29) with the straight lines resulting from the hysteresis band (3.28) the two additional points P_5 and P_6 shown in Fig.3.6 and expressed as in (3.33) and (3.34) are obtained. P_5, P_6 identify the vertices of a rectangle, marked in blue in Fig.3.6: expressions (3.33) and (3.34) clearly show the dependency of this RoE approximation on the SM parameters, on the converters' parameters and, moreover, on the PV array operating conditions through R_{diff}. It is also worth noting the dependency of this new RoE approximation from the hysteresis band H, which is missed in the approximation given in Section 3.3.1 through P_1, P_2, P_3 and P_4. Although a rectangular approximation of the RoE could be very useful for design purposes, it might be too rough with respect to the real shape of the RoE. Thus, accounting for the dynamic behavior of the two substructures shown in Fig.3.4 and by using P_5 and P_6 as the points where such dynamics hit the

hysteresis band within the RoE, a more accurate result is obtained. Therefore, P_5 and P_6 are the hitting points of the two trajectories having the maximum distance from the stationary operating point and holding to the RoE.

$$P_5 = (x_2, x_1) = \left(\frac{R_{diff}{k_1}^2 V_{ref} C_{in} - H k_1 L_{in} - H k_2 L_{in} R_{diff}}{k_2 k_1 L_{in} + {k_2}^2 L_{in} R_{diff} + {k_1}^2 R_{diff} C_{in}}, \frac{k_1 (k_2 V_{ref} + H) R_{diff} C_{in}}{k_2 k_1 L_{in} + {k_2}^2 R_{diff} L_{in} + {k_1}^2 R_{diff} C_{in}}\right) \tag{3.33}$$

$$P_6 = (x_2, x_1) = \left(-\frac{{k_1}^2 (V_{ref} - V_{cs} - V_o) R_{diff} C_{in} + H k_1 L_{in} + H k_2 L_{in} R_{diff}}{k_2 k_1 L_{in} + {k_2}^2 L_{in} R_{diff} + {k_1}^2 R_{diff} C_{in}}, \frac{k_1 (k_2 V_{ref} - H - k_2 V_{cs} - k_2 V_o) R_{diff} C_{in}}{k_2 k_1 L_{in} + {k_2}^2 L_{in} R_{diff} + {k_1}^2 R_{diff} C_{in}}\right) \tag{3.34}$$

In Fig.3.7, the red contour shows the real shape of the RoE obtained at a fixed value of $x_4 = V_{cs} = V_{ref}$: it is evident that the real RoE looks completely different from the rectangular approximations shown in Fig.3.6.

RoE parametric variation: effect of the SM gains

Fig.3.8 shows the way in which the SM gains k_1 and k_2 values affect the shape of the RoE. The larger the m_S value, the higher the RoE inclination and the smaller its area. As it will be shown in Section 3.4, this results in a faster system dynamic response.

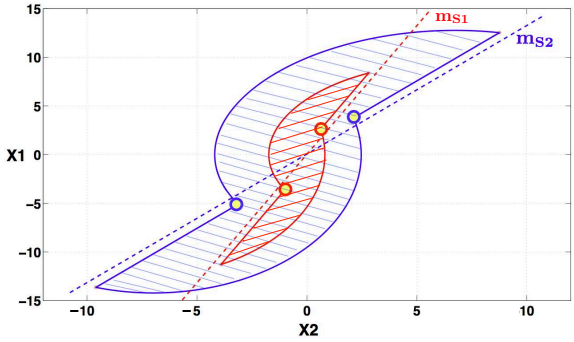

Figure 3.8: Effect of k_1 and k_2 on the RoE

RoE parametric variation: effect of irradiation, output voltage and reference signal value

Figs. 3.9(a)-3.9(c) show the effects on the RoE of variations on the irradiance level, affecting I_{pv} and R_{diff}, on V_{out} and on V_{ref}. The other parameters have been fixed at those values listed in Tab.3.2. The RoE inclination is not affected by these variations.

RoE parametric variation: effect of capacitances values

Fig.3.10 shows the effects on the section of the RoE by keeping constant the working condition and changing some parameters of the switching converter. The input capacitance has a greater effect on the RoE size.

3.3.3 From a 2-dimensional to a 3-dimensional RoE: parametric variation of x_4

The complete tridimensional characterization of the RoE results by collecting the surfaces obtained in the phase plane (x_1, x_2) for a number of different values for $x_4 = V_{Cs}$. Fig.3.11 shows that the RoE tapers for low values of x_4, therefore in that part of the volume the SM can be lost much more easily. At this point, the RoE has been constructed as a function of all the system parameters. Now

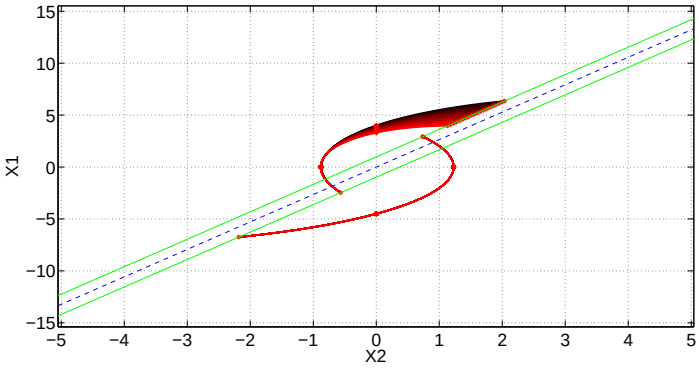

(a)

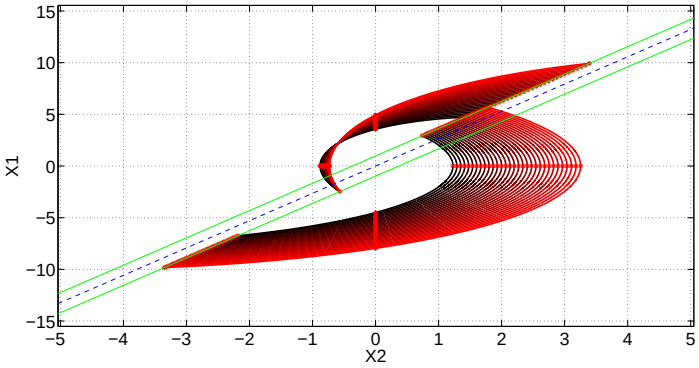

(b)

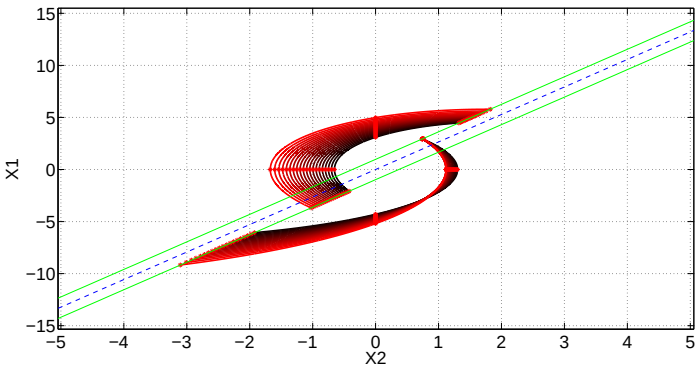

(c)

Figure 3.9: RoE parametric analysis: a) Irradiance level from 200 W/m^2(black line) to 1000 W/m^2 (red line); b) V_{out} from 4V (black line) to 8V (red line) @ V_{ref}=5V; c) V_{ref} from 4V (black line) to 8V (red line) @ V_{out}=5V.

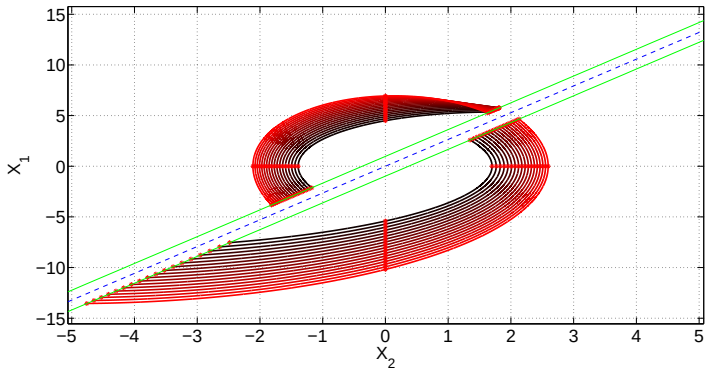

(a)

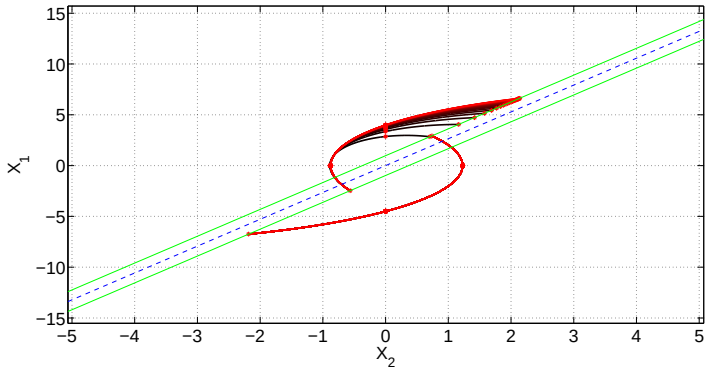

(b)

Figure 3.10: RoE parametric analysis with respect to C_{in} and C_s: a) C_{in} from 22uF (black line) to 48uF (red line); b) C_s from 22uF (black line) to 280uF (red line)

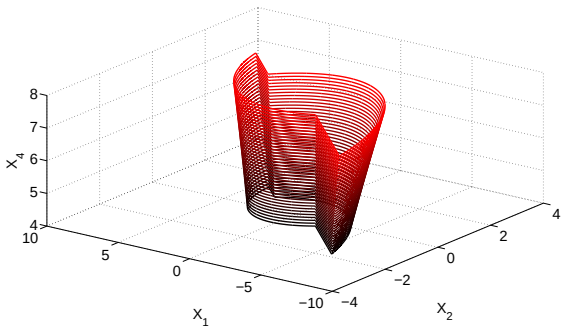

Figure 3.11: 3D RoE obtained by considering a variation of 2V with respect to a central value for V_{Cs}, this means $x_4 = v_{Cs} = 6 \pm 2\text{V}$

the system dynamics need to be studied by means of a suitable model.

3.4 Stability analysis of the system in SM

The technique introduced in Section 3.1.2 is useful in order to have the dynamic behavior of the system and to analyze its stability in SM operation. From (3.10) it results that:

$$\overline{u}_{eq} = \frac{x_2 + v_{ref} - \frac{L_{in}}{C_{in}}\left(\frac{1}{R_{diff}} + \frac{k_2}{k_1}\right)x_1 - L_{in}(\dot{i}_{pv} - \frac{k_2}{k_1}\dot{v}_{ref})}{x_4 + v_o} \quad (3.35)$$

As reported in literature [UGS09], by putting (3.35) in (3.7) a non linear model is obtained. The latter has an order that is reduced by one with respect to the initial model. Therefore, only three of the four state variables are still independent: they are x_2, x_3, x_4.

The non linear model is studied by means of a linearization

around the following steady state operating point [MST95], with $\dot{x}_2 = \dot{x}_3 = \dot{x}_4 = \dot{v}_{ref} = \dot{i}_{pv} = 0$ and $v_{ref} = V_{ref}, i_{pv} = I_{pv}$, that is:

$$\begin{cases} X_2 = 0 \\ X_3 = -\frac{V_{ref} \cdot (R_{diff} I_{PV} - V_{ref})}{R_{diff} V_o} \\ X_4 = V_{ref} \end{cases} \tag{3.36}$$

The state space model has been linearized around the equilibrium point (3.36); it has the following eigenvalues:

$$\lambda_1 = \frac{k_2}{C_{in} k_1} \quad \text{and} \quad \lambda_{2,3} = \frac{\alpha \pm \sqrt{\theta}}{\beta} \tag{3.37}$$

where:

$$\alpha = V_{ref} L_{out} \cdot (V_{ref} - R_{diff} I_{pv})$$

$$\theta = L_{out}^2 V_{ref}^2 \cdot (R_{diff} I_{pv} - V_{ref})^2 + - 4 V_o^2 R_{diff} L_{out} C_s \cdot (V_o V_{ref} + V_o^2)$$

$$\beta = 2 C_s R_{diff} L_{out} V_o \cdot (V_{ref} + V_o)$$

The eigenvalues $\lambda_{2,3}$ affect the dynamic behavior of x_3 and x_4: they explicitly depend on the switching converter and on the source and load parameters R_{diff}, I_{pv} and V_o. As a consequence, the stability of the two modes depends on the system operating point. If the condition (3.26) is fulfilled, the real part of $\lambda_{2,3}$ is less than zero for any possible value of the other PV parameters.

The first eigenvalue λ_1 represents the dynamic behavior of $x_2 = v_{pv} - V_{ref}$. It only depends on the SM gains k_1 and k_2 and on the input capacitance value. This is one of the main results obtained in this analysis, because it means that the dynamic behavior of the PV voltage does not depend on the differential resistance of the PV source and on all the parameters of the dc/dc converter, but

it is affected by the SM gains and by C_{in} only. This means that the MPPT operation can be made faster and faster by working on k_1, k_2 and C_{in} only, without taking into account the PV array operating point and L_{in}, both having a strong influence in the classical P&O approach [FPSV12]. It is worth noting that the values of k_1, k_2 and C_{in} must be designed in order to obtain the best trade off between the system promptness and the width of the RoE.

In the sequel some results obtained through simulations are proposed. They show the dynamic behavior of the system when it is subjected to variations of the reference voltage and of the irradiation level, in relation with the RoE evaluated in Section 3.3.2.

3.4.1 Dynamic behavior after a variation of the V_{ref} value

This analysis is important because the step variations of the reference voltage are triggered by the MPPT P&O based controller [BCG+13]. The circuit shown in Fig.3.2 is simulated by applying a 1V step variation of the reference voltage V_{ref}. As summarized in Tab.3.2, this variation has an effect also on the PV source parameters, which have been determined as in [FPSV12].

Parameter	Values and variations
G	$800W/m^2$
I_{pv}	$6.11A \rightarrow 6.09A$
R_{diff}	$104\Omega \rightarrow 32\Omega$
V_{ref}	$6V \rightarrow 7V$
k_2	-0.436
k_1	0.165

Table 3.2: Parameters values used in the example of Section 3.4.1

As shown in Fig. 3.12, the operating point moves inside the RoE. Fig. 3.12.a) reveals that the range of x_4 used for estimating

the RoE is large enough for including the whole oscillation of x_4.

Just after the perturbation, the working point hits the sliding surface and the system dynamics remains confined in the hysteresis band, being attracted towards the equilibrium point, i.e. the origin.

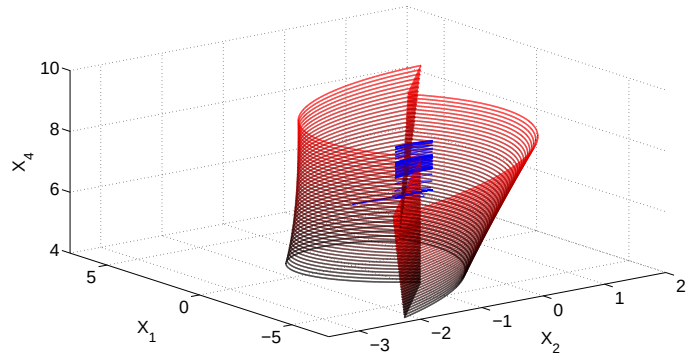

(a) RoE 3D

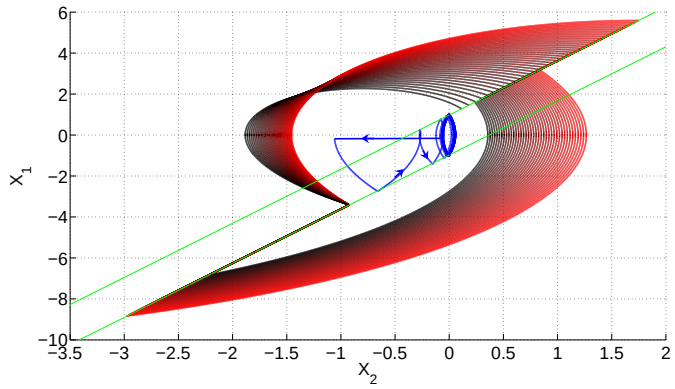

(b) RoE 2D

Figure 3.12: RoE and path of the operating point for the case described in Section 3.4.1

By taking from Tab.3.2 and Tab.3.2 the values of k_1, k_2 and C_{in}, it results that the time constant of the system, equal to $\frac{1}{\lambda_1} \approx$

8.3μs, gives a settling time of about 33μs, which is confirmed by the time domain simulation result reported in Fig. 3.13.

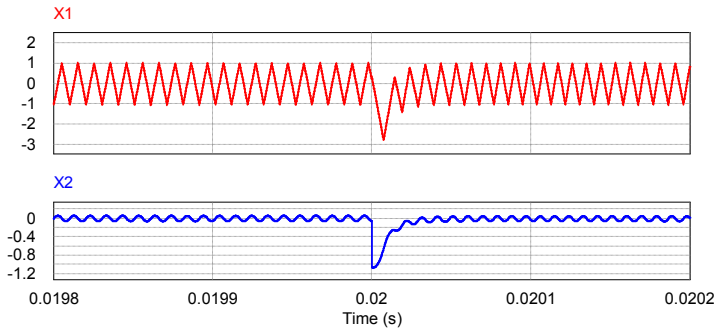

Figure 3.13: Waveforms of x_1 (red) and x_2 (blue) for case described in Section 3.4.1

3.4.2 Dynamic behavior after a variation of the irradiation level

An irradiance variation from $G = 900W/m^2$ to $G = 200W/m^2$ is applied (see Tab.3.2) after the system has reached the steady state operation corresponding to $[x_1, x_2, x_4] = [0, 0, V_{ref} = 6V]$, which is the central point of the RoE shown in Fig. 3.14.a. The significant variation of the irradiance level causes the operating point moving outside the RoE (see Fig.3.14). The reachability conditions are still valid out of RoE, thus the system starts from an operating point which is located outside the RoE and moves towards the straight line of the hysteresis band according to (3.5) (branch A of the evolution in Fig.3.14.b) . Thus, the new starting point is inside the RoE and the system evolves, according to the new substructure just entered, by an additional natural evolution (branch B of the evolution in Fig.3.14.b). Afterwards, the SM operation is restored. The time domain simulation results shown in Fig.3.15 put into evidence that the irradiance variation causes a transient dynamic behavior that does not fulfill the designed value

of the settling time, fixed at about $33\mu s$, because of the sequence of the additional natural evolutions discussed above. This event can be avoided by enlarging the RoE through a different design of the k_1, k_2 and C_{in} values.

As a final example, the parameters values given in Tab.3.3 have been used in order to show what happens if the coefficient α in (3.37) is greater than zero because of a violation of the condition (3.26). In this case the eigenvalues associated with the output L-C cell show a positive real part, so that the system is unstable. In particular, x_4 shows a divergent oscillation behavior, thus the system goes out of the RoE due to the variation along the x_4 axis. Although from a mathematical point of view the condition (3.26) might be violated, in practice this does not happen because it would mean that the PV generator works as a load and some power is injected from the dc/dc converter output. As in any PV power processing system, the energy back flow must be avoided; in the case treated in this paper, and shown in Fig.3.2, the synchronous topology has been considered in order to have two substructures only and to achieve a higher efficiency. Thus, fulfilling the condition (3.26) means to adopt a further hardware, e.g. a blocking diode, or a software control avoiding the current back flow.

Par.	**Values and variations**	**Values and variations**
G	$900W/m^2 \rightarrow 200W/m^2$	$900W/m^2 \rightarrow 100W/m^2$
I_{pv}	$6.86A \rightarrow 1.48A$	$6.68A \rightarrow 0.67A$
R_{diff}	$6\Omega \rightarrow 121\Omega$	$2.5\Omega \rightarrow 10\Omega$
V_{ref}	$7V$	$8.25V$
k_2	-0.436	-0.436
k_1	0.165	0.165

Table 3.3: Parameters values used in the two examples of Section 3.4.2

By simulating the PV system in the conditions listed in Tab.3.3, the behavior shown in Fig.3.16 is obtained. By looking at the

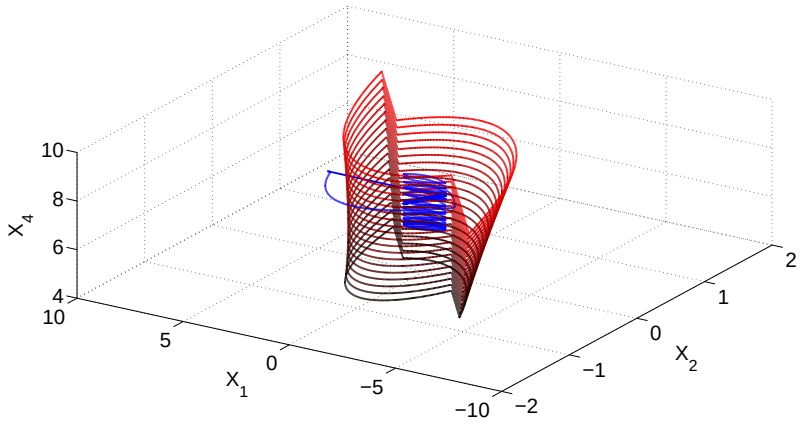

(a) Three-dimensional RoE

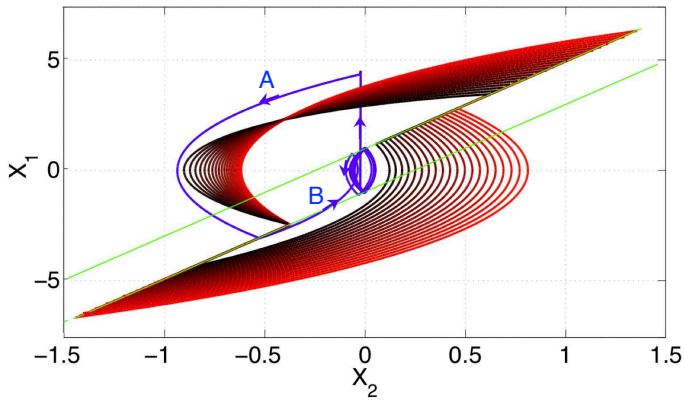

(b) Bi-dimensional RoE

Figure 3.14: RoE and path of the operating point for the first case described in Section 3.4.2

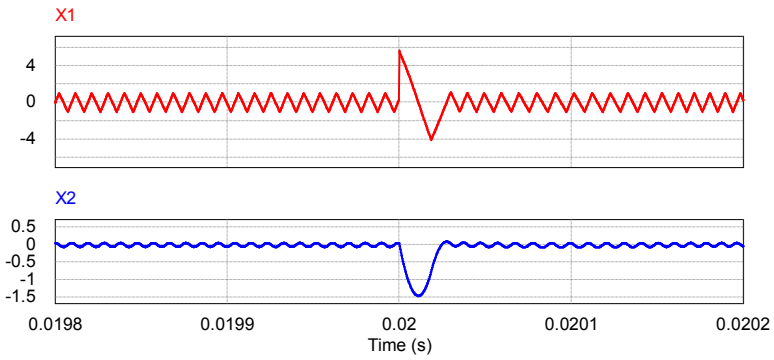

Figure 3.15: Waveforms of x_1 (red) and x_2 (blue) for the first case described in Section 3.4.2

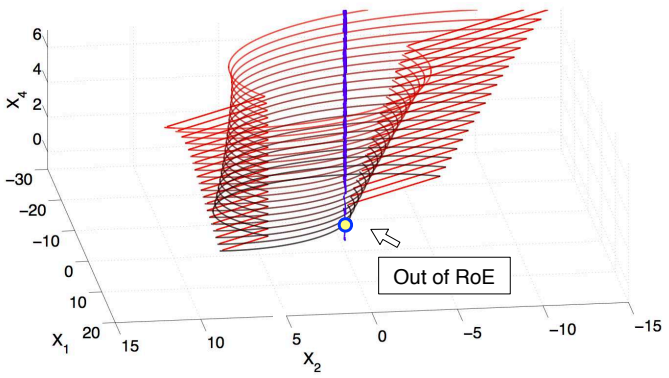

Figure 3.16: RoE and path of the operating point for the second case described in Section 3.4.2

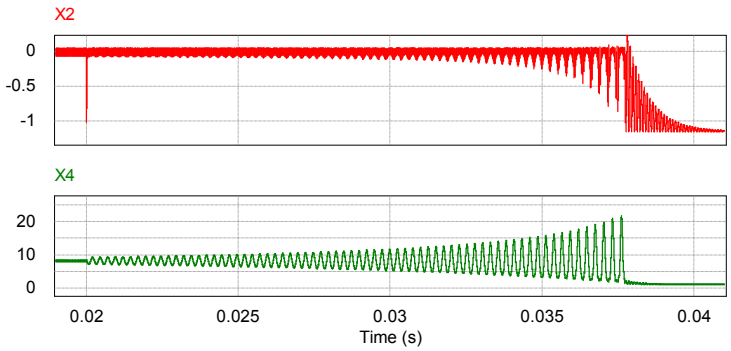

Figure 3.17: Waveforms of x_1 (red) and x_2 (blue) for the second case described in Section 3.4.2

time domain simulation results shown in Fig.3.17, it results that at $0.02s$, thus when the irradiance step is applied, the state variable x_2 still has a stable behavior. This was predicted by the negative value assumed by λ_1 in (3.37) and is confirmed by the magnification shown in Fig.3.18.a. On the contrary, as predicted by the positive values of the real part of $\lambda_{2,3}$ in (3.37), the state variable x_4 starts to show an oscillation (see Fig.3.18.b) whose amplitude increases up to the operating point exits from the RoE (see Fig.3.16). As shown in Fig.3.18.b, at about $0.038s$ the switching operation stops and, due to the violation of the reachability condition (3.26), the operating point is not directed towards the sliding surface, but it evolves according to the dynamics of the substructure.

3.5 Experimental results

The experimental validation has been obtained by means of a laboratory prototype of the converter shown in Fig.3.2. The parameters' values are those ones given in Tab.3.2. The SM controller is implemented by means of a digital controller as described in [MPS13]. The SM controller parameters have been designed according to the criteria obtained by means of the analysis described

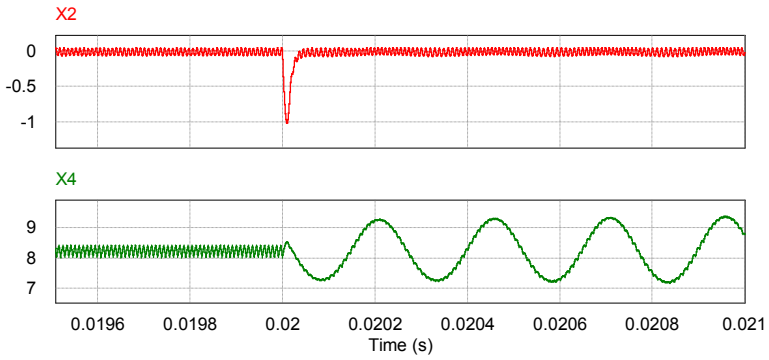

(a) System oscillation

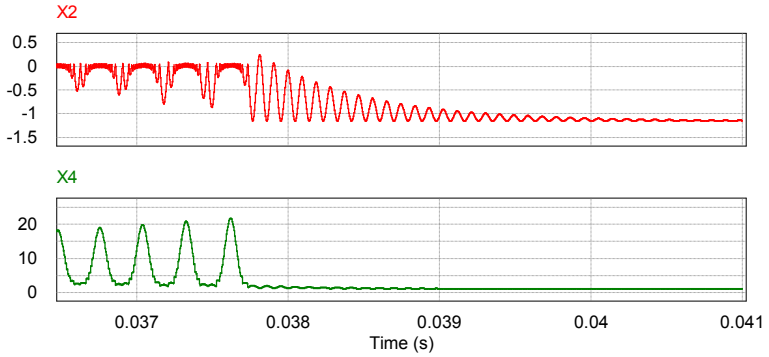

(b) System switching off

Figure 3.18: Two magnifications of the x_1 (red) and x_2 (blue) waveforms for the second case described in Section 3.4.2

in the previous sections. Fig.3.19 shows the time domain simulation results obtained in PSIM by imposing a step variation of 2V on the reference voltage V_{ref} with $k_1 = 0.165$ and $k_2 = -0.218$.

According to the λ_1 value in (3.37), a time constant of $16.6us$ and

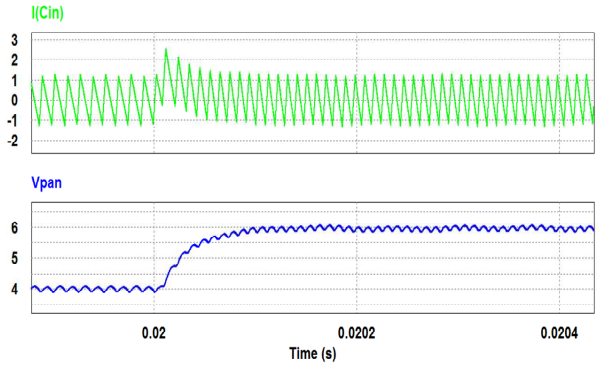

Figure 3.19: Step response: simulation result obtained by PSIM ®

a rise time of $70us$ have been designed. The experimental measurements given in Fig.3.20 validate the simulation results. The very good agreement is also confirmed by Fig.3.21, where the section of the RoE, the sliding surface and the experimental behavior of the system operating point have been plotted together in the phase plane. The SM control holds for the whole transient and the system keeps far from the boundary of the RoE.

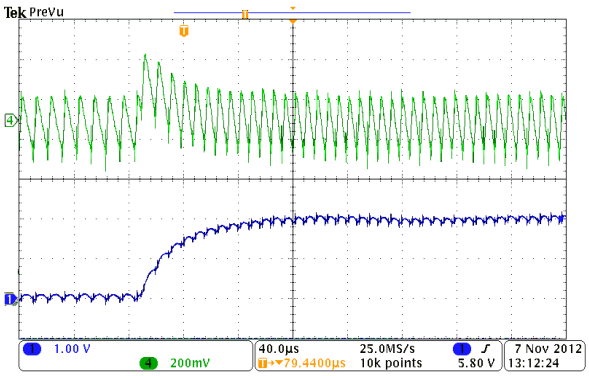

Figure 3.20: Step response: experimental result

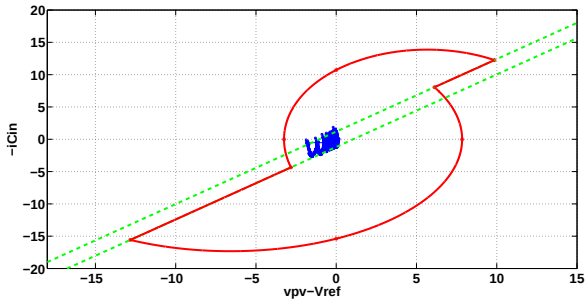

(a) Experimental RoE

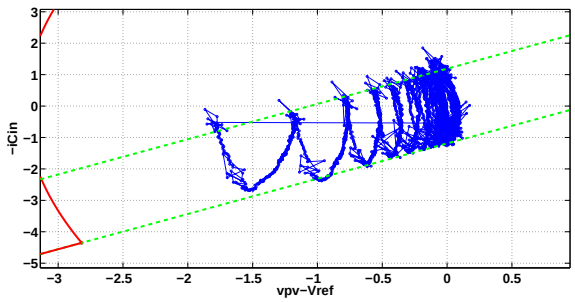

(b) Magnification

Figure 3.21: Transient in the phase plane: experimental result

Chapter 4

Dynamic Modeling of SM Controlled DC/DC converters for PV applications

PhotoVoltaic (PV) applications require an accurate design of the power processing system, both in terms of power stage and closed loop compensators. As shown in [FPSV12], a proper design of the linear feedback control of the dc/dc converter allows to improve the steady state and dynamic performances of the MPPT control. Unfortunately, the linear compensator design is not immediate.

The frequency modeling of the SM controlled closed loop system, which is mandatory for the controller design, cannot be afforded easily by means of the classical techniques. This because the validity of the linear model is usually restricted to the frequencies below one tenth of the switching frequency. Instead, the large frequency response of the SM control requires an accurate analysis also above such a limit in order to predict the system dynamic performances accurately. In the literature some effort has been carried out for extending the validity of the linear models in a larger frequency range: this has been done for the current based controllers but, unfortunately, without including the SM control. The aver-

aged models used for current controlled converters working at a constant switching frequency allow to simplify the design of the feedback loop to the aim of improving the dynamic performance of the system [EM01]. The application of such techniques to the SM controlled converters is not a trivial task because of the variability of the switching frequency and of the intrinsic non linearity of the control law. In literature, some papers (e.g. [Sun02a]) have been dedicated to the small signal modeling of converters working at a variable switching frequency, based on hysteretic constant on-time or constant off-time techniques.

In [Sun02b] a unified approach to the ac modeling of converters working in continuous as well as in discontinuous conduction mode is proposed: it refers to direct on-time control at fixed as well as variable frequency.

In [PC06] the small signal modeling of hysteretic current mode control is presented: the critical and the fixed band current modes are analyzed, but the proposed approach is not extended to the SM control, which has its own peculiarities.

In [YLM12] a significant effort for unifying the small signal analysis of different current mode controls applied to various converters' topologies is done. Nevertheless, the application of the same approach cannot be applied straightforwardly to the SM control technique analyzed in this thesis, because of the peculiar variables taken into account and included in the sliding surface oriented to an MPPT PV application.

In the following sections a linearized dynamic model of the SM controller presented in the previous chapters has been derived. It has been obtained in a general form which has been applied to the boost and to the Single Ended Primary Inductor Converter (SEPIC) topologies, these deserving a high interest in distributed PV applications. The analysis clearly puts into evidence some of the benefits of the proposed SM control technique with respect to the classical linear control.

As expected, the developed model exhibits a significant error with respect to the simulation results in the frequency range above the conventional limit of one tenth of the switching frequency. In

literature, e.g. in [CDNFZ11], the problem is often avoided by choosing a crossover frequency that is significantly lower than the switching frequency. This might be done also in case of variable frequency control techniques, by operating a design based on the minimum switching frequency at which the converter will operate.

The need of corrective terms allowing a more accurate model at high frequency is put into evidence in [YLM12] as well as in some other papers.

In the second part of this chapter an analysis of this corrective term is carried out for the PV applications under study. The corrective term is calculated by comparing the dynamic model of the converter obtained by means of the equivalent control approach and that one resulting from the averaging method developed in the first part of this work.

The proposed analysis is the starting point of a future work of generalization of the corrective term.

4.1 Functional block diagram of the SM controlled converters

The referring SM control architecture is shown in Fig.4.1 and it is described by the following equation [BCG+13]:

$$S = k_1 \cdot (-i_{c_{in}}) + k_2 \cdot (v_{pv} - v_{ref}) \tag{4.1}$$

The SM controller acts on the input cell of the converter, which consists of the PV source and the converter's input capacitance. The former is modeled by the Norton equivalent circuit, where the parameter R_{diff} is the differential resistance of the PV source in its operating point and the current i_{pv} depends on the irradiance level and on the PV output voltage. By looking at Fig.4.1, it is evident that the analysis proposed in this section can be applied to a wide class of converters topologies.

It is also assumed that the converter always works in continuous conduction mode, e.g. it is a synchronous one. The converter's small signal model is usually derived by assuming a fixed

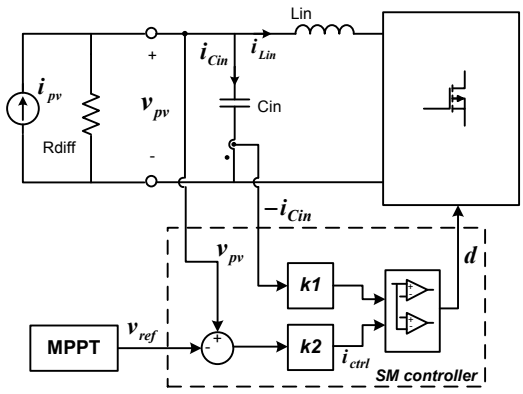

Figure 4.1: The input stage of the switching converter, the PV linear model and the SM controller

switching frequency operation. The switching period is divided into subintervals and the averaged model is obtained by looking at the constitutive equations of the reactive components. Afterwards, the small-signal dynamic model is obtained by perturbing and linearizing the large signal model [EM01]. Thus, the way in which the small signal model of any converter can be derived is a well known procedure.

By using the SM control, the switching frequency is not constant and the duty cycle value is non linearly related to the control voltage. As a consequence, perturbations must be kept into account in both the intervals of the switching period T_s:

$$D + \hat{d} = \frac{T_{on}}{T_s} + \frac{\hat{t}_{on}}{T_s} - \frac{T_{on}}{T_s^2}\hat{t}_s = \frac{T_{on}}{T_s} + \frac{\hat{t}_{on} - D\hat{t}_s}{T_s} \tag{4.2}$$

where:

$$\hat{t}_s = \hat{t}_{on} + \hat{t}_{off} \tag{4.3}$$

is the small signal variation of the switching period, which is the sum of the small signal variations of both the two subintervals T_s is divided into.

Fig.4.2 shows the waveform of the input capacitor current in the hysteresis band, whose width is H, imposed by the SM controller. In this figure, m_1 and m_2 are the slopes of $i_{Cin}(t)$ in the two subintervals, k_1 is the SM cofficient.

By looking at Fig.4.2, it descends that:

$$i_{ctrl}(t) = k_1 \cdot < -i_{Cin}(t) >_{T_s} + \frac{t_{on}(t)}{2} \cdot m_1(t) \tag{4.4}$$

from which the expression of t_{on} can be obtained. On the other side, it is:

$$t_{off}(t) = -\frac{H}{m_2(t)} \tag{4.5}$$

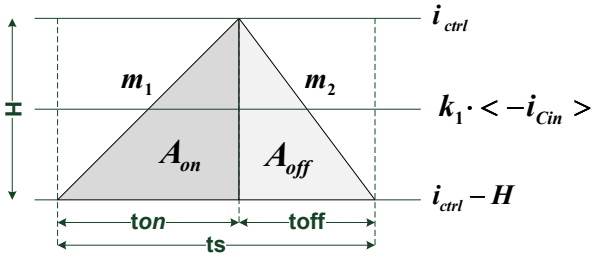

Figure 4.2: Input capacitor current waveform under the SM control

The expression of the time varying duration of the two subintervals $t_{on}(t)$ and $t_{off}(t)$ can be calculated by perturbing the following variables:

$$\begin{aligned} i_{Cin}(t) &= I_{Cin} + \hat{i}_{Cin}(t) \\ i_{ctrl}(t) &= I_{ctrl} + \hat{i}_{ctrl}(t) \\ m_1(t) &= M_1 + \hat{m}_1(t) \\ m_2(t) &= M_2 + \hat{m}_2(t) \end{aligned}$$

Thus, from (4.4) and (4.5) it results that:

$$\hat{t}_{on} = \frac{2}{M_1} \cdot (\hat{i}_{ctrl} + k_1 \hat{i}_{Cin}) - \frac{2I_{ctrl}}{M_1^2} \cdot \hat{m}_1 \tag{4.6}$$

$$\hat{t}_{off} = -\frac{H}{M_2^2} \cdot \hat{m}_2 \tag{4.7}$$

By means of (4.2) and by keeping into account (4.3), (4.6) and (4.7) it results that the small signal variation of the duty cycle is:

$$\begin{aligned} \hat{d} = & \frac{2(1-D)}{M_1 T_s} \cdot (\hat{i}_{ctrl} + k_1 \hat{i}_{Cin}) + \\ & - \frac{2(1-D) I_{ctrl}}{T_s M_1^2} \cdot \hat{m}_1 - \frac{DH}{T_s M_2^2} \cdot \hat{m}_2 \end{aligned} \tag{4.8}$$

In the following, the control equation is particularized for the boost and the SEPIC SM controlled converters. By assuming, as usual, that the current ripple in the input capacitor is equal to the input inductor current ripple and by analyzing the converters' topologies in the two subintervals, the slopes m_1 and m_2 are expressed as shown in Tab.4.1. As a consequence, the expression (4.8) can be rewritten as follows:

$$\hat{d} = F_m \cdot [F_c(\hat{i}_{ctrl} \ + \ k_1 \cdot \hat{i}_{Cin}) + F_g \hat{v}_{pv} + F_v(\hat{v}_{Cs} + \hat{v}_o)] \tag{4.9}$$

where $\hat{v}_{pv}(t)$ and $\hat{v}_o(t)$ are the low frequency variations of converter's input and output voltages respectively, and $\hat{v}_{Cs}$ is the low frequency variation of the coupling capacitor voltage in the SEPIC converter. The expressions of the coefficients F_m, F_c, F_g, F_v are reported in Table 4.2. Of course, for the boost converter, the same expression 4.9 and the same terms listed in Tab.4.2 can be derived, by only putting $V_{Cs} = 0$ and $\hat{v}_{Cs} = 0$.

The block diagram of the controller can be sketched as in Fig.4.3. The linearized model of the boost converter, including the components' ESRs and the MOSFET ON resistances, is shown in Fig.4.4.

	boost	SEPIC
$m_1(t)$	$k_1 \cdot \frac{v_{pv}(t)}{L_{in}}$	$k_1 \cdot \frac{v_{pv}(t)}{L_{in}}$
$m_2(t)$	$k_1 \cdot \frac{v_{pv}(t)-v_o(t)}{L_{in}}$	$k_1 \cdot \frac{v_{pv}(t)-v_{Cs}(t)-v_o(t)}{L_{in}}$

Table 4.1: Current slopes

F_m	$\frac{L_{in}}{k_1 T_s V_{pv}}$
F_c	$2 \cdot (1 - D)$
F_g	$-\frac{2(1-D)I_{ctrl}}{V_{pv}} - \frac{HDV_{pv}}{(V_{pv}-V_{cs}-V_o)^2}$
F_v	$\frac{HDV_{pv}}{(V_{pv}-V_{cs}-V_o)^2}$
T_s	$\frac{2L_{in}I_{ctrl}}{k_1 V_{pv}} - \frac{HL_{in}}{k_1(V_{pv}-V_{Cs}-V_o)}$

Table 4.2: SM coefficients

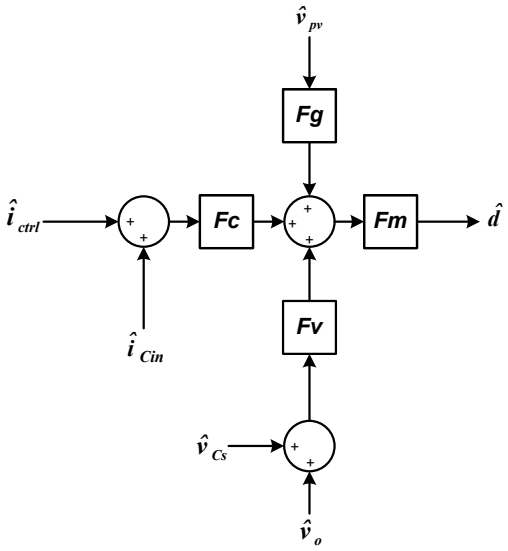

Figure 4.3: Functional block diagram of the SM controller for the SEPIC converter.

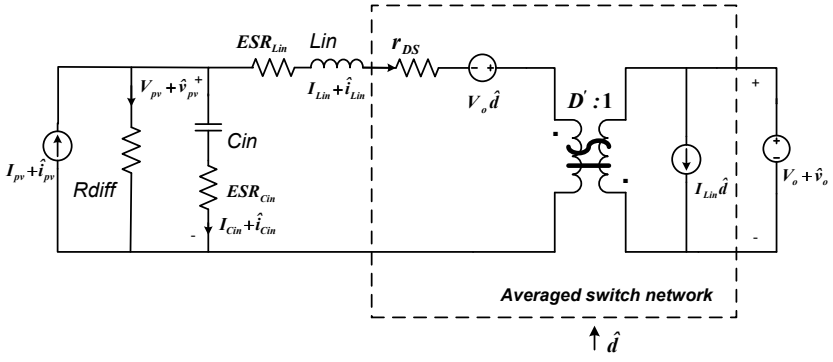

Figure 4.4: dc and small-signal ac averaged circuit of the CCM boost converter

The averaged switch network is represented by the following equations:

$$V_1 + \hat{v}_1(t) = (V_2 + \hat{v}_2(t))(D' - \hat{d}) + r_{DS}(I_1 + \hat{i}_1(t)) \tag{4.10}$$

$$I_2 + \hat{i}_2(t) = (D' - \hat{d})(I_1 + \hat{i}_1(t)) \tag{4.11}$$

The linearized model of the SEPIC converter, including the components' ESRs and the MOSFET ON resistances, is shown in Fig.4.5.

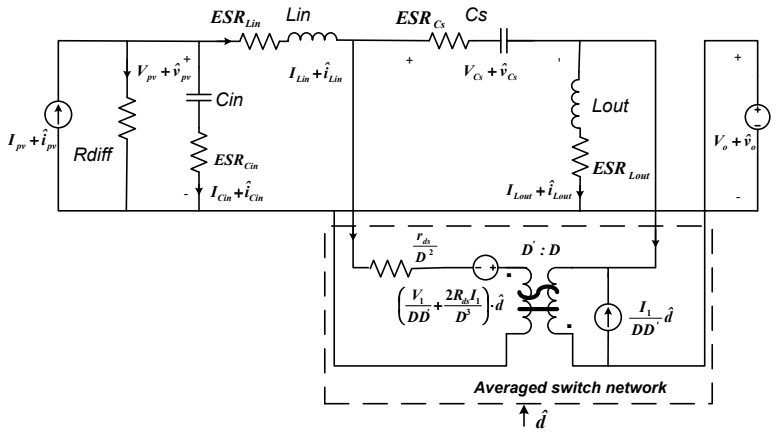

Figure 4.5: dc and small-signal ac averaged circuit model of the CCM SEPIC Converter

It has been obtained by means of a standard procedure that uses the averaged model of the switching cell and matches it with the remaining part of the converter. Finally, it results that:

$$V_1 + \hat{v}_1(t) = \frac{D'}{D}(V_2 + \hat{v}_2(t)) + \frac{r_{DS}}{D^2}(I_1 + \hat{i}_1(t)) - \frac{V_2}{D^2}\hat{d} - 2\frac{r_{DS}I_1}{D^3}\hat{d} \tag{4.12}$$

$$I_2 + \hat{i}_2(t) = \frac{D'}{D}(I_1 + \hat{i}_1(t)) - \hat{d}(\frac{I_2}{DD'}) \tag{4.13}$$

The complete system dynamic model including the parasitic elements can obtained easily by combining the SM control equation (4.9) with the converter's transfer functions.

4.2 Open loop and closed loop transfer functions

In order to study the dynamic behavior of the closed loop converter, its open loop behavior must be firstly described by a set of transfer functions relating the input voltage of the converter, that is the PV voltage $\hat{v}_{pv}$, to the duty cycle $\hat{d}$, the output voltage $\hat{v}_o$ and the input current $\hat{i}_{pv}$ as follows:

$$\begin{aligned}\hat{v}_{pv}(s) = G_{v_{pv},d}(s)\hat{d}(s) + G_{v_{pv},i_{pv}}(s)\hat{i}_{pv}(s) + \\ + G_{v_{pv},v_o}(s)\hat{v}_o(s)\end{aligned} \tag{4.14}$$

In the same way, the relationships giving the dynamic behavior of the input current capacitor and, in the SEPIC converter, the coupling capacitor can be written:

$$\begin{aligned}\hat{i}_{Cin}(s) = G_{i_{Cin},d}(s)\hat{d}(s) + G_{i_{Cin},i_{pv}}(s)\hat{i}_{pv}(s) + \\ + G_{i_{Cin},v_o}(s)\hat{v}_o(s)\end{aligned} \tag{4.15}$$

$$\begin{aligned}\hat{v}_{Cs}(s) = G_{v_{Cs},d}(s)\hat{d}(s) + G_{v_{Cs},i_{pv}}(s)\hat{i}_{pv}(s) + \\ + G_{v_{Cs},v_o}(s)\hat{v}_o(s)\end{aligned} \tag{4.16}$$

Such links among the variables are summarized as in Fig.4.6, which is referred to the SEPIC converter. A similar, and more simple, block diagram can be obtained for the boost converter by neglecting in the scheme of Fig.4.6 the contributions depending on the coupling capacitance.

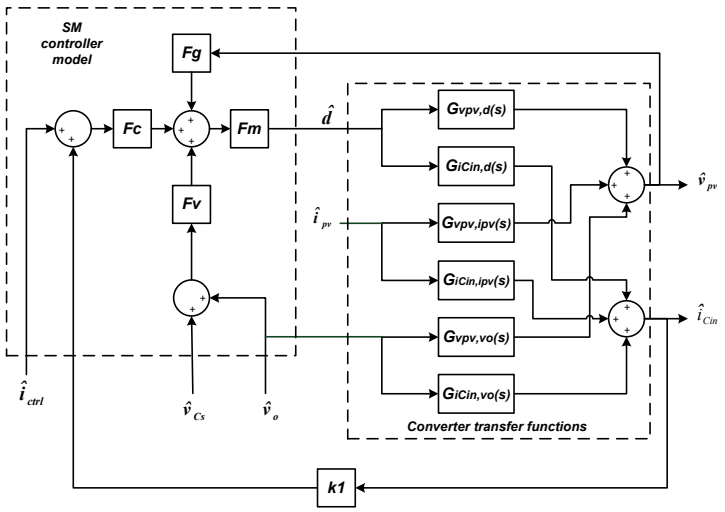

(a)

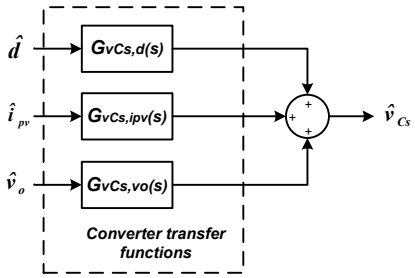

(b)

Figure 4.6: Block diagram that models the SM controlled SEPIC Converter

Usually in PV applications the main transfer function used to design the MPPT algorithm is that one relating the control signal to the PV voltage. For a converter operating in open loop the control signal is the duty cycle, so that the interest is in the transfer function:

$$G_{v_{pv},d}(s) = \frac{\hat{v}_{pv}}{\hat{d}}\Big|_{\hat{v}_o(s)=0,\ \hat{i}_{pv}(s)} \tag{4.17}$$

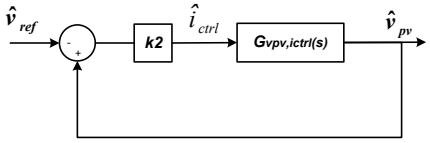

Figure 4.7: Voltage Loop of the SM based MPPT technique

For the control architecture proposed and shown in Fig.4.1, the MPPT is designed by analyzing the control scheme shown in fig.4.7, thus studying the transfer function:

$$G_{v_{pv},i_{ctrl}}(s) = \frac{\hat{v}_{pv}}{\hat{i}_{ctrl}}\Big|_{\hat{v}_o(s)=0,\ \hat{i}_{pv}(s)=0} \tag{4.18}$$

It is the closed loop transfer function accounting for the converter transfer functions and the SM controller.
For the SEPIC converter, by using the relations for $\hat{v}_{cs}$ e $\hat{i}_{Cin}$ given in (4.15) and (4.16) in which $\hat{v}_o$ and $\hat{i}_{pv}$ are settled to zero as required by (4.18), by looking at the Fig.4.7 and by keeping into account the expression of the sliding surface (4.1), it results that:

$$\hat{d} = \frac{F_m \cdot (F_c \hat{i}_{ctrl} + F_g \hat{v}_{pv})}{1 - F_m \cdot (F_c k_1 G_{i_{Cin},d} + F_v G_{v_{Cs},d})} \tag{4.19}$$

Finally, by putting (4.19) in (4.14) the closed loop transfer function (4.18) for the SEPIC converter is expressed as a function of some open loop transfer functions:

$$G_{v_{pv},i_{ctrl}}(s) = \frac{F_m F_c G_{v_{pv},d}}{1 - F_m \cdot (F_c k_1 G_{i_{Cin},d} + F_v G_{v_{Cs},d} + F_g G_{v_{pv},d})} \tag{4.20}$$

The same transfer function for the boost converter has the following expression:

$$G_{v_{pv},i_{ctrl}}(s) = \frac{F_m F_c G_{v_{pv},d}}{1 - F_m \cdot (F_c k_1 G_{i_{Cin},d} + F_g G_{v_{pv},d})} \tag{4.21}$$

where $G_{v_{pv},d}$ and $G_{i_{Cin},d}$ are evidently related to the boost topology.

Thanks to the proposed model, the benefits of the MPPT architecture in terms of the dynamic behavior can be appreciated. In order to do this, a numerical example is proposed. The values used for the boost and SEPIC converters are reported in Tab.4.3 and 4.4 respectively.

parameter	**value**	**parameter**	**value**
L_{in}	$13.6\mu H$	ESR_{Lin}	$16m\Omega$
C_{in}	$110\mu F$	ESR_{Cin}	$6m\Omega$
$r_{DS}(L_Mos)$	$6.5m\Omega$	$r_{DS}(H_Mos)$	$6.5m\Omega$
V_o	12V	V_{ref}	6V
I_{pv}	3A	R_{diff}	5Ω
F_s	100kHz	H	0.126
k_1	0.165	k_2	0.3

Table 4.3: boost converter parameters' values

Fig. 4.8 shows the comparison among the converter open-loop and the SM current-closed loop transfer functions (4.20) and (4.21) for the two converters. It is evident that the typical resonant peaks, appearing in the converter transfer functions, have been flattened by the SM controller.
It is worth noting that, by looking at the control scheme shown

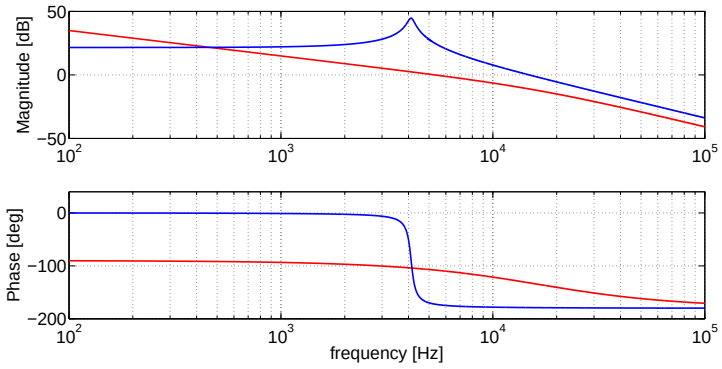

(a) boost

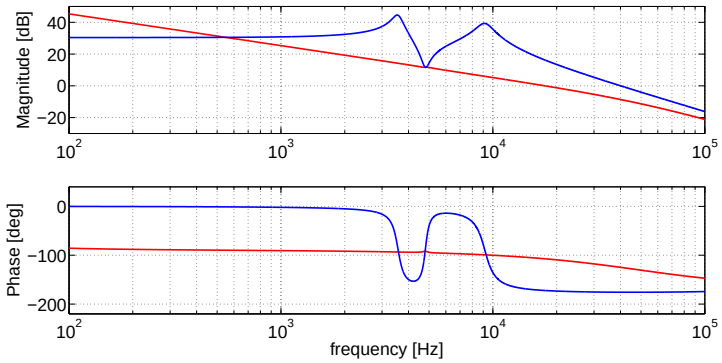

(b) SEPIC

Figure 4.8: Open-loop (blue) vs SM closed-loop (red) control-to-v_{pv} transfer functions

parameter	value	parameter	value
L_{in}	$15\mu H$	ESR_{Lin}	$12m\Omega$
C_{in}	$22\mu F$	ESR_{Cin}	$3m\Omega$
L_{out}	$15\mu H$	ESR_{Lout}	$12m\Omega$
C_s	$44\mu F$	ESR_{Cs}	$6m\Omega$
$r_{DS}(L_Mos)$	$6.5m\Omega$	$r_{DS}(H_Mos)$	$6.5m\Omega$
V_o	12V	V_{ref}	6V
I_{pv}	3A	R_{diff}	5Ω
F_s	140kHz	H	0.126
k_1	0.165	k_2	0.218

Table 4.4: SEPIC converter parameters' values

in Fig.4.7, the $G_{v_{pv},i_{ctrl}}(s)$ is the only transfer function that affects the voltage loop gain, thus the MPPT parameters values can be settled on the basis of it only. Moreover, as shown in Fig.4.8, the $G_{v_{pv},i_{ctrl}}(s)$ behavior is almost invariant with respect to the converter used for acting the MPPT.

In order to validate the proposed SM ac-model, a comparison with the PSIM simulations has been performed. In Fig.4.9 the voltage loop gains for the boost and SEPIC converters have been shown. The fitting is almost perfect in the low frequency range while at high frequencies a significant phase error is evident. This discrepancy is a usual problem in the averaged models of the current based controllers, thus in the following an improvement of the SM ac-model is discussed.

4.3 Reliability of the model at high frequencies and the correction factor

In the previous section the low frequency model of the SM controlled control converters has been obtained. This result has been achieved under the assumption that the control signal i_{ctrl} is slowly varying in the switching period, as shown in Fig.4.2. A graphical

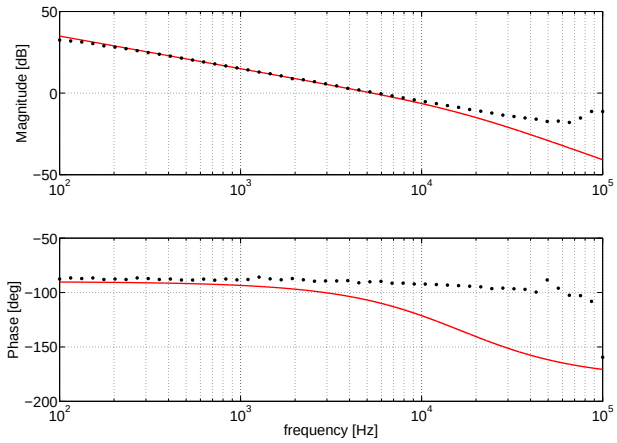

(a) boost

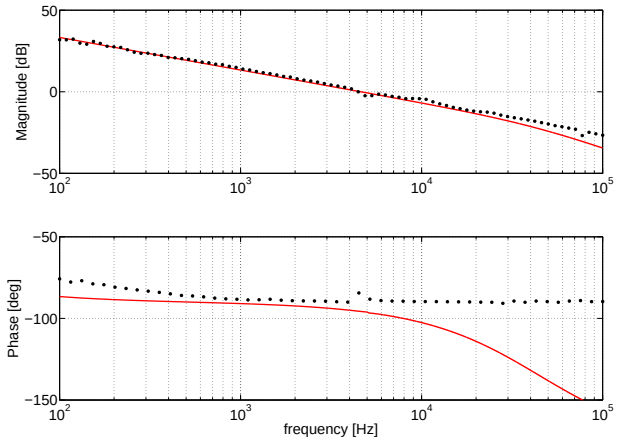

(b) SEPIC

Figure 4.9: SM voltage loop gain: MATLAB model (red line), PSIM simulation (black dots)

approach [PC06], accounting for the effects of the capacitor current ripple variations in the on-time and off-time of each switching period (4.2), has allowed to calculate the equivalent duty cycle control law (4.8).

It is worth noting that the SM control acts on high frequency components, thus having an effect on i_{ctrl}. This cannot be neglected if a higher accuracy of the model above one tenth of the switching frequency is required. In fact, the PV voltage v_{pv}, appearing in the sliding surface (4.1), is affected by high frequency components that, as it is evident from Fig. 4.1, have also an effect on i_{ctrl}. The model accounting for both the high frequency components, i.e. those ones affecting i_{Cin} and shown in Fig.4.2, and those ones affecting i_{ctrl} and due to v_{pv}, would be very much complicated, so that a corrective term to be used in the SM controller models shown in Fig.4.3 is identified. The equivalent control theory [UGS09] uses the sliding law (4.1) for obtaining a non linear model of the system. This can be linearized in order to achieve an expression of the $G_{v_{pv},v_{ref}}\Big|_{EQ} = \hat{v}_{pv}(s)/\hat{v}_{ref}(s)$ transfer function. On the other side, another expression of the same transfer function can be obtained by means of the averaged approach shown in the previous Section. By adding a correction term F_p in the model shown in Fig.4.7, the model of Fig.4.10 is obtained. Thus, the correction term is identified by equating the two expressions of the $G_{v_{pv},v_{ref}}(s)$ and solving, by using a symbolic calculation tool, with respect to F_p :

$$G_{v_{pv},v_{ref}}\Big|_{EQ} = G_{v_{pv},v_{ref}}\Big|_{AVE} \tag{4.22}$$

As for the boost converter, by using an analysis similar to that one shown in [BCG+13], the analysis based on the equivalent control theory yields:

$$G_{v_{pv},v_{ref}}\Big|_{EQ} = \frac{-k_2/k_1C_{in}}{s + k_2/k_1C_{in}} \tag{4.23}$$

Instead, by accounting for the control model shown in Fig.4.10, and including the correction term to be identified, it results that:

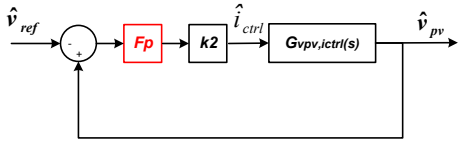

Figure 4.10: Voltage Loop of the SM based MPPT controller including the corrective term

$$G_{v_{pv},v_{ref}}\Big|_{AVE} = \frac{k_2 F_p G_{v_{pv},i_{ctrl}}}{1 - k_2 F_p G_{v_{pv},i_{ctrl}}} \tag{4.24}$$

where $G_{vpvictrl}(s)$ is given in (4.21).

By equating (4.23) and (4.24) and by solving symbolically with respect to the correction term F_p, the following expression results:

$$F_p = \frac{F_1 \cdot s^2 + F_2 \cdot s + F_3}{s} \tag{4.25}$$

where:

$$F_1 = \frac{L_{in}}{V_o F_m F_c k_1} \tag{4.26}$$

$$F_2 = 1 + \frac{L_{in}}{R_{diff} C_{in} V_o F_m F_c k_1} \tag{4.27}$$

$$F_3 = \frac{1 + V_o F_m F_v}{C_{in} V_o F_m F_c k_1} \tag{4.28}$$

It is worth noting that the correction term (4.25) is not a merely algebraic coefficient. It depends on the same quantities appearing in the model developed in Section 4.1 and reproducing the low frequency harmonic content. This result confirms that a close correlation exists between the high frequency and the low frequency contributions. Fig.4.11 shows the beneficial effect of the correction term, which allows a better fitting between the calculated response and that one simulated by PSIM.

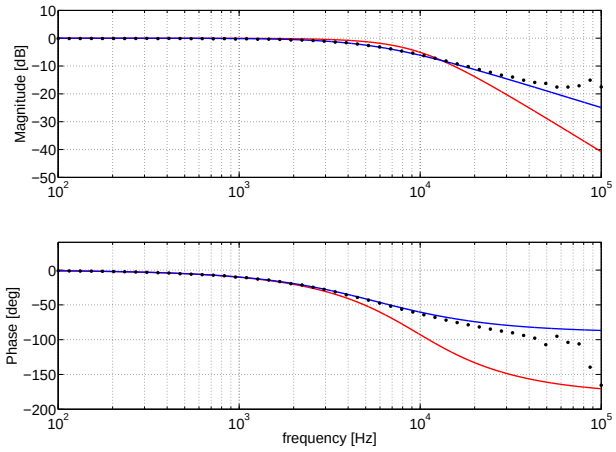

Figure 4.11: $G_{v_{pv},v_{ref}}$ of the SM controlled boost converter. Red line=model, blue line=model including the corrective term, black dots=PSIM simulation

The same procedure can be applied to the SEPIC case, thus having a good fitting (see Fig.4.12). The Bode plot of the correction term in the cases of the boost and of the SEPIC converter is shown in Fig.4.13: they differ in the dependency on the converter's parameters, but their shapes are similar.

In the next section the experimental validation of the models developed is proposed. The results are also useful for confirming the benefits offered by the SM MPPT technique proposed in [BCG+13].

4.4 Experimental Validation

The experimental tests have been focused on a prototype of SEPIC converter. Tab.4.4 summarizes the values of the parameters used for the prototype. As described in [MPS13], the SM controller has been implemented by means of a digital device, so that the $G_{v_{pv},v_{ref}}$ transfer function cannot be compared with that one shown in Fig.4.12. Nevertheless an equivalent comparison is done by look-

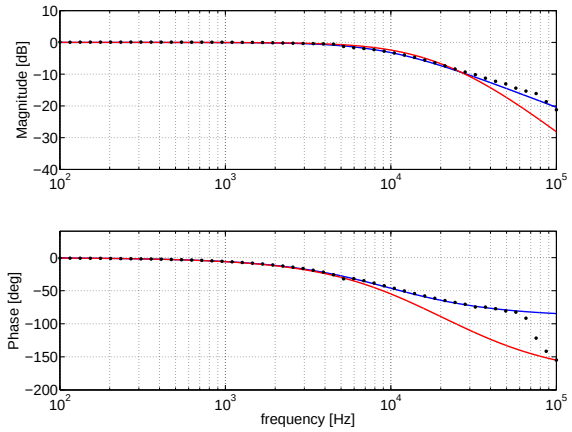

Figure 4.12: $G_{v_{pv},v_{ref}}$ of the SM controlled SEPIC converter. Red line=model, blue line=model including the corrective term, black dots=PSIM simulation

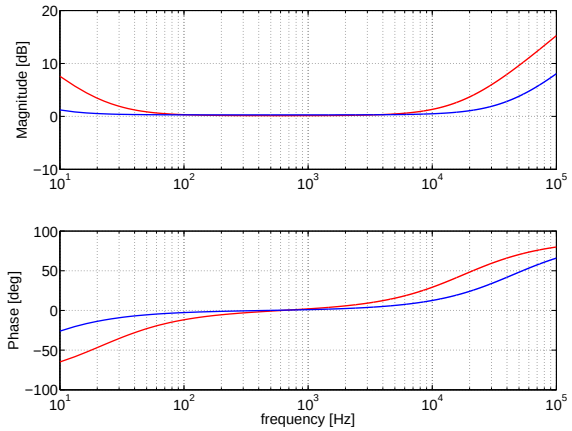

Figure 4.13: Bode plots of the correction factor F_p for boost (red line) and SEPIC (blue line) converters

ing at the voltage loop gain.

Fig.4.14 shows the way in which the voltage loop gain of the system has been experimentally measured. It looks like the one of a first order (see Fig.4.15) and this assures a simple design of the MPPT control loop. If the loop gain calculated at different irradiance levels is plotted, as it is done in Fig.4.16, one of the main features of the SM based MPPT technique is put into evidence.

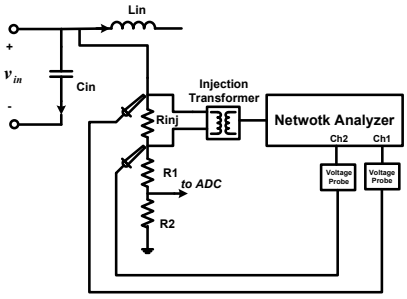

Figure 4.14: Loop gain measurement setup.

The system response remains almost unchanged at different level of irradiance, output voltage, desired input voltage and number of PV cells the module is made of. This feature is due to the SM control adopted, because the design of the phase margin and of the crossover frequency in a linear controller would have been dependent on the operating point of the system. This aspect is greatly beneficial in PV applications where the system operating point greatly changes along the day. In fact, the proposed SM control ensures the desired response performance regardless of the specific system operating point.

A further benefit of the proposed SM architecture is in its high rejection capability of noise affecting the converter's output voltage. Fig.4.17 shows the screenshot of the G_{v_{pv},v_o} transfer function of the SM controlled SEPIC converter. In this example an attenuation of -28dB is assured in the frequency range from 100Hz to 30kHz. This is very useful for reducing the detrimental effects on the MPPT efficiency that, in grid connected PV systems, causes the disturbance at a frequency that is the double of that one of

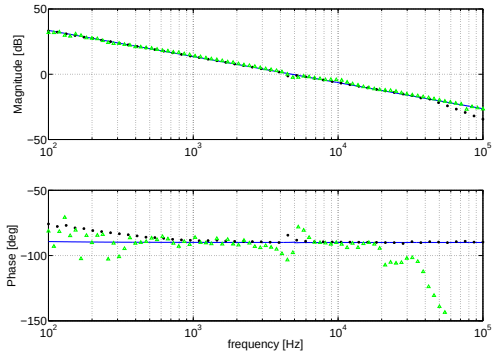

Figure 4.15: Loop gain of the SM based MPPT control for the SEPIC converter. Blue line=model including the corrective term, black dots=PSIM simulation, green triangles=experimental measurements

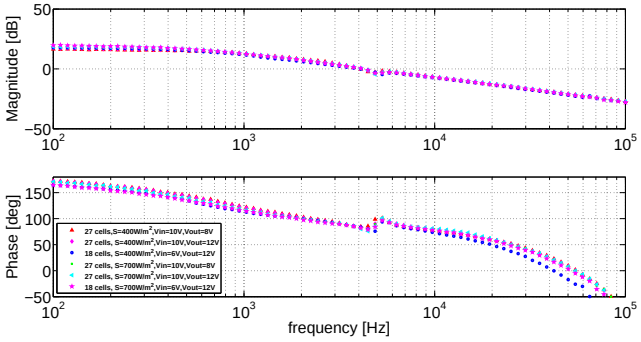

Figure 4.16: Experimental loop gain at different operating conditions

the grid voltage, appearing at the dc bus and back propagating towards the PV array terminals.

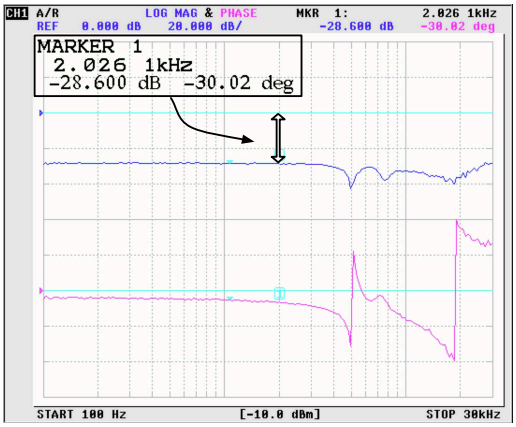

Figure 4.17: G_{v_{pv},v_o} transfer function of the SM controlled SEPIC converter.

In order to validate the proposed ac-model, additional Bode plots referring to the transfer functions relating the PV current with the coupling capacitor voltage and with the current in the SEPIC output inductance have been obtained. Moreover, the transfer functions expressing the effects of a disturbance affecting the converter's output voltage on the coupling capacitor voltage and on the output inductance current have been proposed in Figs.4.18 and 4.19 respectively.

Those Bode diagrams clearly show the very good agreement among the results obtained by means of the model developed in the previous section, the PSIM simulations and the experimental results. The larger discrepancies appear in the frequency ranges where the attenuation is very large, thus where the simulation and the experimental accuracies is low. However the high attenuation of the disturbances affecting the PV current, e.g. due to irradiance changes, and the output voltage on the voltage across the coupling capacitor C_s shows an additional benefit of the proposed architecture. Fig.4.20 collects experimental results concerning the transfer function between the voltage on the coupling capacitor

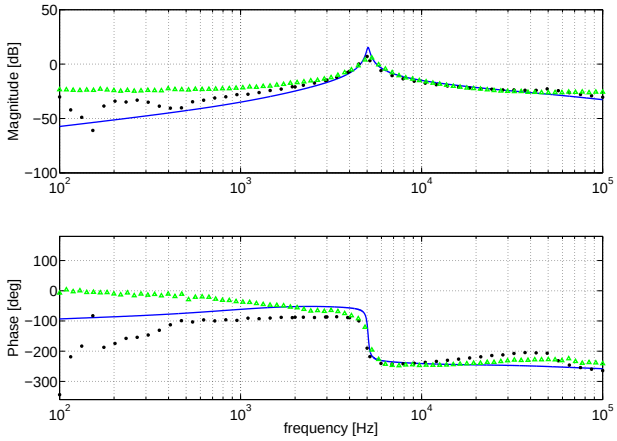

(a) i_{pv}-to-v_{Cs}

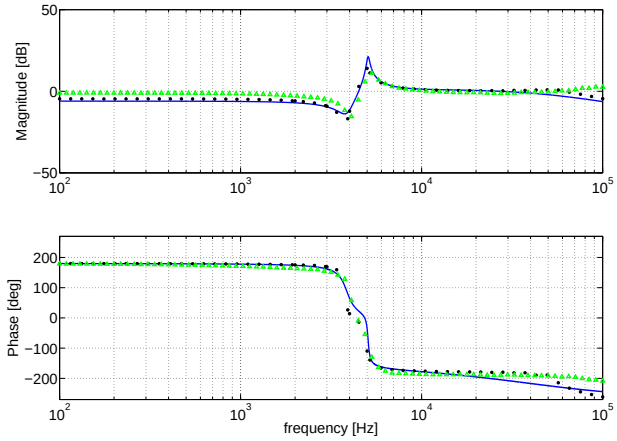

(b) i_{pv}-to-i_{Lout}

Figure 4.18: Transfer functions related to PV current variations in SM control SEPIC converter. Blue line=model including the corrective term, black dots=PSIM simulation, green triangles=experimental measurements.

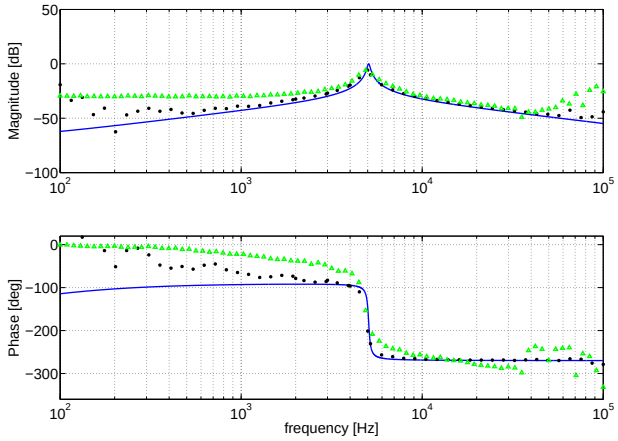

(a) v_o-to-v_{Cs}

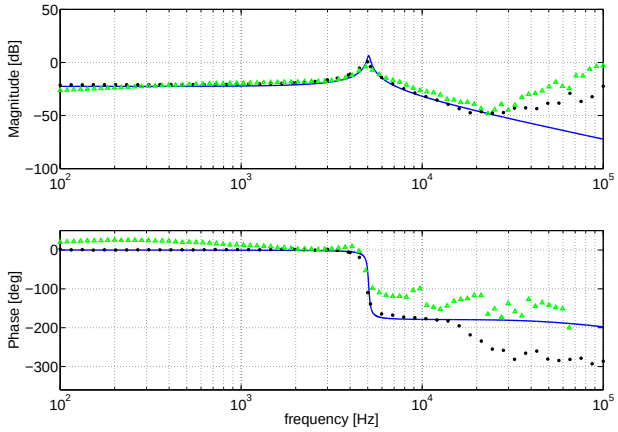

(b) v_o-to-i_{Lout}

Figure 4.19: Transfer functions related to output voltage variations in SM control SEPIC converter. Blue line=model including the corrective term, black dots=PSIM simulation, green triangles=experimental measurements.

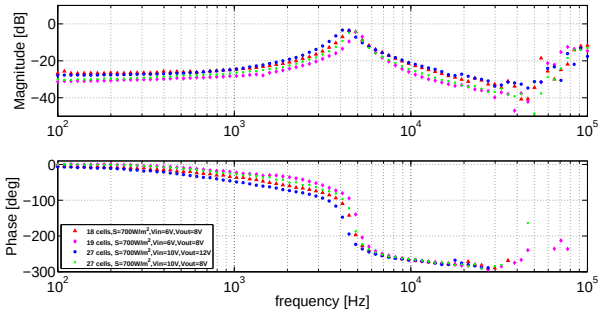

Figure 4.20: Behavior of G_{v_{Cs},v_o} transfer function at different operating conditions

and the output voltage under varying operating conditions. As expected, the transfer functions involving the converter's output cell are much more affected by the variations of the system's operating point, because of the absence of any direct control of the internal variables.

Chapter 5

An hybrid digital-analog SM controller for PV applications

As explained in the introduction, the fully digital implementation of the SM control can be carried out in different ways. Nevertheless, the possibility to implement it in an hybrid analog-digital way has not yet been investigated. The main benefit of the proposed solution is in the fact that it is possible to split the SM control equation in two terms: the first one is characterized by a combination of signals which can be defined as *fast* and a second part obtained by a combination of signals which can be defined as *slow*. It is clear that the faster term can be implemented in digital way only if high speed ADC's and/or high computational capability are available. Of course, such a solution is of poor interest for low power applications because of its high cost. Instead, the slower term suits the digital implementation because it can be treated as a linear control which works in the low frequency range, thus the problems related to the quantization errors and to the delay can be solved properly.

5.1 Selection of fast and the slow signals in the SM control equation

In the following a general procedure for identifying the fast and slow signal in the SM control will be proposed and applied for the PV architectures proposed in the previous chapter. It is worth noting that this separation depends on the specific SM equation and on the switching converter topology, so that a preliminary analysis is mandatory. In its general form the SM control is based on an equation which forces the system's variables to stay on the *sliding surface*, that is:

$$S = f(x_1, x_2, ..., x_N) = \sum_{i=1}^{N} c_i \cdot x_i = 0 \tag{5.1}$$

where N is the order of the system and x_i are the state variables. The use of a linear combination of the state variable in (5.1) results in a particularly simple implementation in SMPS applications where the sliding equation is used to perform the modulation of the switches driving signals.
The interaction among the control equation and the SMPS system is more evident if the condition given in (5.1) is expressed by means of the corresponding *real* sliding surface, in which the additional signal H is introduced in order to have an hysteresis band around the ideal condition:

$$\begin{cases} \sum_{i=1}^{N} c_i \cdot x_i > \frac{H}{2} & \rightarrow \quad \mathbf{u = 1} \\ \sum_{i=1}^{N} c_i \cdot x_i < -\frac{H}{2} & \rightarrow \quad \mathbf{u = 0} \end{cases} \tag{5.2}$$

In 5.2, **u** is the signal at the output of SM controller which is used as modulating signal for driving the switches in the SMPS. Fig.5.1 shows a simple analog implementation of the SM modulator consisting in a couple of comparators and a flip-flop. The additional signal $V = H/2$ is used to modulate the hysteresis band H, whose amplitude defines the switching frequency.

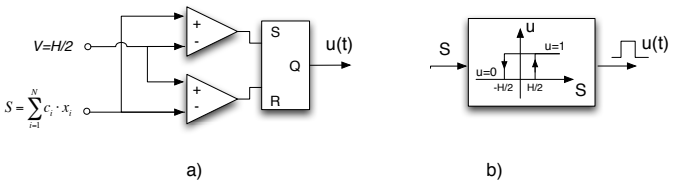

Figure 5.1: Analog implementation of the sliding-mode modulator.

If all the parts of the SM controller are implemented in a digital way, two main problems must be afforded. The first one concerns the comparator function: it is performed on quantized signals, thus it may fail if the ADC process is slow and not accurate. The second one is the time delay introduced by the digital processing: it must be a small fraction of the switching period in order to avoid significant degradation of the system phase margin. In [VICCMS11] it has been shown that it is possible to reduce the sampling hardware resources. The price to pay is an increased elaboration time which might require a digital device with very high computational capabilities.
An hybrid analog-digital implementation of the SM equation is useful if low cost micro controllers have to be used. In fact, the market offers a lot of devices having at least two analog comparator embedded on the chip. The latter, if properly configured, can be used to perform the analog part of the SM control equation.
The main issues are to define which signals must be given at the comparators' inputs in an analog form and which part of the control algorithm can be managed in a digital way without affecting its performances. The SMPS is modeled by means of the bilinear state space representation [SR87]:

$$\dot{\mathbf{x}} = \mathbf{A} \cdot \mathbf{x} + \mathbf{u} \cdot (\mathbf{B} \cdot \mathbf{x} + \gamma) + \delta \tag{5.3}$$

where $\mathbf{A}$ and $\mathbf{B}$ are square constant matrices [**NxN**], while γ and δ are vectors representing the sources. The matrices are calculated by studying the two sub-structures obtained by assigning to the

SMPS control signal **u** the two logic states u=0 and u=1. The model (5.3) is very effective for highlighting the relation between the system variables **x**, their derivatives $\dot{\mathbf{x}}$ and the modulating signal **u**. In particular, by referring to the i-th system equation, it results that:

$$\dot{x}_i = \sum_{j=1}^{N} a_{i,j} \cdot x_j + u \cdot (\sum_{j=1}^{N} b_{i,j} \cdot x_j + \gamma_i) + \delta_i \tag{5.4}$$

This equation describes how the derivative of the signal x_i depends on the modulating signal **u**. It allows an accurate calculation of the time instant at which the **u** signal commutates, thus changes its state from 0 to 1 or vice versa. In fact, if x_i is one of the variables used in (5.1), eq. (5.4) puts into evidence that the signal x_i must be accurately reproduced within the switching period, because in (5.4) the actual signal value x_i and its derivative $\dot{x}_i$ appear. In other words, because of the fact that $\dot{x}_i$ is the slope of the signal x_i, the switching time instant determined by the SM controller through (5.4) depends on the value of the variable x_i as well as on its ripple at the switching frequency. On the contrary, if the following condition holds:

$$\sum_{j=1}^{N} b_{i,j} \cdot x_j + \gamma_i = 0 \tag{5.5}$$

then the SM control does not require the information about the slope of the x_i signal, thus it can be processed in a digital way because it can be acquired with a low sampling rate without losing any information. In conclusion, those signals having their derivative directly related to the control signal cannot be processed by a low cost digital device, because they require a sampling rate that is higher than the switching frequency, so that they are best suited to be processed in an analog way. It is worth noting that the condition expressed by (5.5) is the general rule that can be used in whichever system controlled by means of the SM technique: it is

useful for identifying the signals that can be managed in a digital way without using expensive hardware resources. Signals x_i that fulfill (5.5) require a sampling rate equal to the switching frequency: in this way the SM analog/digital hybrid implementation ensures the same dynamic performances of the pure analog one [PS03].

5.2 Hybrid SM control implementation: a PV application

The SM digital implementation is described by referring to the scheme of Fig.5.2: this is not a limitation because the proposed approach can be used for implementing whichever SM control equation that can be decomposed in the way described in the previous section. Details concerning the scheme shown Fig.5.2 and the reasons of the use of SM control for improving the MPPT performances of the Perturb and Observe (P&O) technique have been discussed in this thesis and in related papers [SPV+12],[BCG+11b] and [BCG+11a].

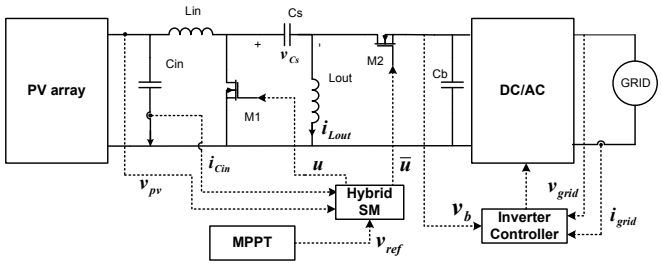

Figure 5.2: Sliding-mode control in photovoltaic application.

For the system under study, the sliding surface is reported in the following equation:

$$\begin{cases} S = & i_{Cin} - i_{ref} = \\ & = i_{Cin} - k_p \cdot (V_{ref} - v_{pv}) + \\ & -k_i \cdot \int (V_{ref} - v_{pv}(t))dt = 0 \end{cases} \tag{5.6}$$

where V_{ref} is the control signal used to set the SM modulator, as shown in Fig.5.2. Signals i_{Cin} and v_{pv}, that are the SEPIC converter capacitor current and input voltage respectively, are acquired on the dc/dc converter power stage and are used for defining the sliding surface. As explained in the previous section, the hybrid analog-digital implementation of the control algorithm requires that the signals needing a high sampling rate, so that they cannot be processed in a digital way, must be recognized. The state-space matrix representation of the SEPIC converter is derived in the chapter III and is summarized in 5.7. It has been obtained by using a simplified model of the PV field and by representing the dc/ac stage in Fig.5.2 as a constant voltage source. This assumption is based on the fact that the bulk capacitance C_b is usually so high that the voltage at its terminals is almost constant. The following condition for the driving signal has been also assumed: $\mathbf{u} = \mathbf{1} \rightarrow$ Mosfet M1 turned ON; $\mathbf{u} = \mathbf{0} \rightarrow$ Mosfet M1 turned OFF.

By defining with $\mathbf{x} = [-i_{Cin}, (v_{pv} - V_{ref}), v_{Cs}, i_{Lout}]^T$ as the vector of the SMPS variables, It results that:

$$\dot{\mathbf{x}} = \mathbf{A}\ \mathbf{x} + \mathbf{B} + (\mathbf{C}\ \mathbf{x} + \mathbf{D}) \cdot \overline{u} \tag{5.7}$$

With $\overline{u} = 1 - u$ and respectively:

$$\mathbf{A} = \begin{bmatrix} -\frac{1}{R_{diff} C_{in}} & \frac{1}{L_{in}} & 0 & 0 \\ -\frac{1}{C_{in}} & 0 & 0 & 0 \\ 0 & 0 & 0 & -\frac{1}{L_{out}} \\ 0 & 0 & \frac{1}{C_S} & 0 \end{bmatrix}$$

$$\mathbf{B} = \begin{bmatrix} \frac{V_{ref}}{L_{in}} \\ 0 \\ 0 \\ 0 \end{bmatrix}$$

$$\mathbf{C} = \begin{bmatrix} 0 & 0 & 0 & -\frac{1}{L_{in}} \\ 0 & 0 & 0 & 0 \\ 0 & 0 & 0 & \frac{1}{L_{out}} \\ \frac{1}{C_S} & -\frac{1}{R_{diff}C_s} & -\frac{1}{C_S} & 0 \end{bmatrix}$$

$$\mathbf{D} = \begin{bmatrix} -\frac{V_b}{L_{in}} \\ 0 \\ \frac{V_b}{L_{out}} \\ -\frac{V_{ref}}{C_S R_{diff}} + \frac{I_{pv}}{C_S} \end{bmatrix}$$

The matrix representation 5.7 highlights that the derivative of the capacitor current i_{Cin} affects the modulating signal $\mathbf{u}$ and is the only term in (5.6) that cannot be processed in the digital way. The SM equation (5.6) can be written by separating, on the left side, the variable that is connected directly to the analog comparators, namely i_{Cin}:

$$\begin{cases} i_{Cin} > k_p \cdot (V_{ref} - v_{pv}) + \\ \qquad +k_i \cdot \int (V_{ref} - v_{pv}(t))dt + \frac{H}{2} \quad \rightarrow \quad \mathbf{u = 0} \\ i_{Cin} < k_p \cdot (V_{ref} - v_{pv}) + \\ \qquad +k_i \cdot \int (V_{ref} - v_{pv}(t))dt - \frac{H}{2} \quad \rightarrow \quad \mathbf{u = 1} \end{cases} \tag{5.8}$$

In (5.8), the quantities at the right side can be processed in a digital way, so that a change in the values of the coefficients

appearing in them is very simple. This increases the flexibility of the control system. The reference signal V_{ref} is the output of the MPPT controller based on the P&O technique, which has usually a digital implementation. As a consequence, V_{ref} is a digital signal. Several approaches can be used for designing controllers in the discrete time domain [Oga95]. In the following, the Euler

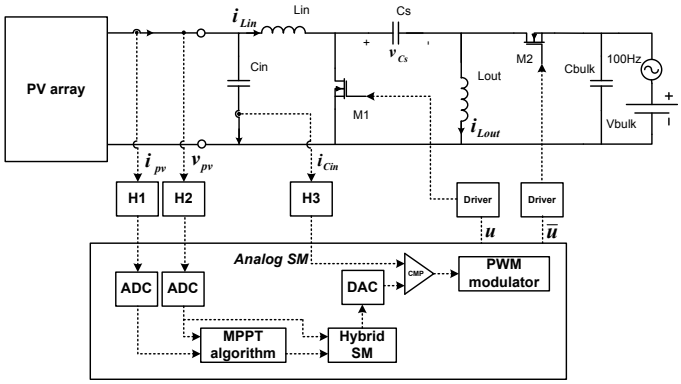

Figure 5.3: Digital SM developed by means of a micro-controller

backward transformation is used for translating the proportional and the integral terms of the control equations (5.8) into a digital form. By considering a sampling period T_c, it results that:

$$e_{(k)} = V_{(k)_{ref}} - V_{(k)_{PV}} \tag{5.9}$$

$$I_{(k)_{ref}} = I_{(k-1)_{ref}} + (k_p + k_i \cdot T_c) \cdot e_{(k)} + k_p \cdot e_{(k-1)} \tag{5.10}$$

By means of (5.10), the analog SM control (5.8) is expressed in the following hybrid way:

$$\begin{cases} i_{Cin} > I_{(k)_{ref}} + \frac{H}{2} & \rightarrow \quad \mathbf{u = 0} \\ i_{Cin} < I_{(k)_{ref}} - \frac{H}{2} & \rightarrow \quad \mathbf{u = 1} \end{cases} \tag{5.11}$$

Fig.5.3 shows the circuit schematic including the micro controller. In series with the dc generator, representing the dc bus

voltage, an additional ac generator has been inserted. The latter reproduces the voltage oscillations at a frequency that is the double of the grid frequency: such disturbance appears whenever the bulk capacitance C_b has not an infinite value and it is due to the inverter operation. inverter operating conditions can be represented by a 100Hz oscillation. The data listed in Tab.5.1 refer to a scaled version of a grid-connected photovoltaic system used for developing a laboratory prototype.

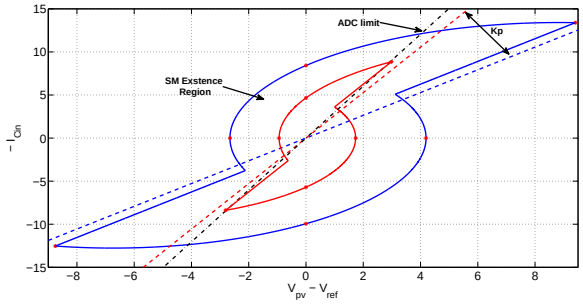

Figure 5.4: SM Existence Region and maximum speed of the SM control bounded by the ADC limit. The region with a blue contour is obtained with $k_p = 0.22$ and the one with a red contour is obtained with $k_p = 0.44$.

The scheme shown in Fig.5.3 has been accurately reproduced in the PSIM ® simulation environment, also including the sampling and quantization effect of the ADC devices, in order to verify the agreement between the analog version and the corresponding hybrid solution.
Fig.5.5 shows the waveforms obtained by simulating the scheme reported in Fig.5.3. Fig.5.5.a) shows the results obtained by simulating the system using the full analog SM control, while Fig.5.5.b) shows the results obtained by using the hybrid SM control. The only difference between the two results is in the discretization of the boundary of the sliding equation. As confirmed by the result shown in Fig.5.5.c), this negligible difference does not affect the response in terms of photovoltaic voltage significantly.

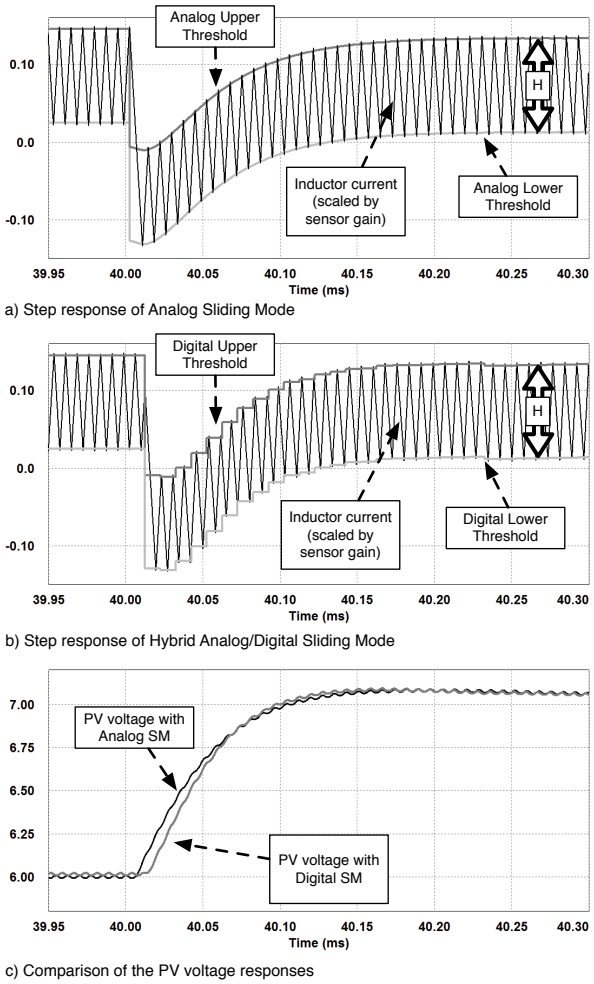

Figure 5.5: Comparison of PSIM simulations between a pure analog SM control and the proposed hybrid analog/digital SM controller

The analysis of the system behavior in the phase plane gives an additional information about the choice of the SM parameters and the characteristics of the micro-controller. Fig.3.8 shows the SM regions of existence. Moreover, the switching lines have been plotted for different values of k_1 and k_2 [SM01]. In [BCG$^+$11a] it has been shown that an increase of the $\frac{k_2}{k_1}$ value causes an increase of the slope of the switching line that corresponds to an increase in the system promptness. Thus, in order to guarantee that the analog SM implementation and the hybrid one have the same performances, the maximum slope in the SM switching line must be bounded by the ADC speed. For the case under study, the boundary where the system speed response is lower than 1/10 of the ADC sampling frequency.

5.3 Implementation of the hybrid SM controller

A Microchip®16 bit dsPIC micro controller has been selected for this application: it is equipped with two fast analog comparators that are useful for implementing the SM modulator. The memory size, the computational capability and the ADC performances are also suitable for implementing the MPPT algorithm, the digital part of the SM control and some additional routines for monitoring and safety protection. Details concerning the performances and the main characteristics of such a micro-controller are reported in Tab.5.2 and in the data sheets available online [Web11]. The first step of the implementation is the configuration of the analog block used for obtaining the SM modulator, as it is described in (5.11). The modulating signal $\mathbf{u}$ must be generated with a high resolution in terms of duty cycle and with the lowest possible delay in the transitions $0 \rightarrow 1$ and $1 \rightarrow 0$. Many micro controllers have a hardware PWM modulator based on a high frequency counter and dedicated to the generation of the modulating signals. Unfortunately, this PWM modulator is designed for working with the classical control techniques at a constant value of the switching

frequency, so that it is not suitable for implementing SM control applications. Indeed, in the photovoltaic application considered, the switching frequency can vary significantly and rapidly, so that the embedded PWM modulator becomes useless. In the following, two possible solutions for implementing the variable switching frequency modulator are presented.
The first one has been named *software modulator*, because the signals $\mathbf{u}$ and its complementary $\bar{\mathbf{u}}$ are obtained by using two General Purpouse IO pins (GPIO), configured by means of two Interrupt Service Routines (ISR) activated by the SM analog comparators. The second one has been named *hardware modulator*: it employs the embedded PWM modulator by forcing it to work with a variable frequency. In this case the SM analog comparators are electrically connected to the PWM modulator. Advantages, performances and drawbacks of the two solution are described in the following.

For the both solutions the analog comparators have been configured in the following way.

- The analog signal $i_{Cin}(t)$ is addressed at the positive input of comparators CMP1 and CMP2.

- The negative inputs of the comparators are permanently connected to the internal DACs; this gives the possibility to compare the analog signal $(i_{Cin}(t))$ with two numerical thresholds $(I_{ref} + \frac{H}{2})$ and $(I_{ref} - \frac{H}{2})$. It has been assumed that CMP1 performs the first inequality in (5.11) and the CMP2 performs the second one.

- The inputs DACs inputs have been connected to the internal references so that the thresholds are updated dynamically by performing in the software the discrete time control expressed by (5.10).

- The CMP2 must be configured in complementary logic. This because only the positive inputs of the comparators are configurable for receiving the analog signals so that, in order

PV array	**Values (STC)**
Short-circuit current I_{STC}	7.7 A
Open-circuit voltage V_{OC}	10.8 V
MPP current I_{mpp}	7.2 A
MPP voltage V_{mpp}	8.6 V
Temperature coefficient of I_{SC} (α_I)	0.07 %/^{o}C
Temperature coefficient of V_{OC} (α_V)	-0.35 %/^{o}C
SEPIC paramaters	**Nom. values**
input capacitance C_{in}	110 μF
coupled capacitance C_s	44 μF
output capacitance C_{out}	2 x 22μF
input inductance L_{in}	13.8 μH
output inductance L_{out}	13.8 μH
PV current sensor gain (H_1)	75 mV/A
PV voltage sensor gain (H_2)	0.15
Inductor current sensor gain (H_3)	75 mV/A
SM parameters	**Nom. values**
k_p	0.5
k_i	1820
T_c	100 kHz
MPPT P&O parameters [FPSV05]	**Nom. values**
Ta	25 ms
ΔV_{ref}	100 mV
Operating conditions	**Nom. values**
nominal switching frequency f_s	100 kHz
average output voltage V_{bulk}	13.5 V
100 Hz voltage amplitude $vo_{pp,100Hz}$	6 V

Table 5.1: Parameters and nominal operating conditions for the laboratory prototype

to activate the output when the analog input signal is lower than $(I_{ref} - \frac{H}{2})$, it is necessary to invert the output logic state.

Two possible approaches for obtaining the variable switching frequency modulation are considered. The best solution depends on the hardware resources available in the application, thus the output of the comparators can be used for managing the GPIO pins in the *software modulator* or for triggering the PWM block in the *hardware modulator*.

ADCs	**Nominal values**
number of BIT	10
number of channel	8
sampling rate	4 MSPS
PWM module	**Nominal values**
number of outputs	4
maximum switching frequency	$\simeq$ 1 MHz
maximum duty cycle resolution	1.04 ns
Comparators	**Nominal values**
response time	20 ns
input voltage range	0-1.65 V

Table 5.2: Main characteristics of dsPIC33FJ16GS504

5.3.1 SM controller with software modulator

This is the simpler way to implement the SM control equation (5.11) because the analog comparators are just used as triggers for two Interrupt Service Routines (ISR) in which the GPIO signals are configured. Fig.5.6 shows the detailed internal hardware configuration for the comparators and the ISR.
The hysteretic behavior of the SM modulator is assured by the fact that the ISR associated to CMP1 is dedicated to perform the $1 \rightarrow 0$ transition of the **u** signal, while the ISR associated to

CMP2 is devoted to the $1 \rightarrow 0$ transition. An interlocked mechanism based on the priority level of the two ISR's assures the right sequence and prevents multiple commutations phenomena. Another possibility is to disable the nesting ISR functionality: it consists in the fact that when a ISR is running no other ISR's can start. Fig.5.6 shows a simplified scheme and Tab.5.3 remarks the functional effect of the software SM modulator. A high flexibil-

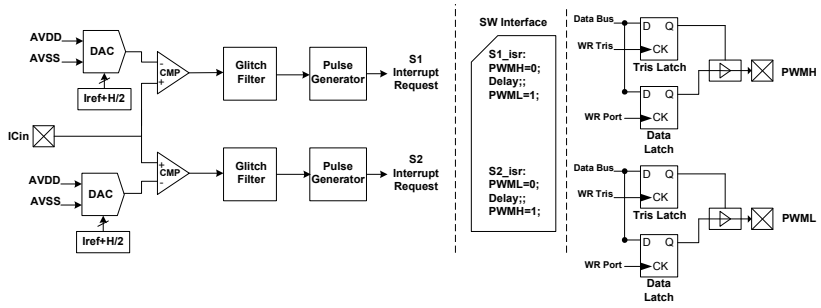

Figure 5.6: Implementation of the sliding-mode modulator with Interrupt-Service-Routine

ity is obtained because of the possibility of controlling the output signals at a software level. The other side of the coin is the calculation time required to the CPU.
In fact, it is mandatory that two ISR's must be activated in each switching period in order to perform the signal commutation, so that the percentage of CPU usage for running the ISR depends on the operations included in the ISR itself. In the proposed example the ISR's are also used for controlling the dead time between the two modulating signal, which has been fixed at 250 ns for each transition. Moreover, in order to activate as fast as possible the corresponding transitions, the ISR has been set at the highest priority, so that the ISR's running cannot be interrupted by any other process. This might be an additional drawback because the safety ISR cannot be activated.
In order to prevent undesired requests of ISR due to the presence of noise affecting the analog signal, an additional protection mech-

anism has been implemented. In the dsPic a glitch filter is already inserted but, in any case, the problem can be solved by introducing a software glitch filtering protection. The SM controller has

GPIO1$^-$	**ACMP1**	$\overline{\textbf{ACMP2}}$	**GPIO1** $= \mathbf{u}$	**GPIO2** $= \overline{u}$
0	$0 \rightarrow 1$	**x**	0	1
1	$0 \rightarrow 1$	**x**	0	1
0	**x**	$0 \rightarrow 1$	1	0
1	**x**	$0 \rightarrow 1$	1	0

Table 5.3: State transition for the SM modulator

been tested experimentally and a measure of the CPU usage for running an ISR has been carried out. The pulse on the central waveform in Fig.5.7 is the duration of a single ISR. It takes about 400 ns and it is evident that the significant part of this time is for introducing the dead time on the driving signals. This means

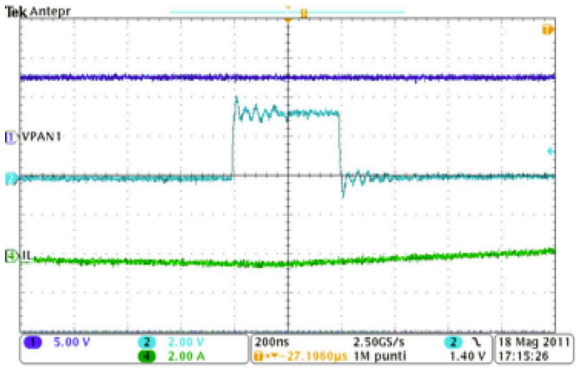

Figure 5.7: Performance evaluation of the SM modulator: the central waveform is the time duration of the ISR

that, in those application in which the dead time is managed by

the MOSFET drivers, the time consumed for the ISR reduces significantly. In any case this approach is applicable only when a small percentage of the switching period is used, in order to give the possibility to the CPU to perform other tasks (e.g. SM digital part, MPPT, monitoring). The main advantage of this approach

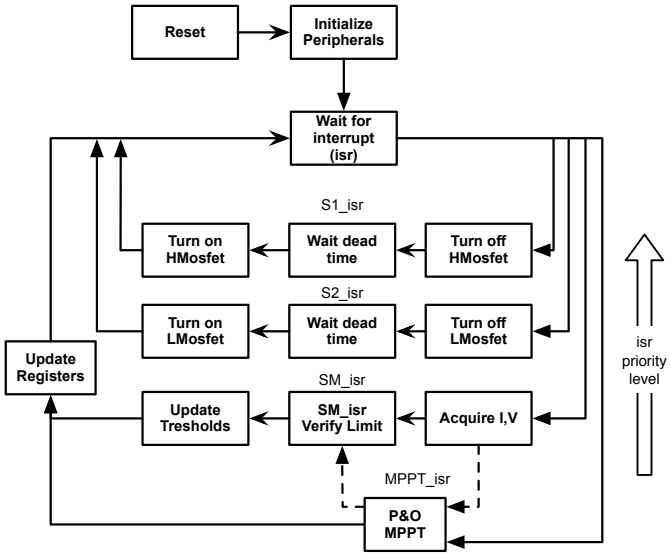

Figure 5.8: Flow chart of routines developed for the dsPIC microcontroller with software SM modulator.

is the minimum consumption of hardware resources, so that it can be exported on any micro controller device having only two analog comparators, but this is paid with a more heavy CPU use. Of course, for the reasons explained above, in this case the performances in terms of maximum switching frequency will depend on the speed of the CPU for performing the ISR and by the maximum sampling rate of the internal ADC and DAC. Fig.5.8 shows the complete flow chart of the main ISR functions developed for the photovoltaic application shown. Besides the service routines **S1_isr** and **S2_isr** used for implementing the software modulation, two additional routines are required. The first one, named

SM_isr, is devoted to implement the digital part of the SM (5.10) and to update the comparators DAC registers.
The second one, named **MPPT_isr**, implements the P&O MPPT algorithm used to track the PV maximum power point. Details on such an algorithm and its design are reported in [FPSV05].

5.3.2 SM controller with hardware modulator

Such a solution employs, in addition to the comparators, the PWM module. In this way the CPU is not involved in the modulating process, so that it is free to perform other tasks. The hardware modulator takes advantage of the PWM modulator by forcing it to work at a variable frequency. Such a feature is obtained by interfacing the comparators with the *fault* and *reset* mechanisms already implemented in the embedded PWM modulator.

The *fault* is a mechanism, triggered by an external signal, that

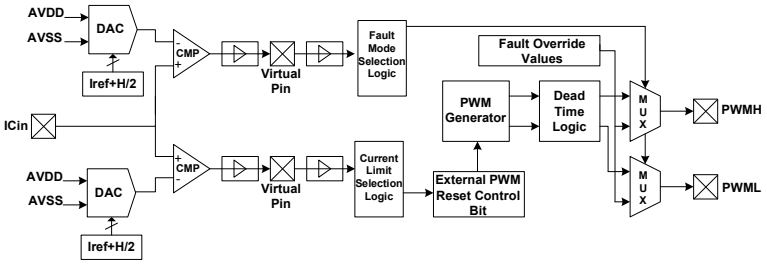

Figure 5.9: dsPIC configuration for the sliding-mode modulator by using the PWM modulator

overrides the duty-cycle value so that it can be used for imposing an asynchronous $1 \rightarrow 0$ transition in the PWM output.
The *reset* is a mechanism, triggered by an external signal, that restarts the PWM counter and this corresponds to have a $0 \rightarrow 1$ transition in the PWM output. The latter is asynchronous with respect to the switching period pre-charged in the PWM modulator. Now, if the comparators' outputs are settled so that CMP1

is used to activate the *reset* and CMP2 is used to activate the *fault*, the desired SM modulator is obtained. As concerns the comparators' inputs, such a solution uses the same configuration described above. If the PWM modulator is used, it is configured in order to have automatically a pair of complementary outputs ($\mathbf{u}$ and $\bar{\mathbf{u}}$) and by setting the desired dead time between the two outputs by means of the dedicated PWM registers, thus without involving the CPU. The Microchip dsPIC used on the converter

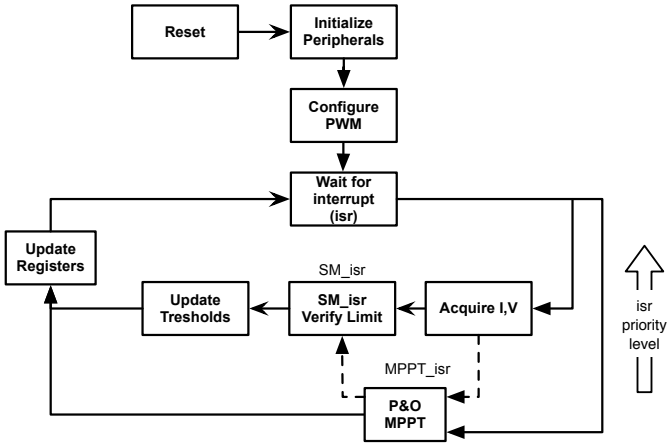

Figure 5.10: Flow chart of routines developed for the dsPIC microcontroller with hardware SM modulator.

board allows to interface the analog comparators with the PWM modulator without any external connection to the chipset. This is possible because the device supports four virtual re-mappable pins which have the same functions of all the other re-mappable pins, excepting the pinouts. These four pins are internal to the devices and they are not connected to a physical device pin. The virtual pins provide a simple way for inter-peripheral connection without utilizing a physical pin. In the photovoltaic application shown in this thesis they have ben used to connect the output of the analog comparators as trigger for the PWM fault and reset functionality in a fast and flexible way. Fig.5.9 shows the complete configura-

tion of the hardware SM modulator.
A drawback of such a solution is the need of pre-configuring the PWM module with fixed values of the switching frequency and of the duty cycle. In order to ensure a correct operation of the SM controller, such values must be fixed on the basis of the worst operating conditions.

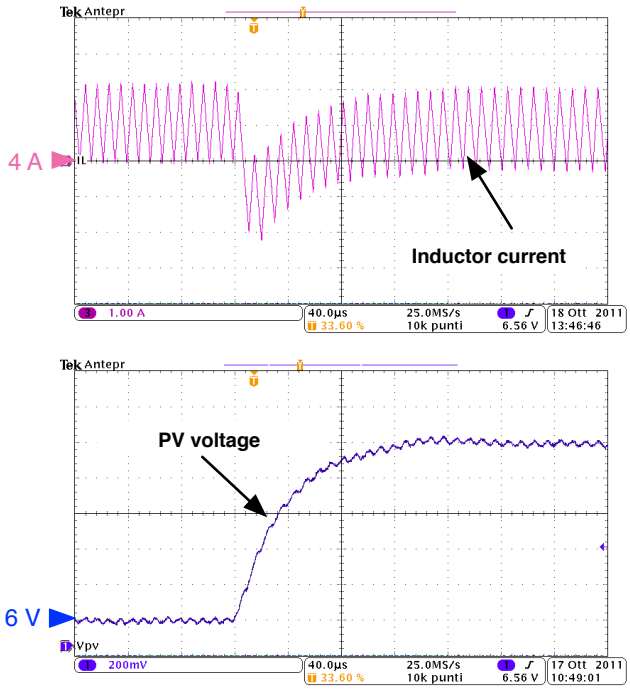

Figure 5.11: System step response whit the hybrid SM control.

The proposed solution represents an advanced use of the PWM modulator because the *fault* and *reset* mechanisms are usually used as a safety protection. Instead, in the proposed photovoltaic application such mechanisms are used for fixing the normal operating conditions. The SM control with the hardware modulator has been tested experimentally: in this case the CPU usage is limited to the initialization procedure used to configure the PWM module. Fig.5.10 shows the flow chart of the ISR functions used for

controlling the photovoltaic system and employing the hardware SM modulator. In this case the CPU processes only the digital part of the SM equation and the MPPT service routine.

5.4 Experimental results

The experimental results have been obtained by means of a laboratory prototype reproducing the scheme shown in Fig. 5.3, whose parameters are listed in Tab.5.1. Fig.5.11 and Fig.5.5 show the experimental and the simulation results respectively. Waveforms

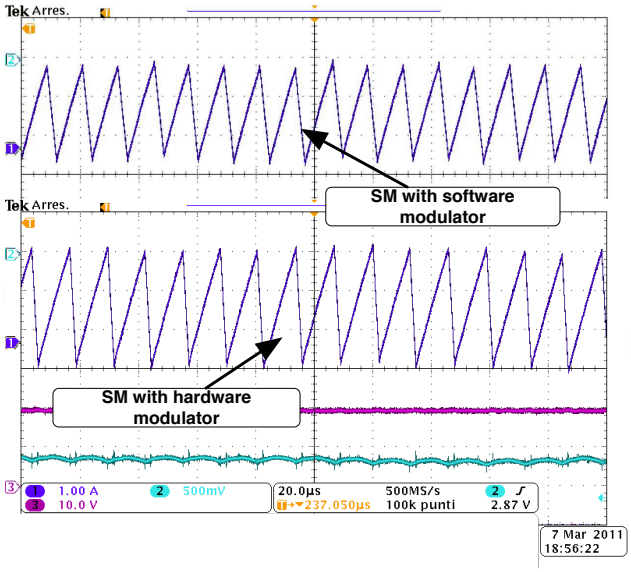

Figure 5.12: Performance comparison for the software and hardware SM modulators.

have been obtained by imposing a step variation of 1 V on V_{ref} and fit very well. The results confirm that the hardware and software configuration of the dsPIC have been carried out properly. Both the SM controller implementations have been tested and the results obtained for the photovoltaic application presented are very

similar, both in terms of PV voltage regulation and dynamic performances. Fig.5.12 shows the waveform of the inductor current obtained by using the two possible implementations of the hybrid SM control. The use of the software modulator gives rise to a slightly greater chattering effect, which is evident because of a small sub-harmonic oscillation. Nevertheless, in both cases the chattering effect is almost negligible and no additional correction has been required in order to reduce it furthermore.

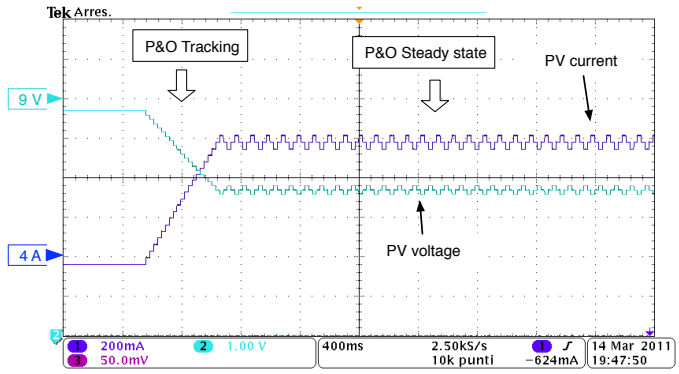

Figure 5.13: testing of the MPPT performance with SM control.

Finally, the software part implementing the P&O MPPT algorithm has been activated in the dsPIC in order to test the whole control system: Fig.5.13 shows the tracking performances and the steady-state MPPT behavior. The three level stair wise voltage waveform at the input terminals of the SEPIC converter confirms that the SM control is able to reject the noise at the double of the grid frequency that comes from the converter's output.

Conclusions

In this dissertation a technique for the maximum power point tracking of photovoltaic systems has been introduced. The approach is based on the sliding mode control technique and is based on the sensing of the current drained by the capacitor which is usually put in parallel with the photovoltaic generator. The technique implementation has been explained in the first part of the thesis by using the boost converter topology. It requires few components and allows to track fast irradiance variations, such properties make the proposed technique particularly suitable for sustainable mobility.
The ability in rejecting the output disturbance at the converter's input terminals makes the proposed solution effective not only in grid connected applications, but in any case in which the PV voltage might be affected by noises back propagating towards the photovoltaic generator from the dc/dc converter output, for example, in Distributed MPPT architectures. Simulation results and experimental measurements shown in Chapter 2 confirm the performances of the proposed control technique.

The guidelines for the design of a SM based MPPT technique have been presented in Chapter 3. The study has been focused on a synchronous SEPIC converter but the conditions achieved can be extended to a wider class of dc/dc converters. The key points can be summarized as follows:

- On the basis of the data available about the PV source and

its operating conditions, the range in which the differential resistance R_{diff} varies can be evaluated. The inequalities (3.15) and (3.23), together with the classical conditions concerning the voltage and current ripples [EM01], allow to design the passive components of the converter's power stage.

- On the basis of the value of the output voltage V_o and of the range in which V_{ref} is expected to vary, $\lambda_{2,3}$ (3.37) add further conditions to the previous ones. In particular, design constraints in terms of damping and settling time of the uncontrolled state variables x_3 and x_4 give further conditions on the power stage parameters.

- Inequality (3.26) assure the reachability condition for the proposed SM control equation, while (3.27) and (3.31) give the constraints for assuring the existence condition.

- Further design conditions are obtained by means of the analysis shown in Section 3.3.2. As discussed therein, all the parameters mentioned above affect its width. Moreover, the effect of the expected range of the irradiance level must be kept into account.

- On the basis of the designed value of the switching frequency, the hysteresis band is designed and the SM control is defined through (3.28).

- By supposing that a perturbative MPPT algorithm acts on V_{ref}, the frequency and the amplitude of the V_{ref} perturbations can be designed according dynamic fixed by the SM control.. In particular, the frequency of the perturbations must be designed by a proper choice of k_1, k_2 and C_{in} only, according to λ_1 in (3.37). The tradeoff between system promptness and the RoE width demonstrated in this paper must be kept into account. The amplitude of the perturbations, that is ΔV_{ref}, must be designed according to the analysis performed in Section 3.3.2. The smaller the RoE

width the smaller the ΔV_{ref} in order to preserve the SM control.

A dynamic models of converters controlled by a sliding mode based maximum power point tracking for photovoltaic applications has been presented in Chapter 4. The analysis has been carried out by referring to the boost and SEPIC topologies, which are among the most interesting ones in photovoltaic applications. As shown a correction term, allowing to have an increased accuracy of the model, is also derived. Such model allows to evaluate the dynamic response of the proposed SM architecture when the converter parasitic parameters have been considered. Simulation results obtained by PSIM and experimental measurements corroborate the analytical method.

Finally, in Chapter 5, an hybrid analog-digital implementation of a sliding mode controller for dc/dc converters used in photovoltaic application has been proposed. A general procedure, based on the theoretical analysis of the sliding mode equation, has been developed in order to design in the best way the hybrid structure. The main feature of the proposed solution is that the modulation function of the sliding mode control is obtained by using two analog comparators, which are usually already integrated in the new generations of micro controllers. The hybrid implementation optimizes the hardware resources and assures performances that are comparable with the sliding mode controller implemented by means of discrete components only. Simulation results and experimental measurements confirm the attractiveness of the proposed method and confirm the effectiveness of the design solutions proposed.

Bibliography

[AFP+10] G. Adinolfi, N. Femia, G. Petrone, G. Spagnuolo, and M. Vitelli, *Design of dc/dc converters for dmppt pv applications based on the concept of energetic efficiency*, Journal of Solar Energy Engineering **132** (2010), no. 2, 021005.

[ARS+12] R. Alonso, E. Roman, A. Sanz, V.E.M. Santos, and P. Ibanez, *Analysis of inverter-voltage influence on distributed mppt architecture performance*, Industrial Electronics, IEEE Transactions on **59** (2012), no. 10, 3900 –3907.

[BBR+02] T. Brekken, N. Bhiwapurkar, M. Rathi, N. Mohan, C. Henze, and L.R. Moumneh, *Utility-connected power converter for maximizing power transfer from a photovoltaic source while drawing ripple-free current*, Power Electronics Specialists Conference, 2002. pesc 02. 2002 IEEE 33rd Annual, vol. 3, 2002, pp. 1518 – 1522 vol.3.

[BCG+11a] E. Bianconi, J. Calvente, R. Giral, G. Petrone, C. A. Ramos-Paja, G. Spagnuolo, and M.Vitelli, *A fast current-based mppt technique based on sliding mode control*, Proc of IEEE International Symposium on Industrial Electronics - ISIE 2011 (2011), 59–64.

[BCG+11b] ———, *Improving the perturb and observe maximum power point tracking by using sliding mode control*, Proc of IEEE International Symposium on Industrial Electronics - ISIE 2011 (2011), 310–315.

[BCG+13] E. Bianconi, J. Calvente, R. Giral, E. Mamarelis, G. Petrone, C. A. Ramos-Paja, G. Spagnuolo, and M. Vitelli, *A fast current-based mppt technique employing sliding mode control*, Industrial Electronics, IEEE Transactions on **60** (2013), no. 3, 1168 –1178.

[CDNFZ11] A. Cantillo, A. De Nardo, N. Femia, and W. Zamboni, *Stability issues in peak-current-controlled sepic*, Power Electronics, IEEE Transactions on **PP** (2011), no. 99, 1.

[CSC09] S.J. Chiang, Hsin-Jang Shieh, and Ming-Chieh Chen, *Modeling and control of pv charger system with sepic converter*, Industrial Electronics, IEEE Transactions on **56** (2009), no. 11, 4344 –4353.

[DT09] M. Dal and R. Teodorescu, *Chattering suppression for dsp based sliding mode current control of pm dc drives*, Industrial Electronics, 2009. IECON '09. 35th Annual Conference of IEEE (2009), 1474 –1479.

[Dur06] H. Tarik Duru, *A maximum power tracking algorithm based on impp = f(pmax) function for matching passive and active loads to a photovoltaic generator*, Solar Energy **80** (2006), no. 7, 812 – 822.

[EC07] T. Esram and P.L. Chapman, *Comparison of photovoltaic array maximum power point track-*

ing techniques, Energy Conversion, IEEE Transactions on **22** (2007), no. 2, 439 –449.

[EM01] Robert W. Erickson and Dragan Maksimovic, *Fundamentals of power electronics*, 2ed ed., Springer, 2001.

[FLM08] R. Faranda, S. Leva, and V. Maugeri, *Mppt techniques for pv systems: Energetic and cost comparison*, Power and Energy Society General Meeting - Conversion and Delivery of Electrical Energy in the 21st Century, 2008 IEEE, july 2008, pp. 1 –6.

[FLP+08] N. Femia, G. Lisi, G. Petrone, G. Spagnuolo, and M. Vitelli, *Distributed maximum power point tracking of photovoltaic arrays: Novel approach and system analysis*, Industrial Electronics, IEEE Transactions on **55** (2008), no. 7, 2610 –2621.

[FPSV05] N. Femia, G. Petrone, G. Spagnuolo, and M. Vitelli, *Optimization of perturb and observe maximum power point tracking method*, Power Electronics, IEEE Transactions on **20** (2005), no. 4, 963 – 973.

[FPSV09] _____, *A technique for improving p&o mppt performances of double-stage grid-connected photovoltaic systems*, Industrial Electronics, IEEE Transactions on **56** (2009), no. 11, 4473 –4482.

[FPSV12] _____, *Power electronics and control techniques for maximum energy harvesting in photovoltaic systems*, 1st ed., CRC Press, 2012.

[GLSA+10] Shuibao Guo, Xuefang Lin-Shi, B. Allard, Yanxia Gao, and Yi Ruan, *Digital sliding-mode controller for high-frequency dc/dc smps*, Power

Electronics, IEEE Transactions on **25** (2010), no. 5, 1120 –1123.

[G.P07] M.Vitelli. G.Petrone, G.Spagnuolo, *Analytical model of mismatched photovoltaic fields by means of lambert w-function*, Solar Energy Materials and Solar Cells **91** (2007), no. 18, 1652–1657.

[GPSV10] A. Giustiniani, G. Petrone, G. Spagnuolo, and M. Vitelli, *Low frequency current oscillations and maximum power point tracking in grid-connected fuel cell based system*, IEEE Transactions on Industrial Electronics **57** (2010), no. 6, 2042 – 2053.

[HKIO95] T. Hiyama, S. Kouzuma, T. Imakubo, and T.H. Ortmeyer, *Evaluation of neural network based real time maximum power tracking controller for pv system*, Energy Conversion, IEEE Transactions on **10** (1995), no. 3, 543 –548.

[HMHO95] K.H. Hussein, I. Muta, T. Hoshino, and M. Osakada, *Maximum photovoltaic power tracking: an algorithm for rapidly changing atmospheric conditions*, Generation, Transmission and Distribution, IEE Proceedings- **142** (1995), no. 1, 59 –64.

[HR00] D.P. Hohm and M.E. Ropp, *Comparative study of maximum power point tracking algorithms using an experimental, programmable, maximum power point tracking test bed*, Photovoltaic Specialists Conference, 2000. Conference Record of the Twenty-Eighth IEEE, 2000, pp. 1699 –1702.

[ISTS00] K. Irisawa, T. Saito, I. Takano, and Y. Sawada, *Maximum power point tracking control of photovoltaic generation system under non-uniform insolation by means of monitoring cells*, Photovoltaic Specialists Conference, 2000. Confer-

ence Record of the Twenty-Eighth IEEE, 2000, pp. 1707 –1710.

[JBSLORGL10] E. Jimenez-Brea, A. Salazar-Llinas, E. Ortiz-Rivera, and J. Gonzalez-Llorente, *A maximum power point tracker implementation for photovoltaic cells using dynamic optimal voltage tracking*, Applied Power Electronics Conference and Exposition (APEC), 2010 Twenty-Fifth Annual IEEE, feb. 2010, pp. 2161 –2165.

[KKN09] Jung-Min Kwon, Bong-Hwan Kwon, and Kwang-Hee Nam, *Grid-connected photovoltaic multistring pcs with pv current variation reduction control*, Industrial Electronics, IEEE Transactions on **56** (2009), no. 11, 4381 –4388.

[KKY06] Il-Song Kim, Myung-Bok Kim, and Myung-Joong Youn, *New maximum power point tracker using sliding-mode observer for estimation of solar array current in the grid-connected photovoltaic system*, Industrial Electronics, IEEE Transactions on **53** (2006), no. 4, 1027 –1035.

[KPB05] S.B. Kjaer, J.K. Pedersen, and F. Blaabjerg, *A review of single-phase grid-connected inverters for photovoltaic modules*, Industry Applications, IEEE Transactions on **41** (2005), no. 5, 1292 – 1306.

[LEMB09] L. Linares, R.W. Erickson, S. MacAlpine, and M. Brandemuehl, *Improved energy capture in series string photovoltaics via smart distributed power electronics*, Applied Power Electronics Conference and Exposition, 2009. APEC 2009. Twenty-Fourth Annual IEEE, feb. 2009, pp. 904 –910.

[LGLSA11] Bo Li, Shuibao Guo, Xuefang Lin-Shi, and B. Allard, *Design and implementation of the digital controller for boost converter based on fpga*, Industrial Electronics (ISIE), 2011 IEEE International Symposium on, june 2011, pp. 1549 –1554.

[LLPG10] O. Lopez-Lapena, M.T. Penella, and M. Gasulla, *A new mppt method for low-power solar energy harvesting*, Industrial Electronics, IEEE Transactions on **57** (2010), no. 9, 3129 –3138.

[LLPG11] O. Lopez-Lapena, M. Penella, and M. Gasulla, *A close-loop maximum power point tracker for subwatt photovoltaic panels*, Industrial Electronics, IEEE Transactions on **PP** (2011), no. 99, 1.

[LLSL+11] N. Li, X. Lin-Shi, P. Lefranc, E. Godoy, A. Jaafar, and B. Allard, *Universal dc-dc converter using sepic*, Power Electronics and Applications (EPE 2011), Proceedings of the 2011-14th European Conference on, 30 2011-sept. 1 2011, pp. 1 –10.

[LW08] Quan Li and P. Wolfs, *A review of the single phase photovoltaic module integrated converter topologies with three different dc link configurations*, Power Electronics, IEEE Transactions on **23** (2008), no. 3, 1320 –1333.

[MPS13] E. Mamarelis, G. Petrone, and G. Spagnuolo, *An hybrid digital-analog sliding mode controller for photovoltaic applications*, Industrial Informatics, IEEE Transactions on **9** (2013), no. 2, 1094 – 1103.

[MRST93] P. Mattavelli, L. Rossetto, G. Spiazzi, and P. Tenti, *General-purpose sliding-mode controller*

for dc/dc converter applications, Power Electronics Specialists Conference, 1993. PESC '93 Record., 24th Annual IEEE, jun 1993, pp. 609 –615.

[MSGO+12] L. Martinez-Salamero, G. Garcia, M. Orellana, C. Lahore, and B. Estibals, *Start-up control and voltage regulation in a boost converter under sliding-mode operation*, Industrial Electronics, IEEE Transactions on **PP** (2012), no. 99, 1.

[MST95] L. Malesani, R.G. Spiazzi, and P. Tenti, *Performance optimization of cuk converters by sliding-mode control*, Power Electronics, IEEE Transactions on **10** (1995), no. 3, 302 –309.

[NBGM10] J.J. Negroni, D. Biel, F. Guinjoan, and C. Meza, *Energy-balance and sliding mode control strategies of a cascade h-bridge multilevel converter for grid-connected pv systems*, Industrial Technology (ICIT), 2010 IEEE International Conference on, march 2010, pp. 1155 –1160.

[Oga95] Katsuhiko Ogata, *Discrete-time control systems (2nd edition)*, Prentice Hall (1995), 745.

[PC06] J.H. Park and B.H. Ch, *Small signal modeling of hysteretic current mode control using the pwm switch model*, Computers in Power Electronics, 2006. COMPEL '06. IEEE Workshops on, july 2006, pp. 225 –230.

[PS03] A.V. Peterchev and S.R. Sanders, *Quantization resolution and limit cycling in digitally controlled pwm converters*, Power Electronics, IEEE Transactions on **18** (2003), no. 1, 301 – 308.

[PST+08] G. Petrone, G. Spagnuolo, R. Teodorescu, M. Veerachary, and M. Vitelli, *Reliability issues in photovoltaic power processing systems*, Industrial Electronics, IEEE Transactions on **55** (2008), no. 7, 2569 –2580.

[RCCP+11] C. Restrepo, J. Calvente, A. Cid-Pastor, A.E. Aroudi, and R. Giral, *A noninverting buck-boost dc-dc switching converter with high efficiency and wide bandwidth*, Power Electronics, IEEE Transactions on **26** (2011), no. 9, 2490 –2503.

[RG11] J.P.Gaubert R.Kadri and G.Champenois, *An improved maximum power point tracking for photovoltaic grid-connected inverter based on voltage-oriented control*, Industrial Electronics, IEEE Transactions on **58** (2011), no. 1, 66 –75.

[Ś11] A. Śabanovic, *Variable structure systems with sliding modes in motion control - a survey*, Industrial Informatics, IEEE Transactions on **7** (2011), no. 2, 212 –223.

[SM01] G. Spiazzi and P. Mattavelli, *Sliding-mode control of switched-mode power supplies*, The Power Electronics Handbook Edited by Timothy L. Skvarenina (CRC Press 2001), no. chapter 8, 1 – 23.

[SPV+12] G. Spagnuolo, G. Petrone, M. Vitelli, J. Calvente, C. Ramos-Paja, R. Giral, E. Mamarelis, and E. Bianconi, *A fast current-based mppt technique employing sliding mode control*, Industrial Electronics, IEEE Transactions on **PP** (2012), no. 99, 1.

[SR87] H. Sira-Ramirez, *Sliding motions in bilinear switched networks*, Circuits and Systems, IEEE Transactions on **34** (1987), no. 8, 919 – 933.

[Sun02a] Jian Sun, *Small-signal modeling of variable-frequency pulsewidth modulators*, Aerospace and Electronic Systems, IEEE Transactions on **38** (2002), no. 3, 1104 – 1108.

[Sun02b] T. Suntio, *Small-signal modeling of switched-mode converters under direct-on-time control-a unified approach*, IECON 02 [Industrial Electronics Society, IEEE 2002 28th Annual Conference of the], vol. 1, nov. 2002, pp. 479 – 484 vol.1.

[TLT08] Siew-Chong Tan, Y.M. Lai, and C.K. Tse, *General design issues of sliding-mode controllers in dc dc converters*, Industrial Electronics, IEEE Transactions on **55** (2008), no. 3, 1160 –1174.

[U.E03] U.Eicker, *Solar technologies for buildings*, Wiley, 2003.

[UGS09] V. Utkin, J. Gulder, and J. Shi, *Sliding mode control in electro-mechanical systems*, 2ed ed., CRC Press, 2009.

[VICCMS11] E. Vidal-Idiarte, C.E. Carrejo, J. Calvente, and L. Martínez-Salamero, *Two-loop digital sliding mode control of dc-dc power converters based on predictive interpolation*, Industrial Electronics, IEEE Transactions on **58** (2011), no. 6, 2491 –2501.

[VIMSG+04] E. Vidal-Idiarte, L. Martinez-Salamero, F. Guinjoan, J. Calvente, and S. Gomariz, *Sliding and fuzzy control of a boost converter using an 8-bit microcontroller*, Electric Power Applications, IEE Proceedings - **151** (2004), no. 1, 5 – 11.

[Web] Website, *http://mathworld.wolfram.com*.

[Web11] ———, *http://www.microchip.com/wwwproducts*.

[WKK+94] Chung-Yuen Won, Duk-Heon Kim, Sei-Chan Kim, Won-Sam Kim, and Hack-Sung Kim, *A new maximum power point tracker of photovoltaic arrays using fuzzy controller*, Power Electronics Specialists Conference, PESC '94 Record., 25th Annual IEEE, jun 1994, pp. 396 –403 vol.1.

[WL10] Rong-Jong Wai and Chun-Yu Lin, *Active low-frequency ripple control for clean-energy power-conditioning mechanism*, Industrial Electronics, IEEE Transactions on **57** (2010), no. 11, 3780 –3792.

[WW08] Rong-Jong Wai and Wen-Hung Wang, *Grid-connected photovoltaic generation system*, Circuits and Systems I: Regular Papers, IEEE Transactions on **55** (2008), no. 3, 953 –964.

[WWL08] Rong-Jong Wai, Wen-Hung Wang, and Chung-You Lin, *High-performance stand-alone photovoltaic generation system*, Industrial Electronics, IEEE Transactions on **55** (2008), no. 1, 240 –250.

[XCK+04] Yaosuo Xue, Liuchen Chang, Sren Baekhj Kjaer, J. Bordonau, and T. Shimizu, *Topologies of single-phase inverters for small distributed power generators: an overview*, Power Electronics, IEEE Transactions on **19** (2004), no. 5, 1305 – 1314.

[YLM12] Yingyi Yan, F.C. Lee, and P. Mattavelli, *Unified three-terminal switch model for current mode controls*, Power Electronics, IEEE Transactions on **27** (2012), no. 9, 4060 –4070.

[YUO99] K.D. Young, V.I. Utkin, and U. Ozguner, *A control engineer's guide to sliding mode control*, Control Systems Technology, IEEE Transactions on **7** (1999), no. 3, 328 –342.

Acknowledgements

Nella mia vita ho avuto modo pochissime volte di ringraziare qualcuno, non perchè non ne abbia mai avuto il motivo(anzi..) ma perche' non ho mai capito quanto invece fosse importante... soprattutto per me! questo e' sicuramente il luogo ed il momento giusto per cominciare.

Inizio ovviamente dalla mia famiglia: mio padre, così lontano ma a cui voglio ovviamente un mondo di bene...; mia madre, sempre presente nel bene e nel male; mio fratello e mia sorella, che sono sempre con me ovunque io vada e qualunque cosa faccia. Anche grazie a loro (..ed esattamente come loro) ho capito che se a volte nella vita ti aspetti invano determinate parole e sentimenti senza mai ottenerli, anche se ne hai inevitabilmente bisogno, cio' non vuol dire non provare quelle esatte emozioni, nè vuol dire che non ci siano...Spesso sono anche fortemente presenti ma non riescono ad uscire o ad essere evidenti come dovrebbero.(Ahime' vale anche il viceversa!!!) Ad ogni modo Grazie di tutto.

Un pensiero particolare va ai miei amici di una vita: Mario, Andrea, Felice, Giovanni, Alex. Se sono quello di adesso lo devo anche a voi, alle nostre giornate passate insieme, ai ricordi che mi fanno star bene ancora oggi, a tutto cio' che di bello e brutto e' capitato e che insieme abbiamo affrontato...Grazie di tutto.

Non posso dimenticare i miei traghettatori: Giovanni S. , che mi ha accolto ed ha permesso questa particolare avventura, e Giovanni P., con cui ho passato innumerevoli giornate di lavoro. Con

loro ho imparato che spesso dietro ad una semplice parola, in questo caso "tutor", alcune volte si ha la fortuna di percepire sfumature di altre quali "guida", per le numerose volte in cui avete indirizzato le mie decisioni verso la giustra strada: il mio caratteraccio me la faceva perdere spesso; "insegnante", per l'enorme quantita' di cose che mi avete insegnato ed ho avuto modo di imparare nel corso di questi pochi anni (avrei potuto fare molto di piu'...); "amico", per le volte che avete preso forse inconsapevolmente per mano la mia vita ed aiutato nei momenti difficili che purtroppo possono capitare; "padre", per i meravigliosi consigli e le ramanzine che mi son beccato e meritato, o di cui avevo semplicemente bisogno. Auguro a tutti di avere la mia stessa fortuna...Grazie di tutto.

Come dimenticare gli amici di corso all'universita': primo su tutti Lorenzo, il cui spirito e forza d'animo, caparbietà e allegria coinvolgente ho sempre ammirato. Ma anche Salvatore, Angelo, Mariella, Graziano, Carmela, Rosa, Marcella, Grazia, Carletto, Pasquale, Mimmo, il saggio Lettieri M., l'amicone Cioffredi, il Fè, i gemelli Marco e Luca e tanti altri a cui chiedo scusa per non averli nominati. Avete avuto un ruolo fondamentale nel corso di questi anni e grazie alla vostra splendida compagnia e immancabile presenza, che spesso non ho saputo valorizzare e coltivare, le fatiche e i problemi si affrontavano più in fretta e piu' agevolmente...Grazie di tutto.

Un ringraziamento speciale anche ai ragazzi del lab: Gianluca (detto Gaudì..), la cui spensieratezza e disponibilita' mi han fatto compagnia come se ci conoscessimo da sempre; Davide (detto il Sola), la cui fermezza e simpatia mi han dato lo spunto per guardare il futuro in modo diverso (spero di aver imparato...); Max , la cui flemma e bonta' d'animo mi han dato piu' che una mano in un periodo a dir poco complicato; Fabrizio ed Armando, che nonostante le loro Wicissitudini han fatto sicuramente parte di questo mio percorso con la loro presenza sempre piacevole e ricca di episodi; Zi' Mario, a cui chiedo scusa per la schiumata, la

cui esperienza e confidenza han reso piu' leggere le mie giornate di lavoro; Evelina e Michela, le tesiste indimenticabili e insostituibili del lab (grazie per essermi state vicino quando avete potuto..); Giulia, la cui disponibilita' e intraprendenza mi han dato ulteriore stimolo per affrontare le numerose difficolta'. Un grandissimo abbraccio e un vi voglio bene e' d'obbligo...Grazie di tutto.

Ringrazio anche il Prof. Nicola F.: per svariati motivi che non sto qui ad elencare e' stato un esempio prima e dopo averlo conosciuto... Grazie di tutto.

Un ringraziamento doveroso a chi nella mia vita invece c'e' stato, anche solo di passaggio, a chi e' appena arrivato, a chi sbadatamente ho dimenticato, a chi non ne ha voluto far parte, a chi ci si e' trovato, a chi ha evitato, a chi non ha creduto in me, a chi non lo sa di essere tanto importante, a quelli che mi hanno umiliato e ferito, a chi ho trattato male per qualche motivo, a chi mi ha fatto cadere e a chi mi ha sferrato il colpo di grazia, a chi invece mi ha voluto bene ma non l'ho mai capito fino in fondo, a chi non c'e' piu' : F.,M.,L.,E.,J... A tutti voi dico: se vi ho nominato vuol dire che la vostra presenza si e' fatta sentire, chi piu' chi molto meno. In fondo mi sento di dire che senza di voi non ce l'avrei mai fatta! Dunque Grazie di tutto.

Non si finisce mai di imparare...

25-26 Marzo 2013.

...it matters not how strait the gate,
how charged with punishments the scroll,
I am the master of my fate:
I am the captain of my soul.